Copyright

by

Rodolfo Salas

2015

The Dissertation Committee for Rodolfo Salas certifies that this is the approved version of the following dissertation:

Rare-Earth Arsenide III-V Nanocomposites for Heterodyne Terahertz Generation

Committee:

____
Seth R. Bank, Supervisor

____
Edward T. Yu

____
Emanuel Tutuc

____
Mikhail A. Belkin

____
Alexander A. Demkov

Rare-Earth Arsenide III-V Nanocomposites for Heterodyne Terahertz Generation

by

Rodolfo Salas, B.S.; M.S.

Dissertation

Presented to the Faculty of the Graduate School of

The University of Texas at Austin

in Partial Fulfillment

of the Requirements

for the Degree of

Doctor of Philosophy

The University of Texas at Austin

May 2015

Dedicated to my parents, my wife, and my son.

Rare-Earth Arsenide III-V Nanocomposites for Heterodyne Terahertz Generation

Rodolfo Salas, Ph.D.

The University of Texas at Austin, 2015

Supervisor: Seth R. Bank

Room-temperature, broadly tunable, continuous-wave, terahertz sources operating in the range from 0.3 to 3 THz are required for applications such as high-resolution spectroscopy and medical imaging. Optical heterodyne conversion, or photomixing, is a technique for generating terahertz frequencies by modulating the photoconductance of a material via the interference of two incident lasers. For efficient terahertz generation, the photoconductive material must simultaneously possess high dark resistivity, high carrier mobilities, and short carrier lifetimes. Superlattice based nanocomposites of rare-earth arsenide nanoparticles epitaxially embedded into $In_{0.53}Ga_{0.47}As$ are attractive candidate materials for terahertz generation via photomixing. In addition to the superior charge transport properties of InGaAs relative to GaAs, InGaAs-based devices can leverage the well-developed fiber-optic technology infrastructure available at 1550 nm, enabling low-cost, compact, room-temperature terahertz sources. Unfortunately, due to the alignment of the Fermi level near the InGaAs conduction band in previously investigated ErAs-InGaAs nanocomposites, photomixers based on these materials currently exhibit high leakage currents resulting in poor device performance. High depositions of ErAs (up to 1.75 monolayers per superlattice period) and beryllium counter-doping can partially overcome this limitation by adjusting the Fermi level closer to the midgap. However,

carrier mobilities suffer, reaching a high of only 202 cm^2/V-s, as a result of carrier scattering from the high counter doping required. Through an exploration of other rare-earth species, we were able to discern the importance of the structural quality of the III-V host matrix overgrowth. By improving the material overgrowth through surfactant-mediated epitaxy and nanoparticle morphology optimizations, we were able to increase the total amount of deposited rare-earth arsenide to 3.2 monolayers per superlattice period, while maintaining good structural quality of the overall nanocomposite. The properties of the resulting photoconductive material were also significantly improved, achieving Fermi level alignments near 240 meV below the conduction band and high dark resistivities of 4.2 Ω-cm, a record for a 1550 nm absorbing nanocomposite material without beryllium counter doping. Mobilities remained above 2700 cm^2/V-s, however, the carrier lifetimes of these enhanced nanocomposites leveled off at 1.45 ps, above the terahertz threshold of 1 ps. An alternate path to improve the properties of nanocomposites is to change the Fermi level alignment of the nanoparticle/matrix interface by using alloy compositions of $In_{0.53}Ga_{0.47}As$ and $GaAs_{0.5}Sb_{0.5}$. Since the Fermi level aligns closer to the valence band in GaAsSb and to the conduction band in InGaAs, the Fermi level can be tailored toward the midgap. We demonstrate rare-earth arsenide nanocomposite materials based on these quaternary alloys that achieve 2× improvement in carrier lifetimes over previous nanocomposites without any counter-doping, 0.73 ps, while maintaining carrier mobilities at least 4× higher than any other material based on counter-doping, over 4000 cm^2/V-s, and modest dark resistivities of 0.8 Ω-cm. Although the InGaAsSb alloy matrix is a potentially elegant solution, the growth of these materials is very challenging due to the miscibility gap that exists for this quaternary alloy. With further optimization, RE-As-InGaAsSb nanocomposite systems show great potential for the development of 1550 nm based photomixing devices.

Table of Contents

Table of Contents vii

List of Tables ix

List of Figures xiii

Chapter 1: Introduction 1

1.1 Motivation and Application for Terahertz Sources 1

1.2 Terahertz Sources 4

1.3 Photomixer Theory 6

1.4 Photomixer Thermal Considerations 13

1.5 Photoconductive Materials for Photomixers 17

1.5.1 Low-Temperature-Grown GaAs 18

1.5.2 ErAs / GaAs Nanocomposites 18

1.5.3 Small Bandgap Materials and Nanocomposites 20

1.6 Organization of Dissertation 21

Chapter 2: Molecular Beam Epitaxy and Material Characterization 23

2.1 Molecular Beam Epitaxy 24

2.2 Flux Measurements and Growth Calibrations 26

2.3 Reflection High Energy Electron Diffraction 28

2.4 High Resolution X-ray Diffraction 30

2.5 Atomic Force Microscopy 32

2.6 Hall Measurements 33

2.7 Carrier Lifetime Measurements 36

2.7.1 Absorption Shifts 37

2.7.2 Carrier Capture and Recombination 39

2.7.3 Pump-Probe Transmission Setup 40

Chapter 3: Superlattices of RE-As:InGaAs 45

3.1 Rare-Earth Arsenides on InGaAs 45

3.2 Growth and Structure of RE-As Superlattices 47

3.3 Electrical Properties of RE-As Superlattices 52
3.4 Carrier Lifetime of RE-As Superlattices..57
3.5 Summary 59

Chapter 4: Growth Enhancements of RE-As:InGaAs Superlattices......................62
4.1 Surfactant-Mediated Growth 62
4.2 Growth Rate-Dependent RE-As Nanoparticle Morphology..........65
4.3 Growth and Structure of Enhanced LuAs:InGaAs Superlattices...66
4.4 Electrical Properties of Enhanced LuAs:InGaAs Superlattices.....73
4.5 Carrier Lifetimes of Enhanced LuAs:InGaAs Superlattices..........78
4.6 Summary 79

Chapter 5: Optimizations to Enhanced RE-As:InGaAs Superlattices 82
5.1 Growth Enhancements of LaAs:InGaAs and GdAs:InGaAs Superlattices 82
5.2 Geometry Investigation of Enhanced ErAs:InGaAs Superlattices 84
5.3 Beryllium Doping of Enhanced ErAs:InGaAs Superlattices.........92
5.4 Summary 96

Chapter 6: Rare-Earth Arsenide on InGaAsSb 100
6.1 Fermi level Alignments...101
6.2 Growth and Structure of InGaAs and GaAsSb Alloys 106
6.3 Electrical Properties of InGaAsSb Based Superlattices...............110
6.4 Carrier Lifetimes of InGaAsSb Based Superlattices 112
6.5 Summary 113

Chapter 7: Material Comparison and Device Calculations.................................115
7.1 Conventional Photomixer Devices 115

Chapter 8: Conclusions 123

Appendix A:...125

References...128

List of Tables

Table 1.1: Thermal conductivity of various semiconductor materials 14

Table 3.1: RE-As species, lattice parameter and mismatch to InP. 46

Table 3.2: Properties of 30-period RE-As:InGaAs superlattices with the 40 nm period spacing grown at 490 °C. The properties summarized include RE-As species, RE-As deposition (Dep), RE-As growth rate (GR), root-mean-squared surface roughness (RMS SR), room temperature mobility (μ), room temperature dark resistivity (ρ), room temperature carrier concentration (n), Fermi level based on room temperature carrier concentration using Nilsson equation [107], activation energy from temperature dependent Hall (E_a), and carrier lifetime (τ). 61

Table 4.1: Properties of bismuth-enhanced LuAs superlattices with 30 periods of 40 nm of InGaAs grown at 490 °C and various LuAs growth rates. The properties summarized include LuAs deposition (Dep), LuAs growth rate (GR), root-mean-squared surface roughness (RMS SR), room temperature mobility (μ), room temperature dark resistivity (ρ), room temperature carrier concentration (n), Fermi level energy relative to the InGaAs conduction band based on room temperature carrier concentration using the Nilsson equation [107], activation energy from temperature dependent Hall (E_a), and carrier lifetime (τ). 81

Table 5.1: Properties of a 30-period LaAs:InGaAs superlattices with 40 nm period thickness grown at 490 °C. The properties summarized include bismuth use during InGaAs growth (Bi), total LaAs deposition (Dep), LaAs growth rate (GR), root-mean-squared surface roughness (RMS SR), room temperature mobility (μ), room temperature dark resistivity (ρ), room temperature carrier concentration (n), Fermi level based on room temperature carrier concentration using Nilsson equation [107], activation energy from temperature dependent Hall (E_a), and carrier lifetime (τ). 84

Table 5.2: Properties of bismuth-enhanced ErAs superlattices grown at 490 °C with an ErAs growth rate of 0.01 ML/s and various period geometries. The properties include: ErAs deposition (Dep), number of periods and thicknesses (L), root-mean-squared surface roughness (RMS SR), room temperature mobility (μ), room temperature dark resistivity (ρ), room temperature carrier concentration (n), Fermi level based on room temperature carrier concentration using Nilsson equation [107], activation energy from temperature dependent Hall (E_a), and carrier lifetime (τ). 98

Table 5.3: Properties of bismuth-enhanced 2.0 ML ErAs superlattices grown at 490 °C with an ErAs growth rate of 0.01 ML/s, with 30 periods of 40 nm each, and increasing uniform beryllium counter doping. The properties include: beryllium doping level, root-mean-squared surface roughness (RMS SR), room temperature mobility (μ), room temperature dark resistivity (ρ), room temperature carrier concentration (n), measured carrier majority (n = electron, p = hole), Fermi level based on room temperature carrier concentration using Nilsson equation [107], carrier activation energy from temperature dependent Hall (E_a), and carrier lifetime (τ). 99

Table 6.1: Properties of bismuth enhanced ErAs(Sb) superlattices grown at 470 °C with an ErAs(Sb) growth rate of 0.01 ML/s in an $In_{0.19}Ga_{0.81}As_{0.68}Sb_{0.32}$ matrix, with 30 periods of 40 nm each, and increasing ErAs(Sb) deposition. The properties include: ErAs deposition (Dep), root-mean-squared surface roughness (RMS SR), room temperature mobility (μ), room temperature dark resistivity (ρ), room temperature carrier concentration (n), carrier activation energy from temperature dependent Hall (E_a), and carrier lifetime (τ). 114

Table 7.1: Properties of the materials to be compared in this theoretical analysis. 117

Table 7.2: Properties of the best materials grown during all of these investigations and materials from other sources for comparison in theoretical analysis. 121

Table A.1: Properties of RE-As superlattices with 30 periods of 40 nm grown at various temperatures. The properties summarized include RE-As species and deposition amount, growth temperature (GT), growth rate (GR), root-mean-squared surface roughness (RMS SR), room temperature mobility (μ), room temperature dark resistivity (ρ), room temperature carrier concentration (n), Fermi level based on room temperature carrier concentration using Nilsson equation [107], activation energy from temperature dependent Hall (E_a), and carrier lifetime (τ). 126

Table A.2: Properties of bismuth enhanced ErAs superlattices grown at 490 °C with a 2500A InAlAs buffer layer before superlattice growth. The properties include: ErAs deposition (Dep), growth rate (GR), root-mean-squared surface roughness (RMS SR), room temperature mobility (μ), room temperature dark resistivity (ρ), room temperature carrier concentration (n), Fermi level based on room temperature carrier concentration using Nilsson equation [107], activation energy from temperature dependent Hall (E_a), and carrier lifetime (τ). 127

List of Figures

Figure 1.1: Illustration of a potential implementation of a THz imaging systems in (a) transmission mode and (b) reflection mode (reprinted from [3]). 2

Figure 1.2: Radiated flux per steradian versus wavelength of a typical interstellar cloud of material showing the blackbody spectrum at 2.7 and 30 K and several key rotational-vibrational molecular absorption features in the submillimeter range (reprinted from [17]). 4

Figure 1.3: A general photomixer device structure showing the tunable lasers incident on the interdigitated fingers (left), the subsequent photogenerated carriers that are swept by the static electric field (right), and terahertz radiation emitted from the antenna and focused by a hemispherical lens (left)..7

Figure 1.4: Equivalent small-signal circuit model of a photomixer device. The load impedance incorporates the electrode capacitance and the antenna impedance. The current sources represent the current contribution from either electron or holes. 9

Figure 1.5: Steady-state finite element analysis simulation of optical heating with 100% absorption of the incident laser light. The top figure a) shows the full 200 µm thick InP substrate with part of the base heat sunk to 300 K and b) is a zoom-in of the 1.35 µm active region showing the majority of the heat being retained by InGaAs. 15

Figure 1.6: Dark current vs. voltage measurements of photomixer devices with different materials using a 10×10 µm^2 active area with interdigitated electrodes that were 1.8 µm apart (Reprinted from [41]). 16

Figure 1.7: Growth of complete RE-V film (Left) showing the formation of planar defects on the overgrown III-V material and growth of RE-V nanostructures (Right) showing the seeding process utilized to overgrow high quality III-V material (reproduced from [54]). 19

Figure 2.1: Top view schematic of a Mod Gen II MBE chamber with the important components illustrated (Image credit: R. Engel–Herbert, Penn State).23

Figure 2.2: Sample mounting technique recommended by Veeco. It uses two spring plates to suspend the substrate material with minimal contact. The retainer ring holds the sample and spring plates firmly in place in a repeatable way. (reproduced from Veeco Instruments, Inc.) 25

Figure 2.3: Diagram of a typical symmetric *ω-2θ* scan showing the resulting Q vector probing the atomic layers in the growth direction (reprinted from [86]). 31

Figure 2.4: Reciprocal space map around the (224) diffraction peak of InP for a 30 period superlattice of (a) 0.2 ML LaAs:InGaAs and (b) 1.2 ML LuAs:InGaAs. The elongation in the Q parallel direction in (a) is indicative of a mosaic spread for the in-plain lattice parameter. 32

Figure 2.5: Electrical connection to samples for Hall measurements in the van der Pauw configuration. In order to minimize error caused by non-point source contacts, ohmic contacts to the samples must be at the corners of the sample and triangular in shape [90]. 33

Figure 2.6: Illustration of a pump-probe transmission measurement. (a) The pump pulse is absorbed in the semiconductor, exciting electron-holes pairs. (b) Charges begin to recombine in the RE-As nanoparticles, which are fast recombination centers. (c) A large portion of the probe pulse is transmitted through the material when excited states near the band edges are filled due to optical excitation from the pump. (d) Subsequent measurements by probe pulses arriving increasingly after the pump pulse show decreased transmission as the charges begin to recombine and are thus available to absorb photons from the probe pulse. 42

Figure 2.7: Normalized differential transmission of a 1.2 ML LuAs:InGaAs superlattice showing a carrier lifetime of 3.6 ps. The horizontal dashed lines indicate the 90% and 10% transmission used as the end points for the linear fitting. 43

Figure 2.8: General overview of optical station used for time-resolved pump-probe transmission measurements 44

Figure 3.1: Rocksalt lattice parameters of rare-earth arsenide compounds over the range of the lanthanide series. The lattice parameters of several widely-used semiconductor substrates are given along the right edge of the figure. The rare-earth species in this investigation are highlighted by squares..46

Figure 3.2: Superlattice structures grown as (a) photoconductive material with the same deposition of RE-As per period for 30 periods and (b) structures for TEM studies with increasing deposition of RE-As per period from 0.2 ML to 3.0 ML (15 periods). 48

Figure 3.3: RHEED patterns of InGaAs overgrowth after 30 superlattice periods for a) 1.2 ML of LuAs, b) 1.6 ML of LuAs, and c) 0.3 ML of LaAs. The diffraction pattern for the LaAs superlattice after 30 periods degraded for a much lower deposition than other RE-As and appears qualitatively similar to that of the LuAs at 1.6 ML depositions. 49

Figure 3.4: Root-mean-squared surface roughness AFM scans of superlattices with increasing RE-As deposition. Surface morphology of LaAs-containing superlattices degraded at a much lower deposition than other RE-As compounds investigated. 50

Figure 3.5: Cross-sectional TEM study of a) LuAs- and b) LaAs-containing structures with increasing deposition of RE-As per period. LuAs shows good material overgrowth up to 1.6 ML depositions. LaAs has poor quality overgrowth even at 0.2 ML depositions. The contrast variation across the LuAs sample was due to local re-deposition during ion-milling and sample preparation. 51

Figure 3.6: Room-temperature dark resistivity measurements of superlattices as a function of increasing RE-As deposition. Superlattices containing LaAs exhibited significantly higher resistivities than those containing ErAs, LuAs, and GdAs at all depositions. The dashed line represents the resistivity of epitaxial InGaAs. 53

Figure 3.7: Room-temperature electron mobility of superlattices versus increasing RE-As deposition. Both LuAs:InGaAs and GdAs:InGaAs exhibited mobilities uniformly higher than ErAs:InGaAs and significantly higher than LaAs:InGaAs at comparable RE-As depositions.....................54

Figure 3.8: Charge carrier concentration versus inverse temperature showing the linear fits used to extract the activation energy. 55

Figure 3.9: a) Activation energy of RE-As superlattices with various depositions. LaAs shows high activation energies for small deposition of RE-As compared to ErAs, LuAs, and GdAs. b) Band diagrams (1D Poisson) of various superlattices using the activation energy as the Schottky barrier height for the nanoparticle/matrix interface and the room temperature carrier concentration as the doping level. 56

Figure 3.10: Carrier lifetime measurements of superlattices with increasing depositions of RE-As. With the exception of LaAs, lifetime trends correlate with lattice-mismatch between the RE-As and InP. Superlattices containing the nearly lattice-matched GdAs achieved the lowest carrier lifetimes...58

Figure 3.11: Carrier lifetime measurements of a 1.2 ML LuAs:InGaAs superlattice with increasing pump fluences. Carrier lifetime does not seem to be affected by the change in fluence, which suggests that there is no saturation of the states at these power levels. 59

Figure 4.1: AFM images of 0.75 ML deposition of uncovered ErSb nanoparticles grown on GaSb at a) 0.09 ML/s, b) 0.06 ML/s, and c) 0.04 ML/s. The lower deposition rate formed the largest sized nanoparticles and the lowest nanoparticle surface density (reproduced from [70]). 66

Figure 4.2: RHEED patterns of InGaAs overgrowth after 30 superlattice periods of 1.6 ML of LuAs grown at a) 0.07 ML/s without bismuth, b) 0.07 ML/s with bismuth, and c) 0.01 ML/s with bismuth. The diffraction pattern for the superlattice with the combined enhancements appears streakier and the 2× reconstruction is almost visible compared to the superlattice that used only bismuth. 68

Figure 4.3: X-ray diffraction symmetric *ω-2θ* scans around the (004) diffraction peak of InP for 1.6 ML LuAs. The stronger fringe peaks are indicative of smoother and more sharply defined period interfaces. 69

Figure 4.4: Root-mean-squared surface roughness AFM scans of superlattices with increasing LuAs deposition with and without bismuth and different LuAs growth rates. Superlattices that combined both bismuth and slower LuAs growth rate had the lowest surface degradation at the highest depositions of LuAs. 70

Figure 4.5: Cross-sectional TEM study of LuAs-containing superlattice structures with increasing deposition of LuAs per period for LuAs growth rates of a) 0.07 ML/s without using bismuth, b) 0.07 ML/s with bismuth, and c) 0.01 ML/s with bismuth. The superlattice structure that combined both enhancements had the best overall material overgrowth quality. 71

Figure 4.6: Room-temperature dark resistivity measurements of superlattices as a function of LuAs deposition per superlattice period. Superlattices grown with bismuth and a slow LuAs growth rate exhibited significantly higher resistivities than other superlattices except at the 1.6 ML deposition where the growth rate had no apparent effect. The dashed line represents the resistivity of epitaxial InGaAs. 74

Figure 4.7: Room-temperature electron mobility as a function of LuAs deposition for LuAs:InGaAs superlattices. Superlattices that combined bismuth and a slow 0.01 ML/s LuAs growth rate exhibited uniformly higher mobilities than all other superlattices in this investigation. 75

Figure 4.8: Activation energy of LuAs superlattices with increasing LuAs deposition. The superlattices that combined both enhancement techniques had the highest energies..77

Figure 4.9: Band diagram (1D Poisson) of one period of the 2.0 ML LuAs superlattice that used bismuth and 0.01 ML/s LuAs growth rate, showing a diagram that is nearly flatband. The band diagram used the activation energy as the Schottky barrier height and the room temperature carrier concentration as the doping level for the InGaAs. 77

Figure 4.10: Carrier lifetime measurements using differential pump-probe transmission of superlattices with increasing deposition of LuAs. Overall trends in the carrier lifetime seem more affected by the presence of bismuth during growth than by the LuAs growth rate. Superlattices using bismuth with depositions of 2.8 ML of LuAs at 0.01 ML/s achieved the lowest carrier lifetimes at 1.6 ps 79

Figure 5.1: Root-mean-squared surface roughness AFM scans of superlattices with increasing ErAs deposition with different superlattice periods. Superlattices with larger periods delayed the degradation of the surface to higher ErAs depositions. 86

Figure 5.2: Room-temperature dark resistivity of superlattices as a function of ErAs deposition and different period thicknesses. The resistivities seem to level off at different values depending on the period thickness, with the 40 nm period reaching the highest resistivities. The dashed line represents the resistivity of epitaxial InGaAs. 87

Figure 5.3: Room-temperature electron mobility as a function of ErAs deposition and different period thicknesses. The 10 nm and 20 nm periods showed decreasing mobilities with increasing deposition of ErAs. The mobilities for the 40 nm period leveled off at over 4000 cm^2/V-s for several depositions and decreased for ErAs depositions higher than 2.0 ML.88

Figure 5.4: Activation energy of enhanced ErAs superlattices with increasing ErAs deposition and different period thicknesses. Superlattices with 40 nm periods had the highest activation energies. 90

Figure 5.5: Carrier lifetime measurements using differential pump-probe transmission of superlattices with increasing deposition of ErAs and various period thicknesses. Shorter periods had lower lifetimes for the same deposition/period of ErAs, however, the 40 nm periods achieved the lowest overall lifetimes since more ErAs was deposited before the material degraded. 91

Figure 5.6: Room-temperature dark resistivity of enhanced 2.0 ML ErAs:InGaAs superlattices with increasing beryllium doping of the InGaAs host matrix. Doping levels of $1x10^{17}$ achieved the highest resistivity of 7.9 Ω-cm, while the doping level of $1x10^{18}$ pushed the material p-type. The dashed line represents the resistivity of an undoped enhanced 2.0 ML ErAs:InGaAs superlattice. 94

Figure 5.7: Room-temperature carrier mobility of enhanced 2.0 ML ErAs:InGaAs superlattices with increasing beryllium doping in the InGaAs. The dashed line represent the mobility of an undoped superlattice with the same ErAs deposition. 95

Figure 5.8: Carrier lifetime measurements using differential pump-probe transmission of enhanced 2.0 ML ErAs:InGaAs superlattices with increasing beryllium doping. Lifetimes do not seem to change significantly until the $1x10^{17}$ beryllium doping level when the lifetime drops to 1.53 ps. Further doping to $1x10^{18}$ with beryllium turned the material p-type and had the lowest measured lifetime of 0.24 ps....................................96

Figure 6.1: Defect reaction energy for the As (dashed line) and Ga sublattice (solid line) defects. Numbers represent the net charge transfer from the lattice due to the reaction. The Fermi level in light blue between $E_V + 0.6$ eV and $E_V + 0.8$ eV represents the balance in the reaction equations where there is a zero net transfer of charge (reprinted from [146])...........102

Figure 6.2: Band offsets and Fermi stabilization energy in III-V semiconductors. Energy is given relative to the vacuum level. Open circles represent the Fermi level at metal/semiconductor interfaces. Closed circles represent Fermi levels due to heavily irradiated and damaged materials. The dashed lines represent the highest doping levels achieved for GaAs and InP (reprinted from [147]). 103

Figure 6.3: Band alignments of various III-V materials and different Fermi level alignments extracted from Schottky diodes, RT carrier concentrations calculations, and activation energies. The light blue line represents the Fermi stabilization energy...105

Figure 6.4: Band alignments of InGaAs, GaAsSb, and the resulting InGaAsSb quaternary alloy showing the shifting of the band alignments with respect to the Fermi stabilization energy level. All materials are lattice-matched to InP. 106

Figure 6.5: Measurement of the absorbance edge, using FTIR spectroscopy, showing the quaternary alloy is still strongly absorbing at 1550 nm. 107

Figure 6.6: X-ray diffraction symmetric *ω-2θ* scans around the (004) diffraction peak of InP for superlattices with increasing depositions of ErAs(Sb) in InGaAsSb. All materials show very strong period fringes which are related to well-defined period interfaces. The materials show a slight lattice mismatch of the matrix to the InP substrate. 109

Figure 6.7: X-ray diffraction reciprocal space map around the (224) diffraction peak of InP for a 2.0 ML ErAs(Sb):InGaAsSb superlattice. The non-deviating vertical position of the period fringes show a coherently strained material. 109

Figure 6.8: Room-temperature dark resistivity of ErAs(Sb):InGaAsSb superlattices with increasing ErAs(Sb) deposition, compared with the enhanced ErAs:InGaAs superlattices from Chapter 5. 110

Figure 6.9: Room temperature electron mobility of ErAs(Sb):InGaAsSb superlattices with increasing deposition of ErAs(Sb) compared to the enhanced ErAs:InGaAs superlattices from Chapter 5. The ErAs(Sb) superlattices maintained high mobilities even with depositions of 2.0 ML. 111

Figure 6.10: Activation energy of ErAs(Sb):InGaAsSb and enhanced ErAs:InGaAs superlattices with increasing ErAs(Sb) deposition. The activation energy of the quaternary superlattices appears to be leveling off at around 186 meV. 112
Figure 6.11: Carrier lifetime measurements using differential pump-probe transmission of ErAs(Sb):InGaAsSb superlattices and compared with enhanced ErAs:InGaAs superlattices with increasing ErAs(Sb) deposition. The quaternary superlattices achieved on average 2× lower lifetimes than the InGaAs based superlattices. 113
Figure 7.1: Maximum incident laser power calculated for an enhanced 2.0 ML ErAs:InGaAs with Be doping of 1×10^{17} cm^{-3} investigated in Chapter 5 and a 1.75 ML ErAs:InGaAs modulation Be doping superlattice grown by Driscoll [41,73]. 117
Figure 7.2: Figure of merit β as a function of the mixing frequency for an enhanced 2.0 ML ErAs:InGaAs with Be doping of 1×10^{17} cm^{-3} investigated in Chapter 5 and a 1.75 ML ErAs:InGaAs modulation Be doping superlattice grown by Driscoll [41,73] as the electric field intensity of increased from1×10^{5} V/m to 5×10^{6} V/m. 118
Figure 7.3: Maximum calculated output power versus biasing electric field for a 1 THz mixing frequency of photomixer devices using the 2.0 ML ErAs:InGaAs from Chapter 5 and the 1.75 ML ErAs:InGaAs from Driscoll [41,73]. 119

Figure 7.4: Calculated output power versus mixing frequency of photomixer devices using the 2.0 ML ErAs:InGaAs from Chapter 5 and the 1.75 ML ErAs:InGaAs from Driscoll [41,73]. The red dots indicate a device fabricated using Driscoll's 1.75 ML ErAs:InGaAs material and tested by Sukhotin [73]. 120

Figure 7.5: Calculated maximum output power as a function of electric field intensity at 1 THz for the best materials grown during this dissertation (solid lines) and compared to best materials grown by Driscoll [41] and Dietz [68,69] (dashed lines)..121

Figure 7.6: Calculated maximum output power versus mixing frequency for each material's optimal electric field bias for the best materials grown during this dissertation (solid lines) and compared to best materials grown by Driscoll [41] and Dietz [68,69] (dashed lines)...............................122

Chapter 1: Introduction

1.1 Motivation and Application for Terahertz Sources

The terahertz (THz) range of the electromagnetic spectrum corresponds to photon frequencies between 0.1 THz and 10 THz. However, only the portion of these frequencies between 0.3 THz to 3 THz is commonly referred to as the submillimeter-wave or THz region [1]. Although the THz region has been explored scientifically with great interest since the early 1920's [2], it remains largely untapped commercially due the lack of compact low-cost sources and components. Applications for THz technology can be separated into two general categories, imaging and spectroscopy [1,3,4]. Imaging systems, which generate their own THz radiation, can be further subdivided into transmission or reflection detection to determine the shape or the composition of a particular material. Spectroscopic applications can also be subdivided into generation and detection for short range sensing or detection through a heterodyne receiver.

Imaging in the THz region has been proposed as a solution for locating, detecting and characterizing concealed threats for security applications as shown in Figure 1.1. THz radiation is transmitted through most plastics, clothing, and other non-metallic materials, thus it can be used for security checkpoint scanning. Additionally, due to THz radiation's shorter wavelength, spatial resolutions up to ten times higher than the more standard millimeter wave imaging technology can be achieved [3]. Consequently, detection of possible threats can then be further analyzed and characterized due to the spectroscopic nature of the imaging system. Medical applications also stand to benefit from non-invasive reflection mode THz imaging as it can be used in the detection of cancerous cells [5,6], health and composition of teeth [7,8], liver tissue cirrhosis [9], and

skin burn healing progress through protective layers of gauze which would allow for real time non-invasive monitoring and treatment [10].

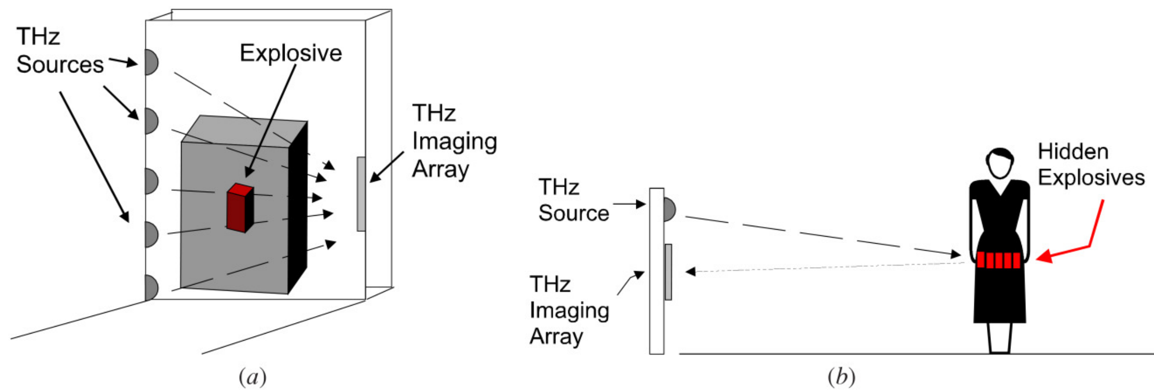

Figure 1.1: Illustration of a potential implementation of a THz imaging systems in (a) transmission mode and (b) reflection mode (reprinted from [3]).

Coherent THz sources play an important role in spectroscopic applications since the rotational-vibrational absorption and emission line features of many light molecules tend to lie within the THz range. Some security applications include rapid short range detection of volatile gases for identification of explosives, illegal drugs, and chemical leaks [3]. Another medical application that would greatly benefit from the use of compact THz sources includes spectroscopy of exhaled volatile biomarker molecules that can be potentially used in the diagnosis of diseases [11]. Plasma fusion diagnostic techniques are also an important application for THz spectroscopy as it can be used for modeling and tracking of the electron density profiles in the plasma, plasma turbulence, and temperature fluctuations in order to maintain power balance in the reactor cores [12-14].

THz spectroscopy applications abound for space-based astronomical instruments, as evidenced by the spectral signature of an interstellar cloud (Figure 1.2). In addition to the many molecular rotational-vibrational absorption features, the THz spectrum also

corresponds to equivalent blackbody temperatures ranging from 14 to 140 K, which are below the ambient background of the Earth and require space-based detection. The majority of the interstellar THz spectrum has yet to be explored due to interference from terrestrial atmospheric absorption and the high resolution required from sources to accurately measure and separate the different spectral features. Experimental results from the NASA Cosmic Background Explorer show that nearly half of the total luminosity emitted from the Big Bang resides in the submillimeter and far-IR range [15]. Red shifted spectral lines from galaxies forming in the early universe that are no longer optically visible are also a major detection challenge for astronomy today since they lie almost exclusively in the THz region. Star formation studies in our own galaxy also stand to benefit greatly from THz spectroscopy since measurements of the different molecular species within the dense clouds of gas and dust allow for more complete astrophysical models that include temperature, movement of different materials, and isotope densities [16]. Exploration of planetary and cometary atmospheres offer yet another important use for THz spectroscopy as detection of certain molecular species offer an insight into surface processes that might not be otherwise detectable. Some of these processes include the role of HCl in terrestrial planets, the formation of H_2O_2 from the electrical discharges in the Martian atmosphere, and the ratio of non-deuterated to deuterated water across our solar system, each of which provide insight into the evolution of the early solar system [16].

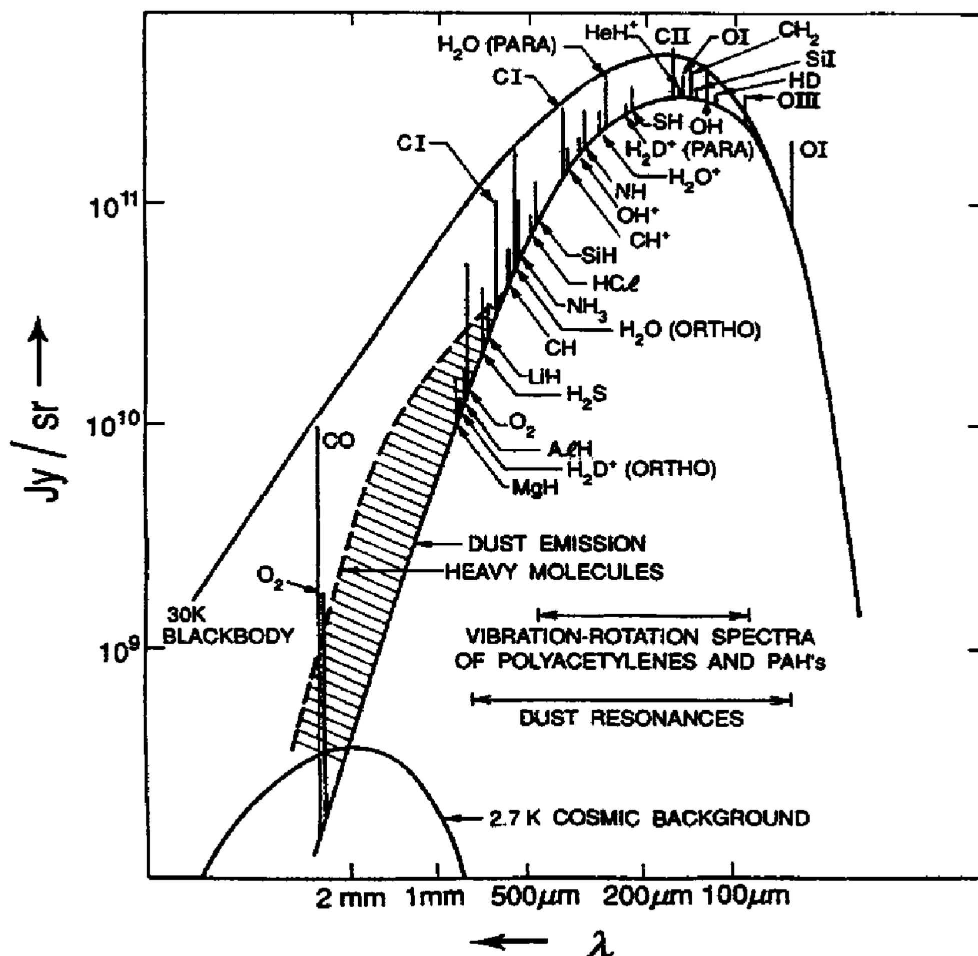

Figure 1.2: Radiated flux per steradian versus wavelength of a typical interstellar cloud of material showing the blackbody spectrum at 2.7 and 30 K and several key rotational-vibrational molecular absorption features in the submillimeter range (reprinted from [17]).

1.2 Terahertz Sources

Although THz science and technology have made remarkable progress over the last several decades, large and power-hungry THz generators like gas lasers, free electron lasers, backward wave oscillators, and vacuum-tube based devices would not be appropriate for many of the applications already mentioned. However, despite the great

need for compact, high-power, broadly-tunable, continuous-wave (CW) THz sources, the development pace of these devices has remained ponderous. Design efforts have approached the problem from the high frequency side of RF devices and from the low frequency side of optical devices. High frequency RF devices such as resonant tunneling diodes [18], Gunn diodes [19,20], and impact ionization avalanche transit time (IMPATT) diodes [21] utilize negative differential resistance (NDR) in the semiconductors to generate oscillations. Resonant tunneling diodes exploit the voltage-controlled tunneling in a quantum well to create the NDR and as such are not broadly tunable since the quantum well resonance frequency is highly dependent on the device structure [22-24]. Gunn diodes utilize intervalley scattering of carriers from high mobility to low mobility valleys to create NDR, but managing the parasitic heat generation is problematic [20]. IMPATT diodes use the delay from impact ionization and transit times to create a current-voltage lag that produces NDR, but the operating frequency is limited by the material parameters for standard substrate materials [21]. Frequency-multiplied Schottky diodes lose an order of magnitude in output power for every frequency doubling stage, requiring hundreds of watts of input power to generate a few milliwatts in the THz region, making them prohibitively power consumptive [25].

From the optical side of the spectrum, quantum cascade lasers (QCL) offer a promising compact solid-state THz source [26]. Intersubband QCLs use the alignment of subbands in the conduction band from stacked quantum wells to separate the energy levels required to generate photons in the THz range. However, these devices require cryogenic cooling in order to operate in CW mode, due to phonon energies becoming comparable to the THz energy at room temperature and causing non-radiative relaxation mechanisms. A promising QCL approach employs intracavity difference frequency generation (DFG) to produce THz [27]. Further optimization of this approach uses a

Cherenkov phase-matching scheme to produce THz at an angle to the generated mid-infrared lasers to minimize THz absorption by the material [28]. This THz generation method can then be coupled with two distinct distributed feedback gratings to lock the dual color of the lasers for DFG [29]. Tunability of these enhanced QCL devices has been improved by up to 580 GHz, the largest by a room-temperature monolithic THz QCL, by independently controlling the biasing scheme of two distributed feedback gratings [30]. However, the broad range tunability of these lasers over the whole THz region remains uncertain without the need of external cavity gratings [29].

Heterodyne down-conversion offers a promising path to generate coherent THz radiation. Optical heterodyning, or photoconductive mixing, was first proposed over fifty years ago as a method for generating millimeter wave radiation [31]. However, only within the last couple of decades have photomixer devices been developed to generate wavelengths in the THz region under CW operation [32-34]. Photomixers have several advantages over all the previous devices, since they operate at room temperature, can be operated in CW or pulsed mode, and are inherently broadly tunable across the THz region via the tunability of the pumping lasers. There are however some limitations to the photomixer that are dependent on the photoconductive material properties which will be the main focus of this thesis investigation.

1.3 Photomixer Theory

The general photomixer structure is shown in Figure 1.3. The active area of the device is a metal-semiconductor-metal photodetector composed of a set of interdigitated metal electrodes biasing the underlying semiconductor with a voltage potential. This region is then illuminated by two continuous-wave single mode lasers at two frequencies,

ν_1 and ν_2. The spatial overlap of the lasers creates an interference pattern that modulates the conductivity of the semiconductor material at the difference beat frequency of the two lasers. The static electric field across the metal electrodes induces a photogenerated current at the beat frequency that is subsequently coupled into a planar antenna patterned on the surface of the material. The antenna receives the signal and emits the majority of the radiation into the photoconductive material due to the high dielectric constant compared to air. A silicon hemispherical lens is placed on the back of the material to collect and collimate the THz radiation emitted from the antenna.

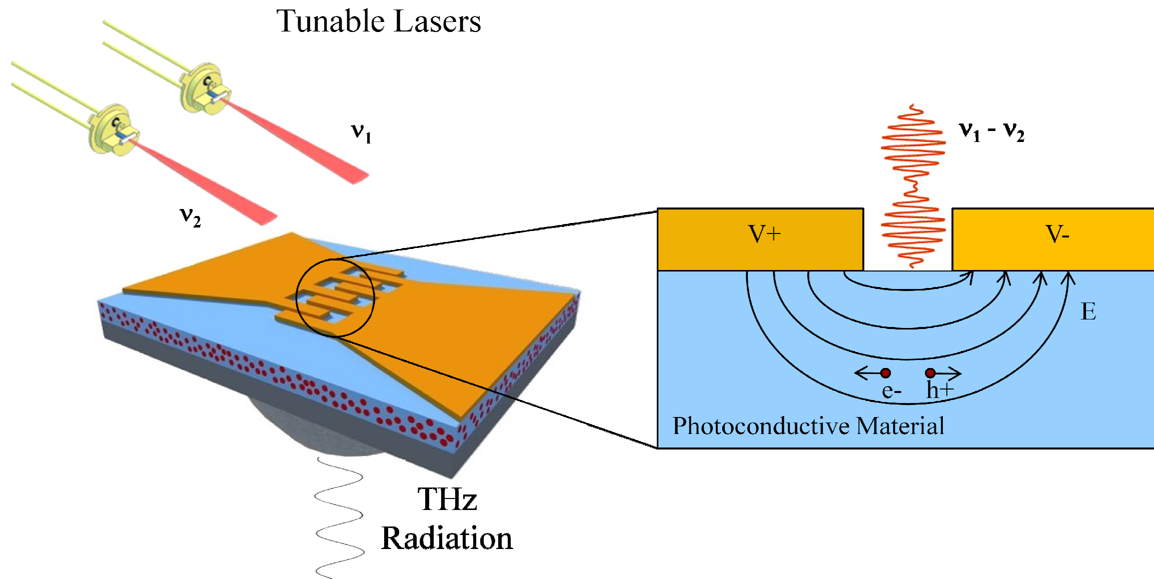

Figure 1.3: A general photomixer device structure showing the tunable lasers incident on the interdigitated fingers (left), the subsequent photogenerated carriers that are swept by the static electric field (right), and terahertz radiation emitted from the antenna and focused by a hemispherical lens (left).

The photomixing process begins with the illumination of the interdigitated electrode region by two lasers with average optical powers P_1 and P_2 and radial

frequencies ω_1 and ω_2, respectively. From heterodyne theory the instantaneous optical power incident on the material is given by [35]

$$P = P_1 + P_2 + 2\sqrt{mP_1P_2}[\cos(\omega_1 - \omega_2)t + \cos(\omega_1 + \omega_2)t], \qquad (1.1)$$

where m is the mixing efficiency that ranges between 0 and 1 depending on the spatial overlap of the two incident lasers. The first cosine term modulates the photoconductivity of the material at the difference frequency and can be tuned by adjusting the incident laser frequencies. The second cosine term corresponds to the sum frequency which can be neglected since it is too fast to modulate the photoconductance significantly and can be considered to minimally add to the DC photo-generated current [34]. By substituting the difference frequency $\omega_1 - \omega_2$ with simply ω and assuming that $P_1 \approx P_2$, the incident optical power simplifies to

$$P_0 = P'(1 + \cos\omega t), \qquad (1.2)$$

where P' is the sum of the two incident laser powers P_1 and P_2 and m is taken to be approximately 1. The generated photocurrent in the material can be expressed as [36]

$$I_0 = \eta_e \left(\frac{e}{h\nu}\right) P_0, \qquad (1.3)$$

where η_e is the external quantum efficiency that incorporates the conversion of the optical signal into an electrical signal and is highly dependent on the material properties, e is the elementary charge, and $h\nu$ is the photon energy of the incident lasers.

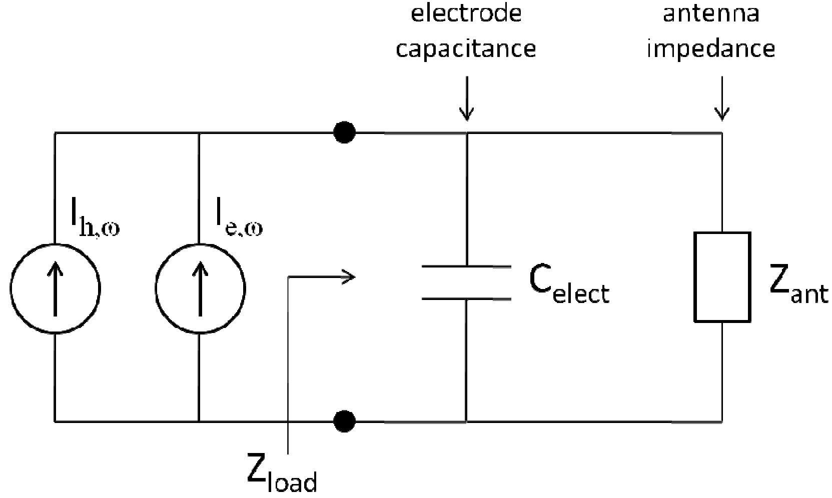

Figure 1.4: Equivalent small-signal circuit model of a photomixer device. The load impedance incorporates the electrode capacitance and the antenna impedance. The current sources represent the current contribution from either electron or holes.

The small signal model of the photomixer is shown in Figure 1.4. Due to the low conductance of the photomixer, the active region can be approximated by two current sources connected to a load impedance, which is composed of the electrode capacitance in parallel with the antenna impedance. The electrode capacitance can be a troubling factor in the photomixer design since it tends to short out the device at high frequencies. The THz output power of the photomixer can then be calculated using this small signal approximation as

$$P_\omega = \frac{1}{2} I_\omega^2 \frac{\eta_{ant} R_A}{\left(1 + \left(\omega R_A C_{elect}\right)^2\right)} = \frac{1}{2} I_\omega^2 \eta_{ant} \operatorname{Re}\left(Z_{Load}\right), \tag{1.4}$$

where R_A is the real part of the antenna impedance, η_{ant} is the antenna efficiency, and $\operatorname{Re}(Z_{load})$ is the real part of the antenna impedance lumped with the capacitive load of the interdigitated electrodes. The magnitude of the relevant small-signal THz current is given by

$$\left|I_\omega\right| = \frac{I_0}{\sqrt{1 + \omega^2 \tau^2}}, \tag{1.5}$$

where τ is the effective carrier lifetime in the material, and I_0 is the generated photocurrent.

To examine how a specific material's properties can affect the overall THz output power of a photomixer, we have to look at the factors included in the external quantum efficiency, η_e. The external quantum efficiency is defined as the integral of the absorption factor f and the photoconductive gain g over the volume of the active region. The absorption factor f can be considered to be the fraction of photons that generate carriers, while the photoconductive gain g can be considered to be the fraction of generated charges that induce a current per absorbed photon [37]. The external quantum efficiency is then

$$\eta_e = \int_V f\, g \frac{dv}{V} = \int_V \frac{P_A}{PV} g\, dv \,, \tag{1.6}$$

where V is the volume of the active region, P_A is the absorbed power and P is the incident power. The photoconductive gain g is defined as the ratio of the individual carrier lifetimes over their respective transit times between electrodes, by utilizing the thermal velocity of the charges the gain becomes

$$g = \frac{\tau_e}{t_e} + \frac{\tau_h}{t_h} = \frac{\tau_e v_e}{L_e} + \frac{\tau_h v_h}{L_h} \,, \tag{1.7}$$

where L_e and L_h are the lengths of the carrier paths from electrode to electrode that follow the electric field and v_e and v_h are the respective charge velocities. The velocity of each of the charges can be substituted by the relation

$$v = \frac{\mu E}{1 + \mu E / v_{sat}} \,, \tag{1.8}$$

where v_{sat} is the saturation velocity for each respective charge. If the distance between electrodes is much larger than the thickness of the photoconductive material, d, then the

electric field can be assumed to be parallel to the surface and L_e and L_h approximate the spacing between electrodes L, thus leading to an expression for g

$$g \approx \left(\frac{\mu_e \tau_e}{1+\mu_e E/v_{e,sat}} + \frac{\mu_h \tau_h}{1+\mu_h E/v_{h,sat}} \right) \frac{E}{L}, \tag{1.9}$$

where μ_e and $v_{e,sat}$ (μ_h and $v_{h,sat}$) represent the mobility and saturation velocity of the electrons (holes) respectively and E is the electric field resulting from the voltage, V_{bias}, applied between electrodes. This first order approximation removes the spatial dependence of the photoconductive gain from the integral in Equation 1.6. By further assuming that the absorption can be modeled by the Lambert-Beer law, the external quantum efficiency can be approximated by

$$\eta_e \approx (1-e^{-\alpha d})\eta_{opt}\, g = (1-e^{-\alpha d})\eta_{opt} \left(\frac{\mu_e \tau_e}{1+\mu_e E/v_{e,sat}} + \frac{\mu_h \tau_h}{1+\mu_h E/v_{h,sat}} \right) \frac{E}{L}, \tag{1.10}$$

where α is the absorption coefficient and η_{opt} is the optical efficiency which accounts for the reflection loss of the pump lasers incident from the air into the active region due to their difference in index of refraction and the shadowing effect by the metallic electrodes on the photoconductive material. The optical efficiency is then defined as

$$\eta_{opt} = \frac{L}{L+L_{electrode}} \frac{4n}{(n+1)^2}, \tag{1.11}$$

where n is the refractive index of the photoconductive material at the laser pump frequency and $L_{electrode}$ is the width of the electrode. Plugging in Equation 1.3 and 1.5 into Equation 1.4, using the approximated external quantum efficiency from Equation 1.10, and taking into account the different current contributions from electrons and holes as if each were an independent current source with their own impedance loads [38], the expression for the THz output power from the photomixer can be obtained as

$$P_\omega = \left[\left(\frac{(1-e^{-\alpha d})\eta_{opt}\mu_e\tau_e}{(1+\mu_e E/v_{e,sat})\sqrt{1+\omega^2\tau_e^2}} + \frac{(1-e^{-\alpha d})\eta_{opt}\mu_h\tau_h}{(1+\mu_h E/v_{h,sat})\sqrt{1+\omega^2\tau_h^2}}\right)\frac{E}{L}\right]^2 \cdot \left[\left(\frac{e}{h\nu}\right)P_o\right]^2 \frac{\eta_{ant}\,\mathrm{Re}(Z_{Load})}{2}. \quad (1.12)$$

The material dependent portion can be extracted and defined as

$$\beta(\omega,E) = \left(\frac{(1-e^{-\alpha d})\eta_{opt}\mu_e\tau_e}{(1+\mu_e E/v_{e,sat})\sqrt{1+\omega^2\tau_e^2}} + \frac{(1-e^{-\alpha d})\eta_{opt}\mu_h\tau_h}{(1+\mu_h E/v_{h,sat})\sqrt{1+\omega^2\tau_h^2}}\right)\frac{E}{L}, \quad (1.13)$$

$$\beta(\omega,E) = \frac{\eta_{e,electron}}{\sqrt{1+\omega^2\tau_e^2}} + \frac{\eta_{e,hole}}{\sqrt{1+\omega^2\tau_h^2}}, \quad (1.14)$$

where $\eta_{e,electron}$ ($\eta_{e,hole}$) is the external quantum efficiency for electrons (holes). The equation for the output power of the photomixer can then be written as follows

$$P_\omega = \beta^2(\omega,E)\left[\left(\frac{e}{h\nu}\right)P_0\right]^2 \frac{\eta_{ant}\,\mathrm{Re}(Z_{Load})}{2}, \quad (1.15)$$

The figure of merit $\beta(\omega,E)$ shows how the mobility and carrier lifetimes each affect the overall response of the material to external stimuli, but it also shows the significance of having a high breakdown field and high absorption coefficient. For the investigation in this dissertation, the photoconductive materials are assumed to be sufficiently thick to absorb the majority of the incident laser light such that the absorptivity $A = (1-e^{-\alpha d}) \approx 1$. An index of refraction of 3.43 for InGaAs at 1550 nm will also be used. The velocity saturation for electrons in InGaAs that will be used for subsequent numerical analysis is 1.3×10^7 cm/s [39]. In addition, numerical analysis clearly shows that the electron properties dominate the value of $\beta(\omega,E)$ and as such we will neglect the contribution due to holes. The $\beta(\omega,E)$ can then be approximated by

$$\beta(\omega,E) \approx \frac{(1-e^{-\alpha d})\,\eta_{opt}\mu_e\tau_e}{(1+\mu_e E/v_{e,sat})\sqrt{1+\omega^2\tau_e^2}}\frac{E}{L} = \frac{\eta_{e,electron}}{\sqrt{1+\omega^2\tau_e^2}}, \quad (1.16)$$

and is essentially the frequency dependent electron external quantum efficiency.

1.4 Photomixer Thermal Considerations

The main failure mechanism of photomixer devices is thermal degradation due to ohmic heating and optical absorption. A more in-depth discussion of thermal considerations can be found in the work by Jackson [40]. Assuming a change in temperature in the device, ΔT_{max}, is the limiting factor, the thermal power dissipated can be used to find the maximum input optical power incident on the active region,

$$Q_{thermal} = A\,\eta_{opt}\,P_{0,RMS} + V_{Bias}(I_{ph} + I_{Dark}) = \frac{\Delta T_{\max}}{\theta}, \qquad (1.17)$$

where $P_{0,RMS}$ is the average RMS power delivered by the lasers and is equal to $\sqrt{3/2}\,P'$, P' is the sum of the laser powers from Equation 1.2, θ is the thermal impedance, A is the effective optical absorption or absorptivity, η_{opt} is the optical efficiency, I_{ph} and I_{Dark} are the photogenerated and dark currents respectively. Rearranging Equation 1.17 and substituting in the average RMS input power P' yields the maximum input power that can be applied incident on the device,

$$\frac{\Delta T_{\max}}{\theta} - \frac{E^2 L^2}{R_{dark}} = A\eta_{opt}\sqrt{\frac{3}{2}}P' + \frac{A\eta_{opt}\mu_e\tau_e}{\left(1+\mu_e E/v_{e,sat}\right)}E^2\left(\frac{e}{h\nu}\right)\sqrt{\frac{3}{2}}P' \qquad (1.18)$$

$$P'_{\max} = \frac{\dfrac{\Delta T_{\max}}{\theta} - \dfrac{E^2 L^2}{R_{dark}}}{A\eta_{opt}\sqrt{\dfrac{3}{2}}\left(1 + \dfrac{\mu_e\tau_e}{\left(1+\mu_e E/v_{e,sat}\right)}E^2\left(\dfrac{e}{h\nu}\right)\right)}, \qquad (1.19)$$

where L is the spacing between the electrodes and $V_{Bias} = E\,L$. It is important to note how strongly dependent on the applied electric field this equation is when the dark current is considered.

Thermal simulations were carried out using a 2D finite element analysis software to analyze the thermal dissipation of the optical heat load. A 1.35-µm layer of InGaAs on top of a 200-µm InP substrate were modeled with part of the base of the InP thermally shorted to a 300 K element to give a rough estimate of the thermal conditions. The

incident laser power was increased until a maximum temperature difference of 110° was reached, the same failure point condition observed experimentally by Jackson for low-temperature-grown GaAs/GaAs photomixers [40]. This may not necessarily be the same ΔT_{max} that can be reached for InGaAs/InP photomixers, but it is a good starting approximation since the thermal conductivities of the materials, shown in Table 1.1, are similar to each other for both systems. Based on the modeled geometry, the results of the thermal simulation show that an incident fully-absorbed heat load of 24 mW spread across a square active area of 100 μm^2 was sufficient to increase the temperature of the material to 110° above room temperature. This set the $\Delta T_{max}/\theta$ in Equation 1.19 to 24 mW and will be used in numerical analysis work in Chapter 7.

Table 1.1: Thermal conductivity of various semiconductor materials

Semiconductor Material	Thermal Conductivity (W/m-K)
LTG-GaAs	15
GaAs	44
InGaAs	5.5
InP	68

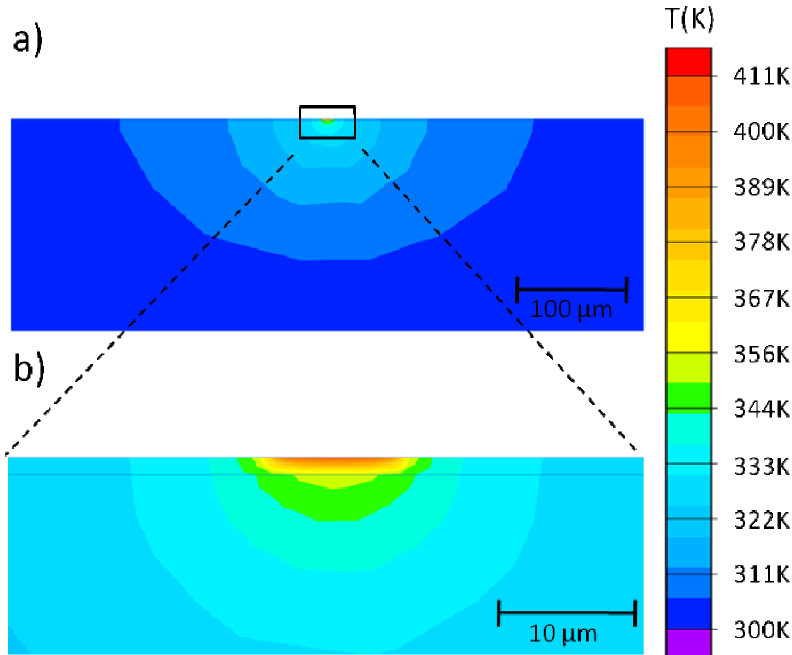

Figure 1.5: Steady-state finite element analysis simulation of optical heating with 100% absorption of the incident laser light. The top figure a) shows the full 200 µm thick InP substrate with part of the base heat sunk to 300 K and b) is a zoom-in of the 1.35 µm active region showing the majority of the heat being retained by InGaAs.

Due to the complex nature of the interdigitated electrodes, dark resistances can be calculated from the dark resistivities by first extracting out the volumetric constant from a measured device. The resistance is given by the equation

$$R = \frac{\rho d}{A} = \rho K, \tag{1.20}$$

where ρ is the resistivity, d is the depth of the material, A is the area, and K is the effective geometry. It is clear that the K is simple for rectangular resistances but not for interdigitated electrodes. Using measurements by Driscoll of a photomixer structure with a $10\times10\ \mu m^2$ active region, shown in Figure 1.6, the geometry-dependent K value can be extracted from I-V measurements of the dark current. Referring to the device with Be δ-doping, the extracted K value is

$$K = \frac{R}{\rho} = \frac{V}{I\,\rho} = \frac{20V}{(0.3\,mA)(225\,\Omega\,cm)} = 296\,cm^{-1}. \tag{1.21}$$

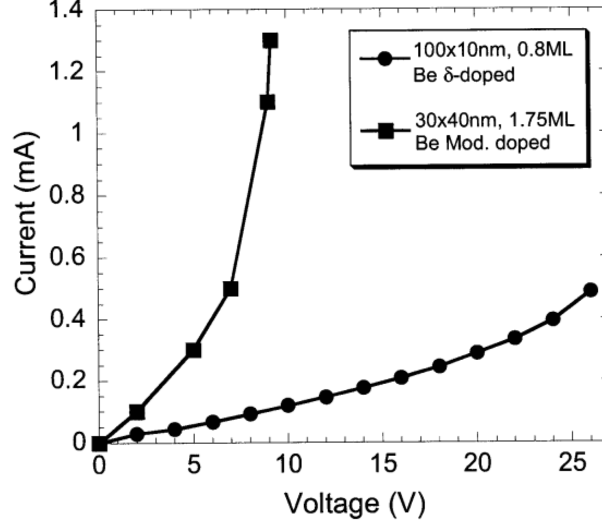

Figure 1.6: Dark current vs. voltage measurements of photomixer devices with different materials using a 10×10 μm^2 active area with interdigitated electrodes that were 1.8 μm apart (Reprinted from [41]).

The maximum input power equation then becomes

$$P'_{\max} = \frac{\dfrac{\Delta T_{\max}}{\theta} - \dfrac{E^2 L^2}{\rho K}}{A\eta_{opt}\sqrt{\dfrac{3}{2}}\left[1 + \dfrac{\mu_e \tau_e}{\left(1 + \mu_e E / v_{e,sat}\right)} E^2 \left(\dfrac{e}{h\nu}\right)\right]}, \tag{1.22}$$

and subsequently

$$P_{0,\max} = P'_{\max}\left(1 + \cos\omega t\right). \tag{1.23}$$

The maximum total output power of a photomixer device then becomes

$$P_{out}^{\max} = \frac{I_{ph}^{\max\,2}}{(1+\omega^2\tau_e^2)} \frac{\eta_{ant}\,\mathrm{Re}(Z_{load})}{2} = \left(\beta(\omega,E)\left(\frac{e}{h\nu}\right)P_{0,\max}\right)^2 \frac{\eta_{ant}\,\mathrm{Re}(Z_{load})}{2} \tag{1.24}$$

$$P_{THz,out}^{\max} = \left[\frac{A\eta_{opt}\mu_e\tau_e}{\left(1+\mu_e E/v_{e,sat}\right)} \frac{E}{L}\left(\frac{e}{h\nu}\right) \frac{\dfrac{\Delta T_{\max}}{\theta} - \dfrac{E^2 L^2}{\rho K}}{A\eta_{opt}\sqrt{\dfrac{3}{2}}\left[1+\dfrac{\mu_e\tau_e}{\left(1+\mu_e E/v_{e,sat}\right)}E^2\left(\dfrac{e}{h\nu}\right)\right]} \right]^2 \frac{\eta_{ant}\,\mathrm{Re}(Z_{load})}{2(1+\omega^2\tau_e^2)}$$

(1.25)

$$P_{THz,out}^{\max} = \left[\frac{\dfrac{\sqrt{2/3}\,\mu_e\tau_e}{\left(1+\mu_e E/v_{e,sat}\right)} \dfrac{E}{L}\left(\dfrac{e}{h\nu}\right)\left(\dfrac{\Delta T_{\max}}{\theta} - \dfrac{E^2 L^2}{\rho K}\right)}{\left[1+\dfrac{\mu_e\tau_e}{\left(1+\mu_e E/v_{e,sat}\right)}E^2\left(\dfrac{e}{h\nu}\right)\right]} \right]^2 \frac{\eta_{ant}\,\mathrm{Re}(Z_{load})}{2(1+\omega^2\tau_e^2)}. \tag{1.26}$$

$$P_{THz,out}^{\max} = \left[\frac{\dfrac{\sqrt{2/3}\,\mu_e\tau_e}{\left(1+\mu_e E/v_{e,sat}\right)} \dfrac{E}{L}\left(\dfrac{e}{h\nu}\right)\left(\dfrac{\Delta T_{\max}}{\theta} - \dfrac{E^2 L^2}{\rho K}\right)}{\left[1+\dfrac{\mu_e\tau_e}{\left(1+\mu_e E/v_{e,sat}\right)}E^2\left(\dfrac{e}{h\nu}\right)\right]} \right]^2 \frac{\eta_{ant} R_A}{2(1+\omega^2\tau_e^2)\left(1+\left(\omega R_A C_{elect}\right)^2\right)}. \tag{1.27}$$

Equation 1.27 explicitly relates the maximum possible output power based on the material properties, the applied electric field, the desired output frequency, and the antenna impedance parameters. This equation will be used in Chapter 7 to rank the maximum THz output power of different materials.

1.5 Photoconductive Materials for Photomixers

Suitable photoconductive materials, as expressed from Equation 1.13, must exhibit high carrier mobilities and carrier lifetimes on the order of the period of the intended frequency to increase the photoconductive response of the material. Equation 1.15 also shows that the applied electric field or bias voltage across the electrodes is squared proportional to the output power, so a potential material must also possess a high breakdown field. From Equation 1.27, we see that a high dark resistivity is also required to maximize the input power that drives the devices and prevent thermal failure due to

ohmic heating. The following section describes the evolution of several material systems previously investigated as candidates for photomixer devices.

1.5.1 Low-Temperature-Grown GaAs

Early work on photomixer devices performed by the Lincoln Laboratories group [35] focused on low-temperature-grown (LTG) GaAs, which was first introduced by Smith *et al.* [42]. GaAs, when grown at substrate temperatures between 200 °C and 300 °C by molecular beam epitaxy (MBE), resulted in a non-stoichiometric material with excess incorporated arsenic [43]. The excess arsenic can be incorporated as As antisite crystal defects or as As metallic clusters, the ratio varying depending on the growth conditions. The As metallic clusters act as buried Schottky barriers and fast carrier recombination centers [44]. These materials were found to have several desirable properties, including sub-picosecond carrier lifetimes and very high dark resistivities [45], which led to their use in fast photodetectors [46] and photomixers [35]. Further work on optimizing LTG-GaAs-based photomixers was led by Jackson [40], who articulated the importance of thermal management during both the growth process and the operation of the device.

1.5.2 ErAs / GaAs Nanocomposites

Rare-earth group-V (RE-V) monopnictides were extensively researched by Palmstrøm's group [47] and found to be well-suited for expitaxial growth with other III-V materials using MBE. ErAs on GaAs, the most widely studied rare-earth system, was found to grow in an embedded island growth mode [48,49] before coalescing into films that subsequently grew in a layer-by-layer mode [47]. However, subsequent growths of

GaAs on films of ErAs follow a Volmer-Weber growth mode that is predicated on the mismatch of the surface energies and wetting differences of the two materials [50]. This leads to nucleation of GaAs islands on the ErAs films that then coalesce into films. Due to the 4-fold rotational symmetry of the rocksalt crystal structure of RE-V materials, the coalesced GaAs film (2-fold rotational symmetry) exhibits planar defects and anti-phase domains at the grain boundaries. Further work by Kadow and Ibbetson [51-53] showed that self-assembled nanoparticles of ErAs could be successfully overgrown with high quality GaAs, if the GaAs growth began before the ErAs nanoparticles coalesced into a full film. The GaAs overgrowth is seeded by the underlying GaAs exposed between the nanoparticles and would maintain the crystal orientation of the substrate. Figure 1.7 shows the different growth methods described for the film and nanoparticle overgrowth.

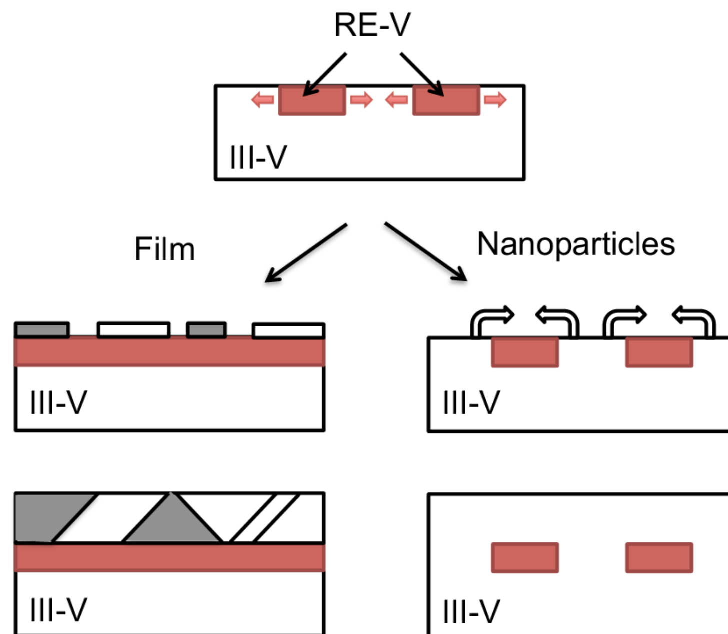

Figure 1.7: Growth of complete RE-V film (Left) showing the formation of planar defects on the overgrown III-V material and growth of RE-V nanostructures (Right) showing the seeding process utilized to overgrow high quality III-V material (reproduced from [54]).

Nanocomposite structures of self-assembled ErAs nanoparticles embedded in GaAs also showed material properties similar to those of LTG-GaAs, such as high dark resistivity [55] and short carrier lifetimes [56]. Photomixer performance based on these composite materials were also shown to be comparable to those of LTG-GaAs [55,57,58]. Further studies showed that the epitaxially embedded nanoparticles had a similar structure as the As metallic clusters found in LTG-GaAs, but the shape, size, density, and separation length could be more easily controlled by the growth conditions [59,60]. There are many benefits of the ErAs/GaAs system compared to LTG-GaAs: the RE-As systems can be grown at standard GaAs growth temperatures and are more robust to temperature changes during growth; the structures do not require post-growth anneal processes; and the material parameters like carrier lifetime can be tuned by changing the period spacing in superlattice structures and deposition of the ErAs [53].

1.5.3 Small Bandgap Materials and Nanocomposites

Due to the telecommunication industry, there is a wide variety of mature photonic components and technology developed that operates at 1550 nm. Fast photoconductive materials with bandgaps in this regime have been pursued in order to take advantage of this infrastructure [61]. However, despite considerable effort with InP-based nipnip [62,63] and uni-traveling carrier [64,65] diodes, plasmonic enhancements [66], and mixers with promising materials such as LTG-InGaAs [67] and LTG-InGaAs/AlGaAs multilayer heterostructures [68,69], the output powers of photomixers developed using these small bandgap materials remain in the low microwatt range.

ErAs nanocomposite materials based on InGaAs superlattice structures similar to the ErAs/GaAs system were investigated by Driscoll and Hanson [41,70]. ErAs

nanoparticles were found to have a very similar microstructure when grown in InGaAs as when grown in GaAs [71], but had prohibitively low dark resistivities [72,73]. Unlike the LTG-GaAs and ErAs/GaAs systems where the Fermi level alignment at the interface of the As-precipitates/GaAs and ErAs/GaAs is near the midgap, ErAs aligns near the conduction band in InGaAs [72]. The alignment difference significantly changes the properties of the resulting nanocomposite. Driscoll attempted to lower the Fermi level alignment closer to the midgap through a series of Be doping profiles, changes in the deposition of the ErAs, and by varying the superlattice period spacing [41]. Dark resistivities of these enhanced nanocomposites improved, achieving a maximum of 502 Ω-cm. Carrier lifetimes were ~0.3 ps, suitable for THz photomixers, but the carrier mobilities suffered, reaching a maximum of 202 cm^2/V-s. Devices based on these enhanced materials achieved output THz powers in the hundreds of nanowatts [73].

1.6 Organization of Dissertation

The work presented in this dissertation aims to further improve the properties of small bandgap materials to increase output powers of photomixers based on them while pumped by 1550 nm laser sources. The structure of this thesis is organized as follows: Chapter 2 will give a brief introduction to molecular beam epitaxy and characterization techniques. Chapter 3 will introduce a study of several RE-As species (Erbium, Gadolinium, Lutetium, and Lanthanum) embedded in an $In_{0.53}Ga_{0.47}As$ matrix lattice-matched to InP in a superlattice structure, where the RE atoms were interchanged to investigate the effect of different innate elemental properties and/or strain on the photoconductive properties. Chapter 4 will explore the effect of different growth enhancement techniques such as surfactant-mediated growth of the $In_{0.53}Ga_{0.47}As$ matrix

and different RE-As growth rates to change the nanoparticle morphology. Chapter 5 will use the enhancement techniques from Chapter 4 to optimize the properties by changing the RE atom once again, changing the period thickness of the superlattice structure, and counter doping the material with beryllium. Chapter 6 will explore an alloy of $In_{0.53}Ga_{0.47}As$ and $GaAs_{0.5}Sb_{0.5}$ lattice-matched to InP for use as the matrix for the RE-As nanoparticles to change their Fermi level alignment within the bandgap of the matrix as a method to further improve the nanocomposites. Chapter 7 will compare the measured properties of the best superlattices from the previous chapters and simulate the output powers of potential photomixer devices. Finally, Chapter 8 will provide some discussion on the use of RE-V nanostructures in III-V materials as photoconductive materials for THz photomixing and suggest avenues to further improve the materials for use in devices.

Chapter 2: Molecular Beam Epitaxy and Material Characterization

Molecular beam epitaxy (MBE) is an ultra-high vacuum (UHV) epitaxial crystal growth technique that was developed in the 1960's and early 1970's at Bell Laboratories by Alfred Y. Cho and by J. R. Arthur [74,75]. MBE was developed as a method to grow high-purity epitaxial GaAs and study its kinetic growth processes [76,77]. MBE is preferred by many researchers because it allows for precise monolayer level control of material thicknesses, atomically abrupt interfaces, precise compositions, and high quality crystalline materials. Such control over the growth processes becomes important when creating and growing new materials. This chapter goes into more detail about the MBE system, growth of materials by MBE, and characterization techniques utilized in this dissertation.

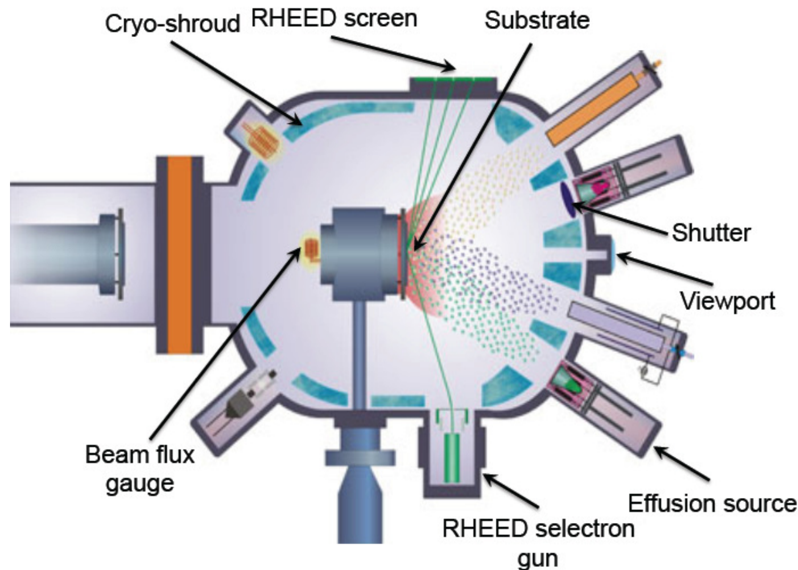

Figure 2.1: Top view schematic of a Mod Gen II MBE chamber with the important components illustrated (Image credit: R. Engel–Herbert, Penn State).

2.1 Molecular Beam Epitaxy

Figure 2.1 shows a schematic top view of a typical MBE growth chamber with the most relevant components labeled. The typical background pressures in a growth chamber of an MBE system range in the 10^{-10} to 10^{-11} Torr. These pressures are achieved by cryogenic pumps and ion pumps (not shown) that can be isolated from the growth chamber with gate valves for maintenance on either the chamber or the pumps. The chamber also contains a liquid nitrogen-filled cryo-shroud that surrounds the continuous-azimuthal-rotation (CAR) assembly where the substrate holder is located. Residual contaminants adsorb to the cryo-shroud, which can thought of as another cryogenic pump, further reducing the local background pressure near the substrate holder. In this ultra high vacuum environment, the flux of atoms or molecules emanating from the source effusion cells towards the substrate can either adsorb on the surface of the material and bond into the growing crystal or desorb back into the chamber, where they will be captured by the vacuum pumps. The low background pressure means that the mean free path of the adatoms is in the meter range and the flux from sources can be considered atomic or molecular “beams” depending on the source type. The source material in the effusion cells is typically of very high purity and the flux originates either through evaporation or sublimation. Mechanical shutters covering the source cell pocket are used to block the molecular beams when the particular source is not needed during the growth process. The interruption of the beam is sufficiently quick as to create atomically abrupt interfaces since the time required to actuate the shutters is on the order of the formation of a monolayer of the crystalline material due to the slow growth rate. The fluxes from individual source cells can be tuned by changing the source temperature and measuring the corresponding beam equivalent pressure (BEP) using a tungsten filament ion gauge located on the back of the substrate manipulator. This BEP gauge can be positioned in

approximately the same place as the substrate is during growth to accurately gauge the molecular beams incident on the substrate. By combining the tuned beams from multiple sources, alloy materials can be grown with high compositional precision. In addition, the substrate rotation from the CAR assembly insures uniform coverage of the substrate by all of the sources. The repeatability of the substrate positioning and temperature is critical since growth calibrations are done before the growth of the material and can not be checked during grown. As such positioning of the sample on the CAR and on the sample holder must be done using a repeatable and accurate method in order to compare the different samples to each other. Figure 2.2 shows a standard Veeco mounting technique where the samples is held together in place by two spring plates.

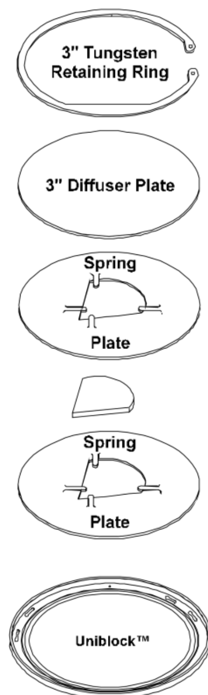

Figure 2.2: Sample mounting technique recommended by Veeco. It uses two spring plates to suspend the substrate material with minimal contact. The retainer ring holds the sample and spring plates firmly in place in a repeatable way. (reproduced from Veeco Instruments, Inc.)

2.2 Flux Measurements and Growth Calibrations

During growth of III-V materials, the group-V elements (P, As, Sb, Bi) are supplied in excess since they have relatively high vapor pressures when compared to the group-III elements (Al, Ga, In). This imbalance of supplied flux from the various sources results in near unity sticking coefficients for the group-III elements. The excess group-V material desorbs back into the chamber, therefore the limiting factor in the rate of growth of the crystal is set by the group III fluxes. The resulting surface of the stoichiometric crystal is group-V passivated due to the excess of group V atoms, an important quality which will be discussed further in the RHEED section. The growth rate of the crystal can be estimated to first order from Equation 2.1 [75], which relates the measured BEP from the ion gauge, the atomic mass of the molecule/atom M^*, and the temperature of the cell T, to the incident *Flux* on the substrate,

$$Flux \propto \frac{BEP}{\sqrt{2\pi M^* kT}}. \tag{2.1}$$

For alloy materials such as InGaAs where there are two distinct group IIIs, careful calibrations were performed to maintain an accurate ratio of the BEPs of In to Ga in order maintain a lattice-matching condition to the InP substrate. All ratios of V/III, V/RE, and III(A)/III(B) mentioned in this dissertation are in terms of measured BEP rather than *Flux*. It will be shown in the following derivation that the difference between *Flux* ratios and BEP ratios can be accounted for in a calibration factor. First order approximations of the alloy composition can also be done by using the equation

$$\%III_A = \frac{Flux_A}{Flux_A + Flux_B} = \frac{\dfrac{BEP_A}{\sqrt{M_A^* T_A}}}{\dfrac{BEP_A}{\sqrt{M_A^* T_A}} + \dfrac{BEP_B}{\sqrt{M_B^* T_B}}}, \tag{2.2}$$

where $\%III_A$ is the percentage of incorporated group-III of species A in the A B group-V (ABV) alloy, M^* and T are the mass and temperature of the corresponding group III species. However, Equation 2.2 is an approximation and calibration measurements from X-ray diffraction (XRD), discussed later in this chapter, can provide more direct information about the material composition. In order to reconcile the approximation with direct measurements, a calibrating factor was utilized that takes into account the geometry of the chamber, possible differences in the shape of the crucibles, potential non-unity sticking coefficients, and even the mass and temperature differences of the two sources. Thus Equation 2.2 can be rewritten as,

$$\%III_A = \frac{\beta\, BEP_A \frac{\sqrt{M_B^* T_B}}{\sqrt{M_A^* T_A}}}{\beta\, BEP_A \frac{\sqrt{M_B^* T_B}}{\sqrt{M_A^* T_A}} + BEP_B} = \frac{\alpha\, BEP_A}{\alpha\, BEP_A + BEP_B}, \tag{2.3}$$

where $\%III_A$ is now the measured incorporated percentage in the alloy from XRD, β is the calibrating factor, and α is calibrating factor taking into account the mass and temperature differences as well. This α factor can vary for different targeted alloy compositions of the same species and must be checked every time something changes in the MBE chamber. Growth rates can also calibrated by using the following ratio equation

$$\frac{GR_{AV}}{GR_{ABV}} = \frac{\%A}{\%A + \%B} = \frac{\%A}{1} = \%A, \tag{2.4}$$

where GR is the growth rate of the respective alloy species. Therefore if the growth rate of an binary III-V material, like GaAs, is known then we can find the growth rate of a ternary III-V alloy of the form $A_xB_{1-x}V$, like InGaAs, provided we know the percentage of the A species, Ga, in the ABV alloy and that this alloy also uses the same BEP of A for AV as it does for the ABV alloy. Thus the equation becomes

$$GR_{ABV} = \frac{GR_{AV}}{\%A}. \tag{2.5}$$

2.3 Reflection High Energy Electron Diffraction

The most common *in situ* characterization technique utilized during MBE growth is reflection high energy electron diffraction (RHEED). RHEED is very sensitive to surface effects due to the low penetration depth of the electron beam. Because of the high scattering rate of electrons with air molecules, this technique requires UHV and must be done in the growth chamber. Since it is also non-destructive, it can be used during the growth process which allows for information to be gathered from the sample as it forms. The beam of electrons is incident on the sample at a grazing angle of 1-3° with energies around 10-30 KeV. The diffracted beam pattern impinges on a phosphor screen that exhibits photoluminescence when struck by the electrons. A CCD camera can be used to image the phosphor screen from the out-of-vacuum side and relay the images to the computer screen for analysis by the operator.

As discussed earlier, the group-V passivated surface creates bonding patterns and surface reconstructions during growth that affect the diffracted beam pattern. Different surface reconstructions along [110] and [-110] directions can indicate what growth space the material is in, which depends on substrate temperature and group-V overpressure. In addition, RHEED can give qualitative information about the surface morphology of the crystalline growth front [76-79]. Streaky patterns indicate smooth and flat surfaces while spotty patterns indicate surface roughening or 3 dimensional growth. On the other hand, very rough or amorphous surfaces show a hazy or ring-like pattern. Growth rate calibrations can also be performed using the intensity profile of the electron diffracted beam pattern [80-84]. When the substrate is not rotating, the intensity of the pattern is

proportional to the smoothness of the surface. As the adatoms adsorb to the surface and a new monolayer surface begins to coalesce, the intensity dims slightly due to the roughness from random atomic steps. As the new monolayer fully coalesces, the surface has less random atomic steps and appears smooth again, increasing the intensity of the diffracted pattern once again. The oscillatory period can be plotted as a function of time to extract the growth rate. RHEED intensity oscillations were used to provide initial rough calibrations of the growth rate of RE-As materials, which were later fine-tuned using other techniques such as x-ray diffraction of full RE-As films.

Another important use of RHEED applied in the work presented in this dissertation was to identify the transition from an oxide-coated substrate surface to a nearly oxide-free surface. Since neither of the MBE systems utilized for this work have phosphorus sources, deoxidation of the InP substrates was carried out under an As_2 overpressure. The potential problem with this method is that if epitaxial growth is not initiated swiftly following the completion of substrate deoxidation, a layer of InAs forms on the substrate surface. The lattice parameter of InAs is about 6.06 Å compared to 5.87 Å for InP, so it does not take much InAs before the film relaxes and impairs further growth. The deox procedure began by first dosing the surface with a constant As_2 overpressure. The substrate temperature was then raised until approximately 545 °C, as measured by pyrometry or bandedge thermometry, at which point the RHEED pattern evolves from a hazy 2x1 pattern to a sharp 2x4 reconstruction. The appearance of the 4x RHEED reconstruction indicates that the substrate has desorbed most of the oxide and the surface is now As terminated. Due to the high desorption rate of the P from the substrate, growth of the lattice matched crystal must begin almost immediately to prevent excessive As for P substitution and hence the formation of InAs. Once the 4x pattern is barely visible, the substrate temperature is quickly lowered to a growth temperature of 490 °C

and growth of InGaAs begins. The deox process takes approximately 2-3 minutes to raise the temperature from 490 °C to 545 °C, where the 4x patterns begins to appear, and back to 490 °C for the initiation of the InGaAs growth.

2.4 High Resolution X-ray Diffraction

High resolution x-ray diffraction (HR-XRD) is one of the most powerful non-destructive characterization techniques used for epitaxial film analysis. Diffracted patterns from x-rays give direct information about the spacing between atomic layers in the sample, and can be used to obtain information about strain, layer thickness, superlattice periodicity, alloy composition, relaxation, etc. A more complete introduction into HR-XRD can be found in Moram *et al.* [85]. One of the most common scans used to characterize materials is the symmetric ω-2θ scans around the diffraction peak of the (004) planes, shown in Figure 2.3. The Q vector resulting from the incident beam and the refracted beam is used to probe the atomic layers in the growth direction. Depending on the incident beam angle, ω, and the diffracted beam angle, 2θ, the diffraction pattern can constructively and destructively interfere based on the Bragg law. These scans were extensively performed on the materials grown for this dissertation to obtain lattice matching conditions and growth rate calibrations, and assess the quality of the superlattice period interfaces.

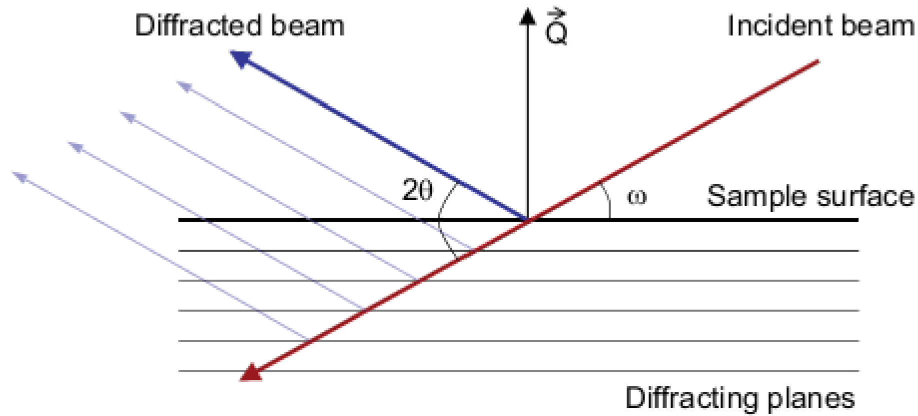

Figure 2.3: Diagram of a typical symmetric *ω-2θ* scan showing the resulting Q vector probing the atomic layers in the growth direction (reprinted from [86]).

Successive scans where the resulting Q vector is not parallel to the growth direction (004) can be done for other reciprocal space points, for example the (224) or (115) lattice planes. The resulting scans can be plotted together as a two-dimensional reciprocal space map (RSM). RSMs can provide additional information regarding in-plane strain, layer relaxation, phase segregation, and dislocation density. Figure 2.4 shows example RSM scans for superlattices of RE-As in an InGaAs matrix. The LaAs superlattice in Figure 2.4(a) shows some relaxation while the LuAs superlattice in 2.4(b) appears coherently strained.

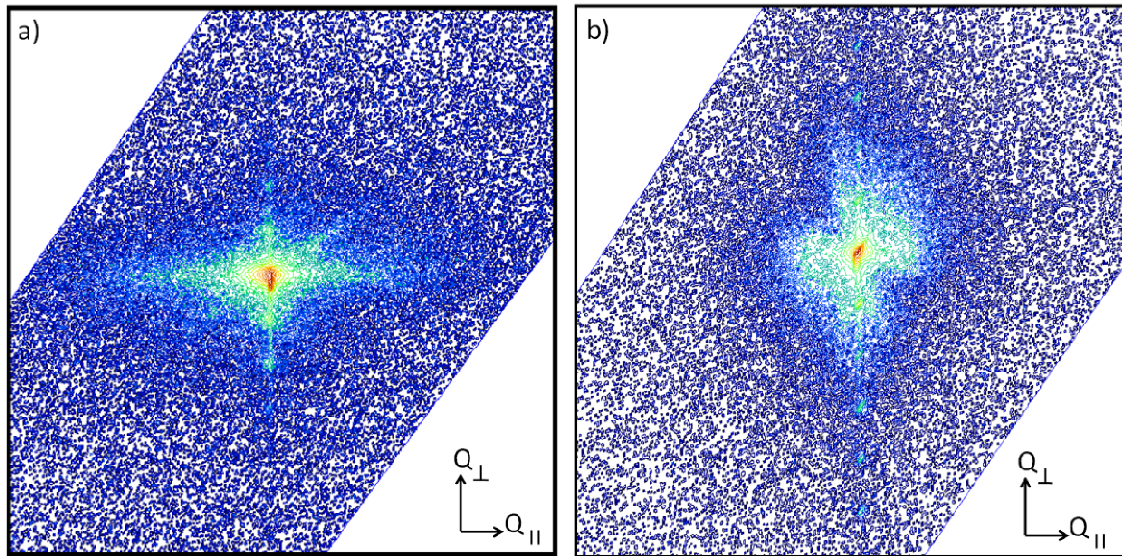

Figure 2.4: Reciprocal space map around the (224) diffraction peak of InP for a 30 period superlattice of (a) 0.2 ML LaAs:InGaAs and (b) 1.2 ML LuAs:InGaAs. The elongation in the Q parallel direction in (a) is indicative of a mosaic spread for the in-plain lattice parameter.

2.5 Atomic Force Microscopy

The surface roughness of material surfaces can be characterized via atomic force microscopy (AFM). A Veeco Dimension ICON atomic force microscope was used for the work in this dissertation to obtain the surface topography of the nanocomposites at room temperature and in ambient atmosphere. The silicon probe tip utilized by the microscopy for these scans had an average spring constant of 42 N/m, a resonant frequency of 320 KHz, and tip radius of 8 nm. The AFM scans were used in the assessment of the overall quality of the superlattice structures. Since overgrowth of the RE-As nanoparticles by the matrix material occurs for every superlattice period, any roughness that occurs at the interfaces that does not smooth out in the overgrowth compounds with the roughness of the subsequent period interface. Hence the RMS

roughness of the top layer is a cumulative gauge of the smoothness of all the period interfaces. As such AFM measurements along with XRD scans give a fairly good non-destructive measure of the overall material quality of the nanocomposites.

2.6 Hall Measurements

Hall measurements performed on the materials in this work to extract their electrical properties used the van der Pauw configuration [87-90] to simplify sample preparation and minimize error due to sample shape irregularities. Figure 2.5 shows the electrical connections made to a sample: the left two diagrams are used to measure the R_A and R_B required for the electrical resistivity and the right diagram shows the connection required to measure the Hall voltage. The resistivity can be extracted from the van der Pauw equation [88]

$$\exp\left(\frac{-\pi d}{\rho} R_A\right) + \exp\left(\frac{-\pi d}{\rho} R_B\right) = 1 , \tag{2.6}$$

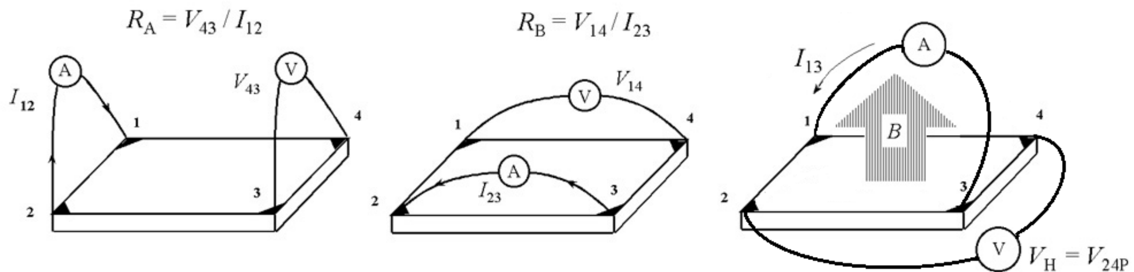

Figure 2.5: Electrical connection to samples for Hall measurements in the van der Pauw configuration. In order to minimize error caused by non-point source contacts, ohmic contacts to the samples must be at the corners of the sample and triangular in shape [90].

where R_A and R_B are the resistances found using the configuration from Figure 2.5, d is the thickness of the test structure being measured, and ρ is the resistivity of the sample. The equation can then be simplified to

$$\rho = \frac{\pi d}{\ln 2}\left(\frac{R_A + R_B}{2}\right) f\left(\frac{R_A}{R_B}\right), \tag{2.7}$$

where $f(x)$ satisfies the equation

$$\exp\left(\frac{-\ln 2}{f(x)}\right)\cosh\left(\left(\frac{x-1}{x+1}\right)\frac{\ln 2}{f(x)}\right) = \frac{1}{2}. \tag{2.8}$$

However, $f(x)$ does not have a closed form solution or analytic expression and must be solved numerically for each value of x. For small values of x, an approximate expression of $f(x)$ is

$$f(x) \approx \frac{1}{\cosh\left(\frac{\ln x}{2.403}\right)}, \tag{2.9}$$

with an error of less than 0.1% for $x < 2.2$ and less than 1% for $x < 4.3$. The charge carrier concentration can be extracted from the equation

$$n = \frac{I B}{q V_H d}, \tag{2.10}$$

where I is the current shown in rightmost diagram in Figure 2.5, V_H is the hall voltage, q is the electric charge, and d is the thickness of the test structure. The mobility can then be calculated from the measured resistivity and carrier concentration using the equation

$$\mu = \frac{1}{q n \rho}. \tag{2.11}$$

Temperature-dependent Hall measurements, also in the van der Pauw configuration, were used to estimate the activation energy of the charges. A brief explanation of the theory follows. A more in-depth tutorial of the following derivation can be found in Sze [91]. For a given semiconductor material, the number of electrons is

given by the total number of states *N(E)*, multiplied by the probability of occupancy *F(E)*, and then integrated over the conduction band.

$$n = \int_{Ec}^{\infty} N(E)F(E)dE\,, \tag{2.12}$$

The density of states (DOS) can be approximated by the density near the bottom of the conduction band as

$$N(E) = M_c \frac{\sqrt{2}}{\pi^2} \frac{m_{de}^{3/2}(E - E_c)^{1/2}}{\hbar^3}\,, \tag{2.13}$$

where M_c is the number of equivalent minima in the conduction band and m_{de} is the DOS mass for the electrons given by

$$m_{de} = (m_1^* m_2^* m_3^*)^{1/3}\,, \tag{2.14}$$

where m_1^*, m_2^*, and m_3^* are the effective masses along the principal axes of the energy isosurface. The probability of occupancy is strongly dependent on the temperature and is given by the Fermi-Dirac distribution

$$F(E) = \frac{1}{1 + \exp\left(\dfrac{E - E_F}{kT}\right)}\,, \tag{2.15}$$

where E_F is the Fermi energy level. The carrier concentration from Equation 2.12 can be evaluated to be

$$n = \frac{4M_c}{\sqrt{\pi}} \left(\frac{2\pi m_{de} kT}{h^2}\right)^{3/2} F_{1/2}\left(\frac{E_F - E_C}{kT}\right), \tag{2.16}$$

where $F_{1/2}(x)$ is the Fermi-Dirac integral which approximates $\sqrt{\pi}\exp(x)/2$, such that the equation simplifies to

$$n = N_c \exp\left(\frac{E_F - E_C}{kT}\right), \tag{2.17}$$

where N_c is the effective density of states in the conduction band and is defined as

$$N_c = 2M_c \left(\frac{2\pi m_{de} kT}{h^2}\right)^{3/2}. \tag{2.18}$$

Equation 2.17 can be rewritten as

$$n = N_c \exp\left(-\frac{E_C - E_F}{kT}\right) = N_c \exp\left(-\frac{E_a}{kT}\right), \tag{2.19}$$

where E_a is the energy difference between the Fermi level and the conduction band or activation energy. However, it is important to note that the approximation of the Fermi-Dirac integral used to derive Equation 2.17 is accurate for activation energies whose magnitude is greater than 25 meV below the conduction band [91]. Below the 25 meV, the Fermi-Dirac integral approximation begins to overestimate the value of the integral. By linearly extrapolating the carrier concentration data from the temperature-dependent Hall measurements in a log plot, the value for the activation energy for the charges in the material can be extracted using the following equation for two points on that line

$$E_a = \frac{\ln n_1 - \ln n_2}{q/kT_1 - q/kT_2}. \tag{2.20}$$

2.7 Carrier Lifetime Measurements

Time-resolved pump-probe optical measurements were used to characterize the carrier dynamics of the materials and how the lifetimes of photogenerated carriers were affected by the introduction of trap states caused by the RE-As nanoparticles. A high intensity ultrashort laser pulse was used for the initial excitation of the carriers in the material. A lower intensity probe pulse of equal time duration was then used to sample the transmission through the affected area by varying the relative arrival times of the two pulses on the material. Optical carrier generation in a semiconductor material induces several changes in the properties of the material that can cause band energy dependent shifts in the observed absorption edge.

2.7.1 Absorption Shifts

There are three main processes that can affect the absorption band edge of a semiconductor using a pump-probe measurement with photon energies slightly above the bandgap: Burstein-Moss shift (band filling), bandgap renormalization, and free carrier absorption [41]. A more detailed examination of each of these processes can be found in Schubert [92].

The Burstein-Moss shift is a blue shift in the absorption band edge related to band-filling effects from high doping levels, but is relevant under these optically induced conditions. When the incident pump signal is absorbed, available conduction band states become significantly filled due to the finite density of states near the band edge. Absorption transitions from the top of the valence band to the bottom of the conduction band can therefore no longer occur. This results in an apparent increase in energy of the absorption edge and an increase in the material transparency at photon energies near the band gap energy. The Burstein-Moss shift is given by the equation [92]

$$E_F - E_C = \frac{\hbar^2}{2m_e^*}(3\pi^2 n)^{2/3}, \tag{2.21}$$

where m_e* is the effective electron mass and n is the carrier concentration assuming that the material is degenerately doped n-type. The equation can also be used to the find the shift in p-type materials, so it is important to note that the shift is inversely proportional to the carrier mass. This means that the effect will more pronounced for electron than for holes.

Bandgap renormalization is red shift in the absorption band edge caused by the lowering of the carrier energies due to many-body effects of the free carriers. These many-body effects become important during small interaction distances and high free carrier concentrations. If we assume that electrons are uniformly distributed across a

crystal, the attractive and repulsive forces between electrons with the same spin and opposite spin tend to have same spin electrons stay away from each other and vice versa. This interaction along with the long-range coulombic interactions leads to a net attractive force that reduces the overall energy of the system and lowers the conduction band edge. Spin interactions between holes behave in a similar fashion leading to net lowering of the system energy and the increase of the valence band edge. The magnitude of the bandgap renormalization is given by the Thomas-Fermi equation [92]

$$\Delta E_g = -\frac{e^3 \sqrt{m_e^*} (3n)^{1/6}}{4\pi^{5/3} \varepsilon^{3/2} \hbar}, \tag{2.22}$$

for degenerate materials. It is important to note that this equation does not consider the carrier-impurity interactions that can increase the strength of the effect to $\Delta E_g \propto n^{1/3}$, since the excitation of charges is due to optical absorption of laser pulses and not due to dopants.

Free carrier absorption can play a significant effect in semiconductors with very high carrier densities, and occurs when an incident photon is absorbed by a charge carrier from an already excited state to a higher excited state in the band. These interactions, however, require carrier densities greater than 10^{20} cm^{-3} in order to be significant and are not expected to have influence on the pump-probe measurements because the concentration of the injected carriers from the excitation of the pump pulse is on the order of 10^{18} cm^{-3}.

The Burstein-Moss shift and the bandgap renormalizations effects shift the band edges in opposite directions. However, it is clear that the Burstein-Moss shift would be the strongest effect based on the inverse effective mass of the carrier and $n^{2/3}$ proportionality compared the square root of the effective mass and the $n^{1/6}$ proportionality for the bandgap renormalization. This observation is supported by optical transmission

measurements of highly doped $In_{0.53}Ga_{0.47}As$ layers lattice matched to InP, where the absorption band edge for the p-type material (p ~4×10^{18} cm^{-3}), did not change compared to an undoped bulk layer. On the other hand, in n-type material, with doping levels of 4×10^{18} cm^{-3} and 7×10^{18} cm^{-3}, the band edges blue-shifted significantly with the higher n-type material being almost completely transparent to 1550 nm excitation [93]. For all the materials measured in this investigation, excitation by the pump pulse produces an increase in the transmission of the subsequent probe pulse, indicating that the Burstein-Moss shift mechanism dominates the changes in transmission of the material.

2.7.2 Carrier Capture and Recombination

There are several possible mechanisms by which the carriers can recombine following the excitation by the pump pulse. One of the primary mechanisms is radiative band-to-band recombination by the electrons and holes, which have time constants on the order of nanoseconds. When deep states are introduced in the bandgap of the material, however, the recombination processes becomes more complex. A more detailed explanation of these processes can be found in Muller [94]. The equations describing the generation and recombination through localized deep trap states in the band gap was first introduced by Hall and by Shockley and Read [95,96]; the processes are referred to as Shockley-Read-Hall (SRH) recombination.

The capture of carriers by a trap state can be described in terms of the capture cross section σ. Any carriers traversing through an area within the size of the capture cross section of the trap will be captured. Assuming a carrier concentration n, the average time per volume it takes to capture a carrier is given by

$$\tau = \frac{1}{(1-F(E_t))N_t v_{th}\sigma n}, \qquad (2.23)$$

where v_{th} is the thermal velocity of the carrier and the $(1-F(E_t))\ N_t$ term is the number of unoccupied trap states located at an energy E_t within the bandgap. It is clear from the equation that in order to decrease the capture time, a large number of trap states at or near the intrinsic level are required. It is important to note that trap states close to either the conduction or valence band will have carrier lifetimes that are dominated by the minority carrier rather than the majority carrier of the semiconductor. The reason for this is that trap states will be occupied (unoccupied) if the majority carriers are electrons (holes) since there are so many of them, but then have to wait for the arrival of the minority carrier holes (electrons) to recombine with the trapped charge. In the event that the material has no clear majority carrier, the capture rate of the charges is the same for electrons and holes such that $\tau_n \approx \tau_h \equiv \tau_{capture}$. The lifetime of any excess carriers is then given by

$$\tau = \tau_{capture}\left[1+\cosh\left(\frac{E_t - E_F}{kT}\right)\right], \tag{2.24}$$

where E_t is the energy of the trap state and E_F is the Fermi level of the intrinsic semiconductor. The carrier lifetime is minimized when the energy of the trap is the same as the Fermi level and $\tau = 2\tau_{capture}$.

2.7.3 Pump-Probe Transmission Setup

Electron-hole recombination lifetime measurements were performed by time-resolved pump-probe transmission near the band edge of $In_{0.53}Ga_{0.47}As$. This technique, outlined in Figure 2.6, utilizes the band-filling effect from the excitation of electron-hole pairs by ultrashort pump pulses of a mode-locked laser. Ultrashort pulses with intensity a hundred times less than the pump pulse were then used to sample the transparency of the material. As the charges causing the band-filling effect begin to recombine, the probe

pulse transmits through the material less and less since there are now more charges and states available for absorption of the probe pulse. The normalized intensity of the transmitted probe pulse can plotted as a function of the delay t between arrival of the pump and probe pulses. The plot follows the equation

$$\frac{I}{I_0} = \exp(-t/\tau), \tag{2.25}$$

where τ is the carrier lifetime. Figure 2.7 shows a typical transmitted intensity measurement that has been normalized for ease of computation and plotted on a log scale. The calculated slope of the linear fit uses a line with end points at the 90% and 10% of normalized intensity to extract the effective carrier lifetime, following previous measurements made by Driscoll [41] and Hanson [70]. The effective carrier lifetime then becomes

$$\tau = -\frac{t_{0.9} - t_{0.1}}{\ln(I_{0.9}) - \ln(I_{0.1})}, \tag{2.26}$$

where $t_{0.9}$ and $t_{0.1}$ correspond to the times at which the normalized intensities are 90% and 10% and $I_{0.9}$ and $I_{0.1}$ are simply 0.9 and 0.1 since they are normalized values.

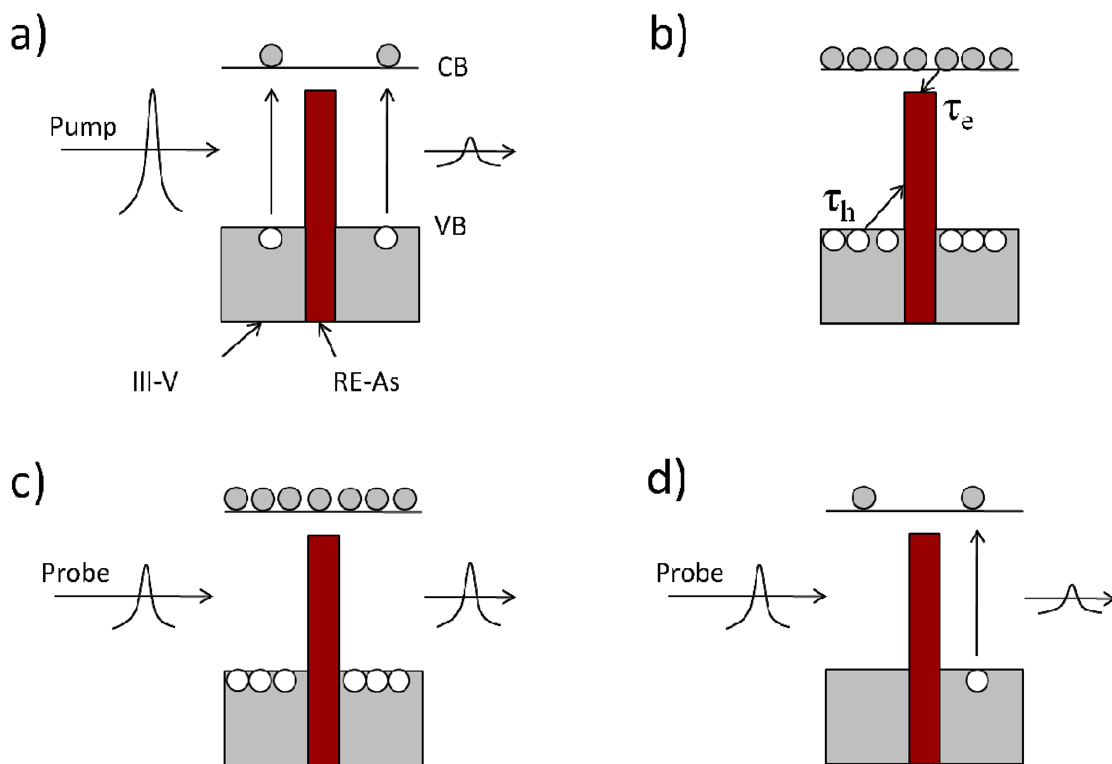

Figure 2.6: Illustration of a pump-probe transmission measurement. (a) The pump pulse is absorbed in the semiconductor, exciting electron-holes pairs. (b) Charges begin to recombine in the RE-As nanoparticles, which are fast recombination centers. (c) A large portion of the probe pulse is transmitted through the material when excited states near the band edges are filled due to optical excitation from the pump. (d) Subsequent measurements by probe pulses arriving increasingly after the pump pulse show decreased transmission as the charges begin to recombine and are thus available to absorb photons from the probe pulse.

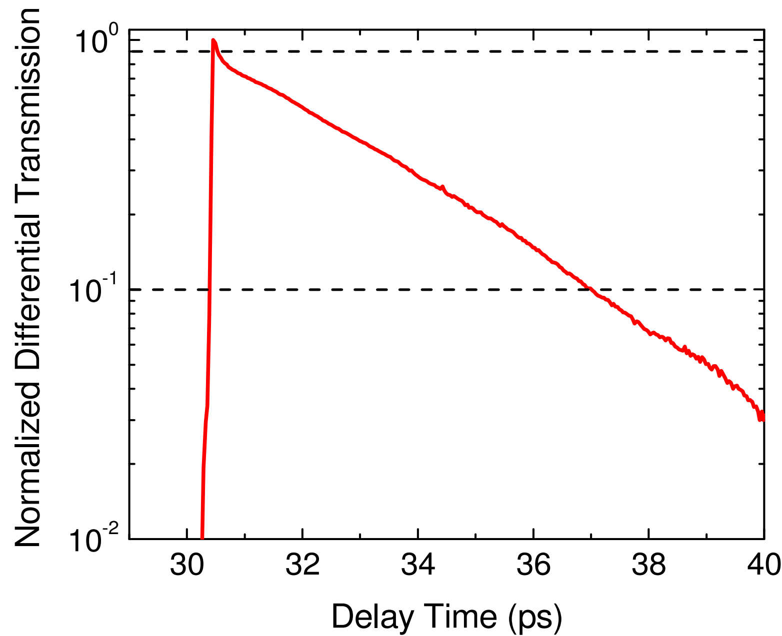

Figure 2.7: Normalized differential transmission of a 1.2 ML LuAs:InGaAs superlattice showing a carrier lifetime of 3.6 ps. The horizontal dashed lines indicate the 90% and 10% transmission used as the end points for the linear fitting.

The laser source for the carrier lifetime tests bench was a mode-locked laser centered at 1550 nm and pulsed at a repetition rate of 20 MHz with a full width at half maximum pulse width of 90 fs. The average output power of the laser was variable between 5 mW to 20 mW. The laser pulses were split using a broadband polarizing beamsplitter cube into s and p polarizations. A half waveplate used to rotate the polarization of the laser light before the beam splitter cube allowed the proportion of light output into the orthogonal polarization modes to be adjusted. The resulting output beams from the beamsplitter cube, the pump and probe pulses, were tuned so that the ratio of pump to probe was 100 to 1. The optical path of the probe signal includes a motorized stage with a maximum travel of 2.54 cm, corresponding to a range of 84 ps in the arrival time of the probe pulse at the sample relative to the pump pulse. The precision of the

stage allows the probe beam's arrival time to be controlled in increments as fine as 7 fs. The pump signal was chopped at a frequency of 1 KHz to minimize 1/f noise in the signal. Both pump and probe pulses were focused to the same spot on the sample using a large 3-inch diameter focusing lens. The measured spot size of the focused beam was approximately 100 µm in diameter. A linear polarizer with an extinction ratio of $1x10^6$ placed in after the sample removed any residual polarization leakage of the pump pulse into the probe. A beam dump behind the sample in the path of the pump beam minimized possible reflections back into the optical station. An iris placed before the detector also acted to minimize noise into the detector from reflections or other sources. The transmitted probe signal was detected by an amplified InGaAs photodetector connected to a lock-in amplifier. With the exception of the large 3-inch focusing lens made out of nBK7, all other lenses were made from CaF_2 to minimize dispersion of the femtosecond pulses. All mirrors were uncoated bare gold, also to minimize dispersion from the reflecting surfaces. A general schematic of the pump-probe optical setup is shown in Figure 2.8.

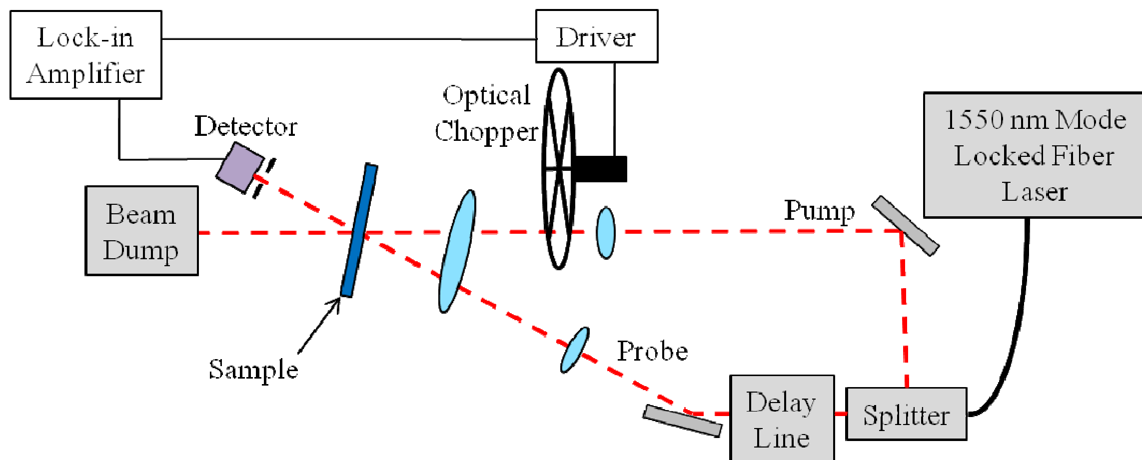

Figure 2.8: General overview of optical station used for time-resolved pump-probe transmission measurements

Chapter 3: Superlattices of RE-As:InGaAs

3.1 Rare-Earth Arsenides on InGaAs

Many rare-earth monopnictide compounds (RE-V) form rocksalt semimetals and can be epitaxially integrated as nanostructures and films when grown on zincblende III-V semiconductors [47]. The most-studied of these rare-earth arsenides (RE-As) is ErAs, which has a high density of states due to its semimetallic nature but tends to align the Fermi level close to the conduction band when grown on $In_{0.53}Ga_{0.47}As$ [41]. As a result, ErAs nanocomposite materials based on superlattice [72,73] and co-deposited [97] structures on InGaAs have been found to have prohibitively low dark resistivities for photomixer applications. The energetic structure of other rare-earth monopnictides is expected to differ only slightly across the lanthanide series due to the excitation of 4f electron states corresponding to transitions into completely screened final states [98-100]. As such, strain-related effects at the nanoparticle-matrix interface could potentially shift the Fermi level alignment closer to the midgap of the semiconductor and improve the properties of the photoconductive materials. However, aside from preliminary electrical studies of TbAs co-deposited in InGaAs that also showed prohibitively low dark resistivities [101], there has been little research exploring the effects of strain and lattice mismatch of other RE-As species in these epitaxial in InGaAs nanocomposite structures.

This chapter presents an investigation of the structural quality, electrical properties, and carrier dynamics of RE-As nanoparticles superlattice structures embedded in an $In_{0.53}Ga_{0.47}As$ matrix, grown lattice-matched to InP substrates, and assess their potential for photoconductive sources. The specific RE-As compounds studied are LaAs, ErAs, LuAs, and GdAs The investigation explored the effect of increasing amounts of

deposition of RE-As in the superlattice structures. As shown in Figure 3.1, the RE-As monopnictide series spans a wide range of lattice parameters. LaAs and LuAs represent the extrema in lattice parameter of the RE-As series, while GdAs is intermediate between these extremes and is nearly lattice-matched to InP [47]. Table 3.1 summarizes the lattice parameters and the percent lattice mismatch to InP for the RE species in this investigation.

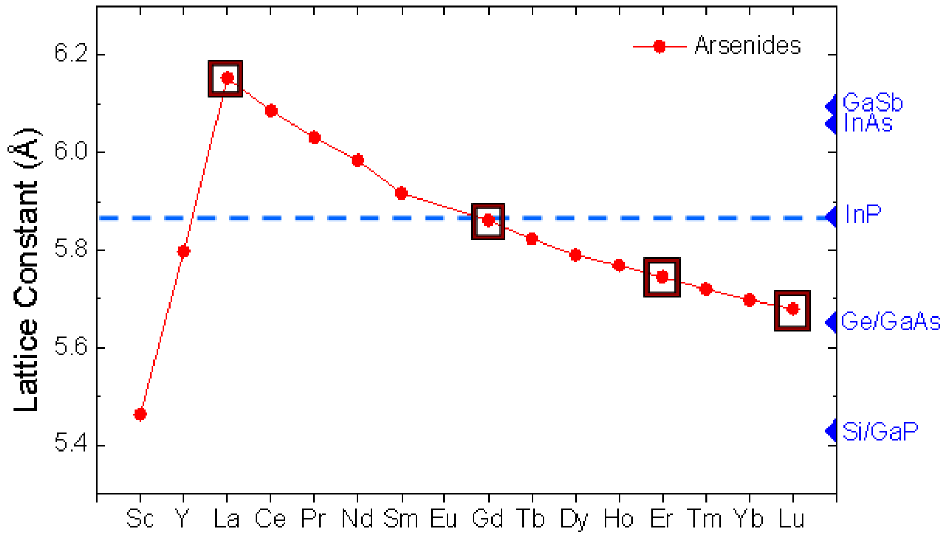

Figure 3.1: Rocksalt lattice parameters of rare-earth arsenide compounds over the range of the lanthanide series. The lattice parameters of several widely-used semiconductor substrates are given along the right edge of the figure. The rare-earth species in this investigation are highlighted by squares.

Table 3.1: RE-As species, lattice parameter and mismatch to InP.

RE-As Species	Lattice Parameter (Å)	Lattice Mismatch to InP
LuAs	5.68	3.3 %
ErAs	5.75	2.2 %
GdAs	5.86	0.1 %
LaAs	6.15	-4.6 %

3.2 Growth and Structure of RE-As Superlattices

RE-As superlattice samples were grown on Fe-doped semi-insulating (100)-oriented InP substrates. The InGaAs host matrix was grown using an As_2/group-III beam equivalent pressure (BEP) ratio of 15 and the As_2 flux was held constant throughout the growth. Preparation of the substrate for growth was initiated by increasing its temperature, as measured by optical pyrometry or bandedge thermometry, until the native surface oxide began to desorb at approximately 545 °C under an As_2 BEP of 1×10^{-5} Torr. Oxide desorption was monitored using reflection high energy electron diffraction (RHEED) as detailed in Section 2.3. The substrate temperature was then swiftly lowered to 490 °C to commence growth. The superlattice structures consisted of a 150 nm buffer layer of InGaAs used to smooth out the surface after deoxidation of the InP substrate, then a fixed deposition of RE-As was grown and followed by 40 nm of InGaAs overgrowth; the RE-As deposition and InGaAs overgrowth steps constituted a single period which was repeated thirty times. The period spacing was kept at 40 nm for all structures in this investigation for clarity of comparison since reducing the superlattice period can reduce the lifetime through a faster diffusive-limited capture process and affect the electrical properties through band bending effects of the InGaAs overgrowth within a period [56,102]. The superlattice structures are similar to those investigated by Driscoll et al. [72] and the ErAs-containing superlattices were reproduced in this study for the purpose of comparison. All materials grown are of this basic architecture except for those prepared for transmission electron microscopy (TEM) studies, which varied the amount of RE-As deposited per period within a single sample. Specifically, TEM structures began with depositions of 0.2 ML in the first period and increased by 0.2 ML per period up to 3.0 ML. Figure 3.2 schematically depicts the different types of structures grown for this investigation. The different RE-As depositions for the structures studied

are given in terms of equivalent number of monolayers (ML), as determined from RHEED intensity oscillations and X-ray diffraction (XRD) measurements of full RE-As films.

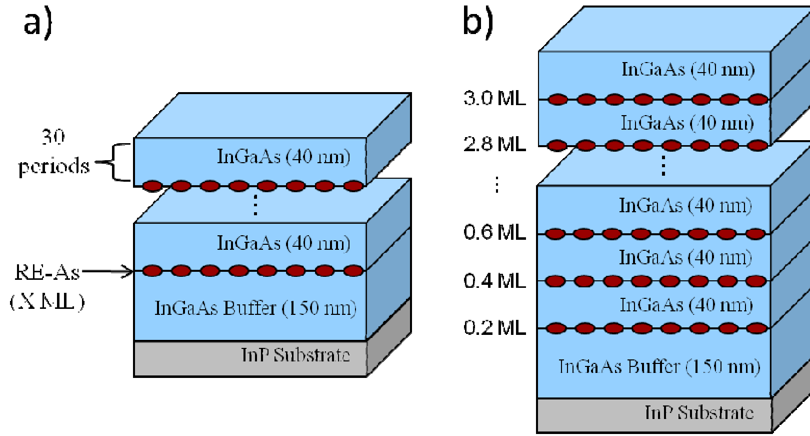

Figure 3.2: Superlattice structures grown as (a) photoconductive material with the same deposition of RE-As per period for 30 periods and (b) structures for TEM studies with increasing deposition of RE-As per period from 0.2 ML to 3.0 ML (15 periods).

Prior studies of ErAs [71] and LuAs [103] nanocomposites have yielded information about the embedded growth mode of the RE-As on zincblende materials. The RE atoms displace the group-III atoms in the matrix and nucleate into nanoparticles with thicknesses of three to four monolayers in height before expanding laterally [48,49]. As such, varying the amount of RE-As deposited affects both the size and surface density of the nanoparticles [59,71,103], making the average height of the nanoparticles larger than the equivalent monolayer depositions. For nanocomposites containing LuAs, ErAs, and GdAs, superlattices with effective RE-As depositions of 1.2 ML or less exhibited streaky RHEED patterns with only a slight blurring during the first 10 nm of InGaAs overgrowth. The streaky pattern recovered for each period throughout the superlattice. Figure 3.3a shows the streaky RHEED pattern for the InGaAs overgrowth after 30 periods of 1.2 ML

of LuAs. For 1.6 ML of RE-As depositions, the observed RHEED pattern began to chevron at the initiation of the InGaAs overgrowth, indicating increased surface roughness. The RHEED pattern recovered, showing a somewhat streaky pattern after ~28 nm of InGaAs deposition during the first superlattice periods. However, the recovery of the InGaAs became progressively worse as the number of periods increased. Figure 3.3b shows the RHEED pattern after 30 periods of 1.6 ML of LuAs. Because the underlying III-V material exposed between nanoparticles seeds the overgrowth of the subsequent InGaAs layers [59,71,103], deterioration of the surface is attributed to a reduction in the uncovered area of the underlying III-V layer as higher density and/or larger particles are formed with increased RE-As deposition. On the other hand, the RHEED pattern for the LaAs-containing superlattices began to chevron immediately during the LaAs deposition. The pattern of the overgrowth became spotty and never fully recovered for LaAs depositions greater than ~0.2 ML. Figure 3.3c shows RHEED pattern after 30 periods of 0.3 ML of LaAs. The patterns look very similar after 30 periods for the 1.6 ML of LuAs and the 0.3 ML LaAs suggesting a similar degradation in quality of the InGaAs overgrowth for both.

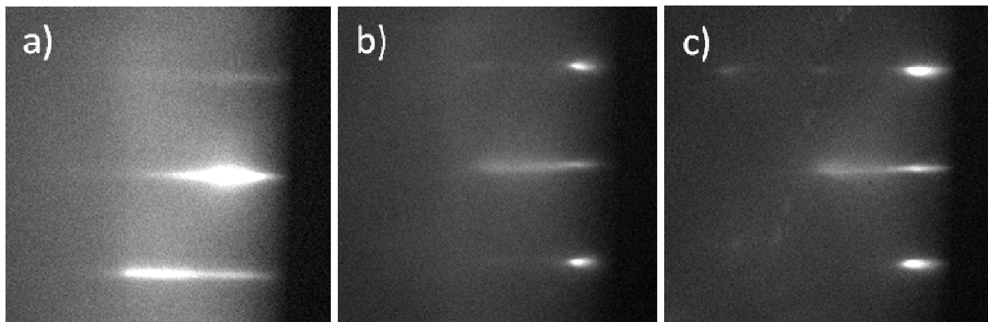

Figure 3.3: RHEED patterns of InGaAs overgrowth after 30 superlattice periods for a) 1.2 ML of LuAs, b) 1.6 ML of LuAs, and c) 0.3 ML of LaAs. The diffraction pattern for the LaAs superlattice after 30 periods degraded for a much lower deposition than other RE-As and appears qualitatively similar to that of the LuAs at 1.6 ML depositions.

Symmetric ω-2θ XRD scans around the (004) diffraction peak of the InP substrate showed well-defined superlattice peaks that degraded significantly for depositions of 1.6 ML for LuAs and GdAs and 0.2 ML for LaAs. In addition, as shown in Figure 3.4, the root-mean-squared surface roughness from atomic force microscopy (AFM) measurements increased dramatically for LuAs and GdAs at and above depositions of 1.6 ML and for LaAs at a deposition of 0.2 ML compared to lower depositions explored, in agreement with XRD and RHEED studies, as well as with previous studies of ErAs [71].

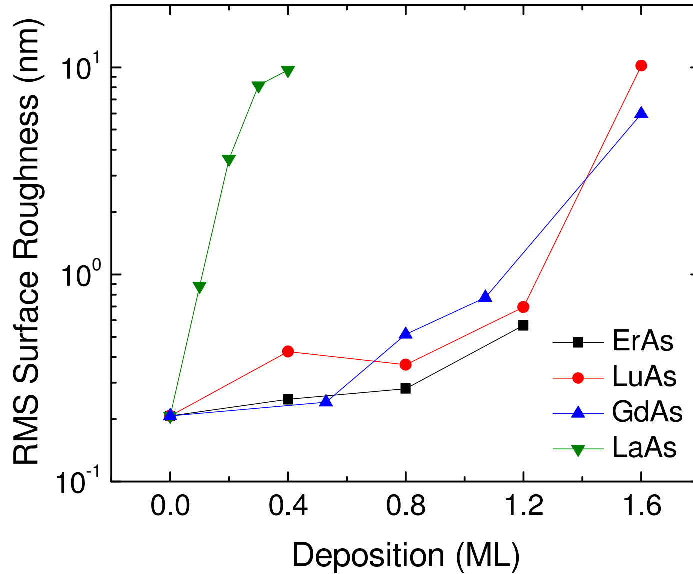

Figure 3.4: Root-mean-squared surface roughness AFM scans of superlattices with increasing RE-As deposition. Surface morphology of LaAs-containing superlattices degraded at a much lower deposition than other RE-As compounds investigated.

Cross-sectional TEM studies of LuAs structures grown with increasing deposition per period, shown in Figure 3.5a, indicated some surface modulation at the RE-As/InGaAs interfaces and lower quality overgrowth after a deposition of 1.6 ML, which

is consistent with previous studies of ErAs on InGaAs [41], as well as the RHEED analysis. By contrast, cross-sectional TEM studies of similar LaAs structures, shown in Figure 3.5b, showed significant planar defect formation in the InGaAs overgrowth for LaAs depositions as low as only 0.2 ML. These differences can be attributed to the single thermodynamically stable rocksalt crystalline phase of ErAs, LuAs, and GdAs, which forms a continuous As sub-lattice with the host matrix under typical zincblende III-V growth conditions [47,104]. However, LaAs can form multiple stable crystalline phases and orientations that can contribute to the difficulty in maintaining high-quality overgrowth and is consistent with XRD measurements of LaAs films [105]. No further depositions of RE-As beyond 1.6 ML for LuAs and GdAs and beyond 0.4 ML for LaAs were attempted as the overgrowth became progressively more challenging and the material quality degraded significantly.

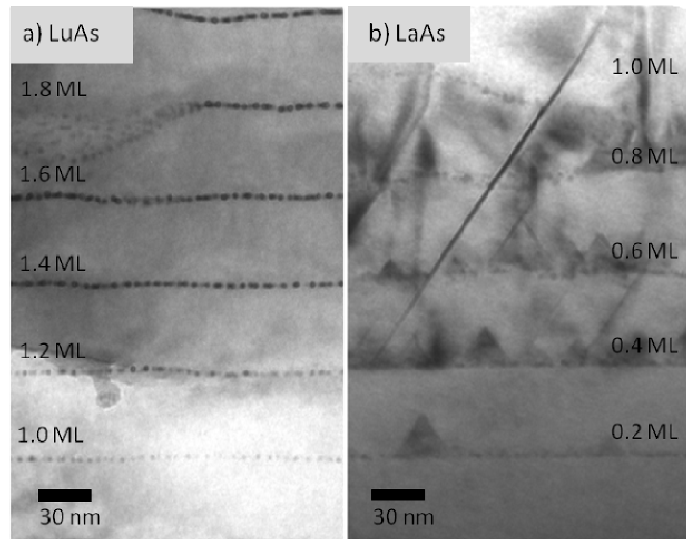

Figure 3.5: Cross-sectional TEM study of a) LuAs- and b) LaAs-containing structures with increasing deposition of RE-As per period. LuAs shows good material overgrowth up to 1.6 ML depositions. LaAs has poor quality overgrowth even at 0.2 ML depositions. The contrast variation across the LuAs sample was due to local re-deposition during ion-milling and sample preparation.

3.3 Electrical Properties of RE-As Superlattices

Room-temperature Hall measurements indicated electrons as the majority carriers for all of the superlattice structures. Low depositions of RE-As initially reduced the measured dark resistivity, relative to the InGaAs reference resistivity of 0.07 Ω-cm. As the RE-As deposition was increased, the dark resistivity gradually increased by about an order of magnitude for each of the RE-As-containing superlattices over the range of depositions studied, as shown in Figure 3.6. This is consistent with previous studies of superlattices of ErAs on InGaAs [72] where the ErAs nanoparticles appear to dope the InGaAs at low depositions and act as recombination centers at high depositions, reducing mobility and hence conductivity. A clear division was also observed between the LaAs structures and the other RE-As-containing compounds. The highest resistivity achieved by the LaAs:InGaAs structures was 0.18 Ω-cm for the 0.4 ML superlattice. However, the highest resistivities achieved by the LuAs:InGaAs and GdAs:InGaAs structures were only about 0.03 Ω-cm for the 1.6 ML superlattices. Some modest differences in resistivity were observed between the LuAs, ErAs, and GdAs-containing superlattice, suggesting some tunability of the electrical properties with the selection of RE species. The mobilities of all the superlattices are shown in Figure 3.7. The general trend is one of decreasing carrier mobility with increasing depositions of RE-As, which is attributed to the degradation of overgrowth quality. With increasing RE-As deposition, the fraction of the exposed InGaAs surface decreases making it more difficult to seed single phase overgrowth [59,71,103]. This likely results in crystalline defects that increase carrier scattering and reduce mobility. The mobility of the LaAs:InGaAs superlattices dropped rapidly with increasing LaAs deposition, reaching as low as 1600 cm^2/V-s for only 0.4 ML. By contrast, LuAs:InGaAs and GdAs:InGaAs nanocomposites maintained mobilities above 2400 cm^2/V-s for depositions as high as 1.6 ML and were uniformly ~20% and

~30% higher, respectively, than the ErAs:InGaAs. The differences in electrical properties between the LaAs:InGaAs and the other RE-As:InGaAs superlattices can be attributed to the quality of the InGaAs overgrowth, as the formation of multiple LaAs crystalline phases degrade InGaAs overgrowth and lead to a poorer quality material, as evidenced by the cross-sectional TEM studies in the previous section. This suggests that the path to improving the carrier mobility of these materials, which is critical for photomixers, is to improve the quality of the material overgrowth of the RE-As nanostructures and will be further explored in the following chapter.

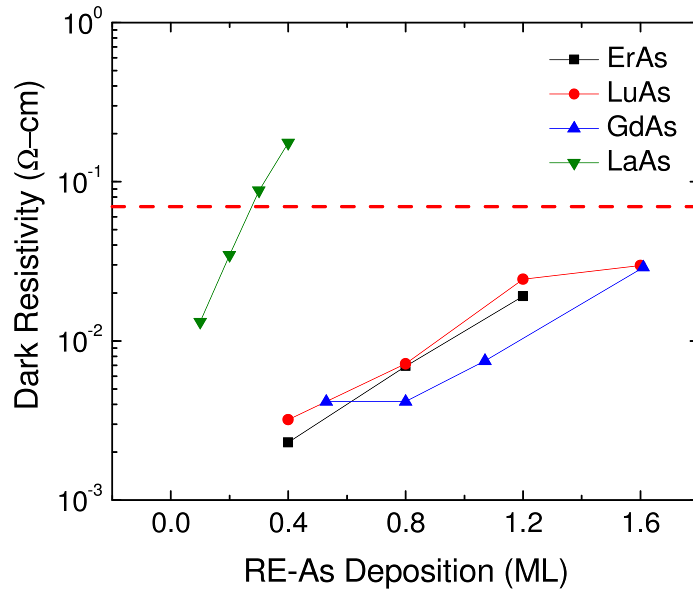

Figure 3.6: Room-temperature dark resistivity measurements of superlattices as a function of increasing RE-As deposition. Superlattices containing LaAs exhibited significantly higher resistivities than those containing ErAs, LuAs, and GdAs at all depositions. The dashed line represents the resistivity of epitaxial InGaAs.

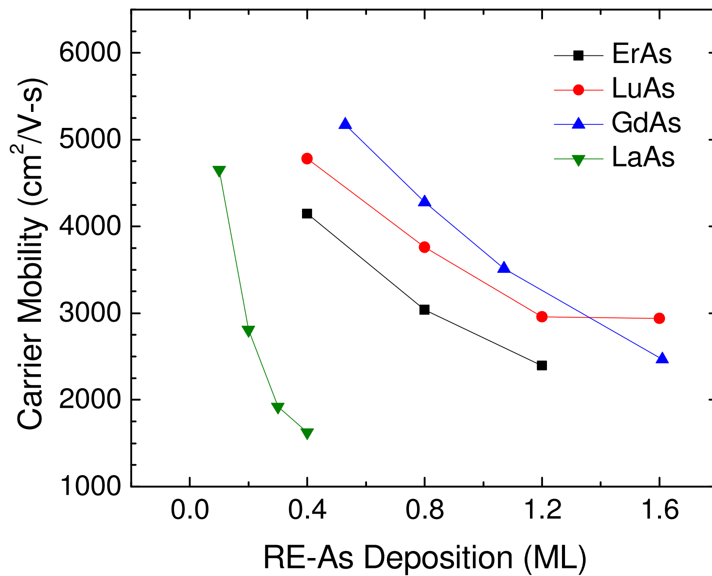

Figure 3.7: Room-temperature electron mobility of superlattices versus increasing RE-As deposition. Both LuAs:InGaAs and GdAs:InGaAs exhibited mobilities uniformly higher than ErAs:InGaAs and significantly higher than LaAs:InGaAs at comparable RE-As depositions.

Temperature-dependent Hall measurements showed the charge carrier concentration to be highly dependent on the amount of RE-As deposition, consistent with previous studies of ErAs:InGaAs [72]. The activation energy can then be extracted from linear fits to semilog plots of the charge carrier concentration as a function of inverse temperature as shown in Figure 3.8 for various depositions of LuAs:InGaAs superlattices. It should be noted that the extracted activation energy is not a measure of the true Fermi level alignment at the RE-As and InGaAs interface but rather a reasonable proxy, since the activation energy represents the average position of the Fermi level at the nanoparticle/matrix interface throughout the superlattice. Higher activation energies correlate with the Fermi level aligning more closely to the middle of the InGaAs bandgap, decreasing free carrier concentration, and increasing dark resistivity. As shown

in Figure 3.9a, the extracted activation energies increased with RE-As deposition, consistent with the dark resistivity measurements. LaAs:InGaAs exhibited the highest energy at 100 meV for 0.4 ML LaAs deposition. Band diagrams (1D Poisson) of various superlattices, shown in Figure 3.9b, utilizing the extracted activation energies as Schottky barrier heights and the room temperature carrier concentration as the doping level for the InGaAs, can give some insight of how the RE-As states can affect the Fermi level alignment, which subsequently affect the overall properties of the photoconductive material.

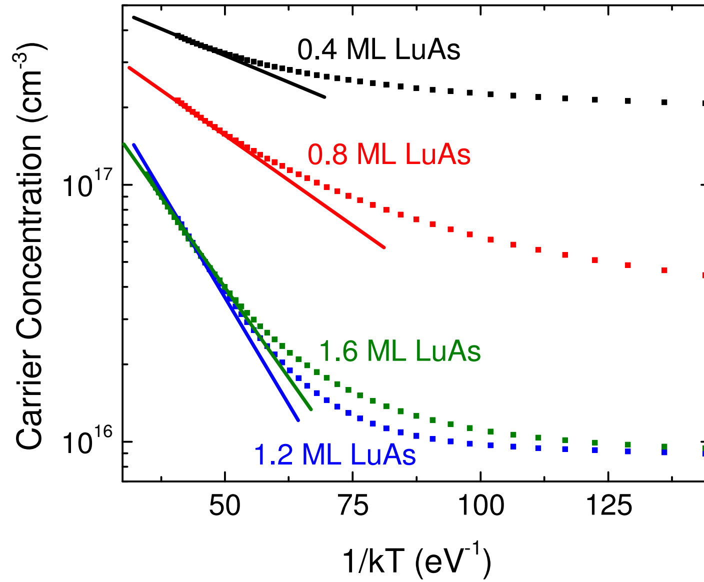

Figure 3.8: Charge carrier concentration versus inverse temperature showing the linear fits used to extract the activation energy.

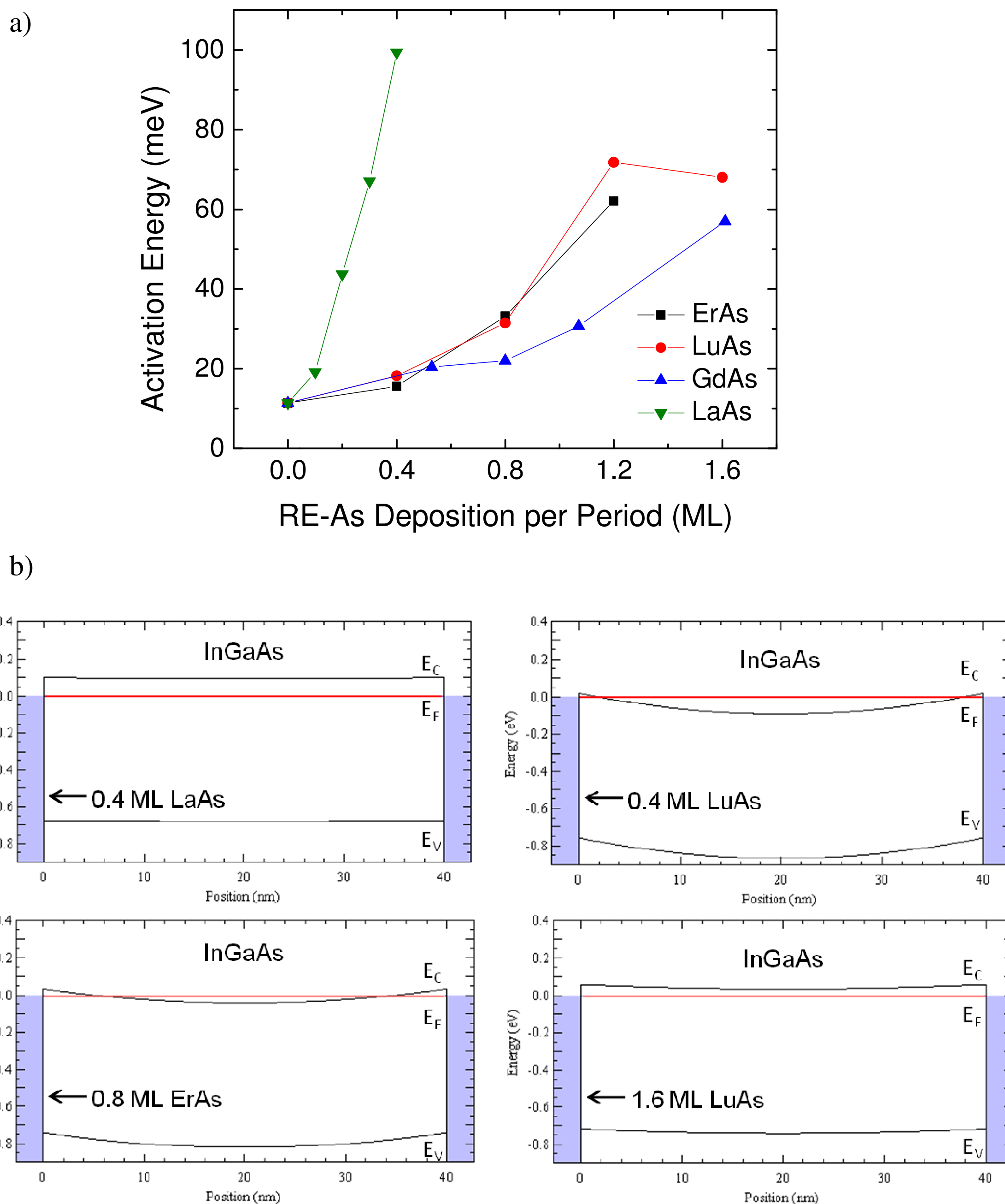

Figure 3.9: a) Activation energy of RE-As superlattices with various depositions. LaAs shows high activation energies for small deposition of RE-As compared to ErAs, LuAs, and GdAs. b) Band diagrams (1D Poisson) of various superlattices using the activation energy as the Schottky barrier height for the nanoparticle/matrix interface and the room temperature carrier concentration as the doping level.

3.4 Carrier Lifetime of RE-As Superlattices

Time-resolved differential pump-probe transmission measurements at 1550 nm were used to evaluate the carrier lifetime of the different nanocomposites, using the method and setup described in Section 2.7.3. The measurements were fitted to the expression $I \sim \exp(-t/\tau)$, where I is the measured normalized differential intensity, t is the time delay of arrival between pump and probe pulses, and τ is the carrier lifetime. As shown in Figure 3.10, the measured carrier lifetimes decreased with increasing RE-As deposition. Much like previous studies of ErAs have shown [102], higher depositions of RE-As increase the interfacial area between the RE nanostructures and the host matrix, where electron-hole recombination is favored, potentially increasing the electron capture cross section and decreasing the carrier lifetime. The GdAs:InGaAs superlattices were uniformly faster than ErAs:InGaAs and LuAs:InGaAs by about 1.3× and 1.8× respectively, achieving the shortest carrier lifetime measured at 1.7 ps for 1.6 ML depositions. RE-As/InGaAs superlattices with greater lattice mismatches, ErAs and LuAs, correlated with longer carrier lifetimes, suggesting a strain-related tunability of the carrier lifetime. However, superlattices containing LaAs do not seem to follow the same lattice mismatch-related trend of the other RE-As superlattices since the nanoparticles likely include multiple crystalline phases and a potentially roughened nanoparticle/matrix interface. The carrier lifetime of the LaAs-deposited material reached a minimum of 5.4 ps for a 0.4 ML deposition before the degradation of the material quality hampered higher depositions of LaAs. In addition, measurements made with increasing pump fluences, which were still on the same order as fluences that would be used to pump a photomixer based upon these materials under CW conditions, showed little change in the carrier lifetime. Figure 3.11 shows the carrier lifetime measurements of a 1.2 ML LuAs:InGaAs superlattice as the fluence is varied from 5 to 10 $\mu J/cm^2$. Although RE-As

recombination centers have been shown to saturate at significantly higher pump fluences [106], such saturation effects are not expected to play a role at the relevant pump powers for photomixer applications in these materials.

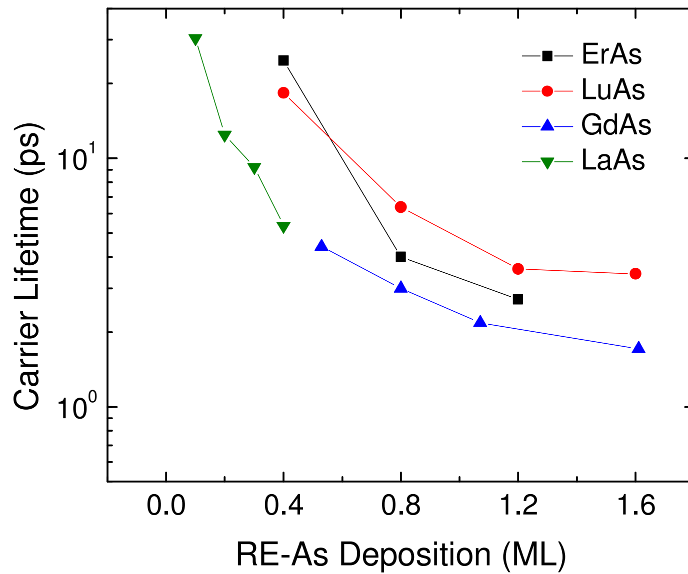

Figure 3.10: Carrier lifetime measurements of superlattices with increasing depositions of RE-As. With the exception of LaAs, lifetime trends correlate with lattice-mismatch between the RE-As and InP. Superlattices containing the nearly lattice-matched GdAs achieved the lowest carrier lifetimes.

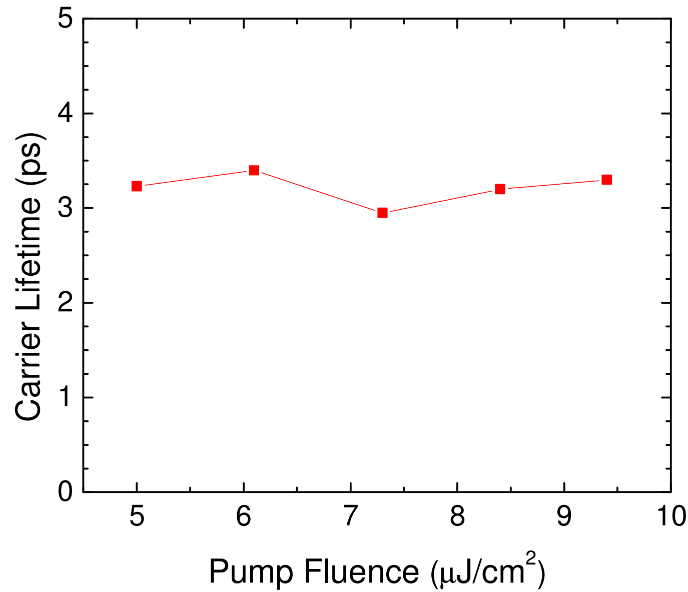

Figure 3.11: Carrier lifetime measurements of a 1.2 ML LuAs:InGaAs superlattice with increasing pump fluences. Carrier lifetime does not seem to be affected by the change in fluence, which suggests that there is no saturation of the states at these power levels.

3.5 Summary

In summary, the material quality, electrical properties, and carrier dynamics of superlattices of ErAs, LuAs, GdAs, and LaAs nanostructures were examined to investigate the possible effects of strain and lattice mismatch of the different RE-As nanoparticles to the InGaAs matrix. However, the strongest effect that was found across all properties was the difference between LaAs and the other RE-As investigated. This difference can be attributed to the formation of multiple LaAs crystalline phases and orientations, which affect the seeding and overgrowth of the host matrix as evidenced directly by the cross-sectional TEM studies and indirectly by the other properties investigated. Furthermore, these differences between the LaAs and the more "well

behaved" single crystalline rocksalt RE-As suggest that the structural quality of the overgrowth may play a key role in the overall properties of RE-As nanocomposites and will be the main topic for the investigation in the Chapter 4.

Diversity in the electrical properties and carrier dynamics between the single crystalline phase forming ErAs, LuAs, and GdAs is more difficult to ascertain and cannot be directly attributed to a strain-related argument. As will be discussed in the following chapter, the growth rate of the RE-As also seems to be important since it can affect the nanoparticle morphology and hence the properties of the materials. For convenience, a summary of all superlattices and the measured properties investigated in this chapter is given in Table 3.2.

Table 3.2: Properties of 30-period RE-As:InGaAs superlattices with the 40 nm period spacing grown at 490 °C. The properties summarized include RE-As species, RE-As deposition (Dep), RE-As growth rate (GR), root-mean-squared surface roughness (RMS SR), room temperature mobility (μ), room temperature dark resistivity (ρ), room temperature carrier concentration (n), Fermi level based on room temperature carrier concentration using Nilsson equation [107], activation energy from temperature dependent Hall (E_a), and carrier lifetime (τ).

RE-As	Dep. (ML)	GR (ML/s)	RMS SR (nm)	μ (cm^2/V-s)	ρ (Ω-cm)	n (cm^{-3})	E_F-CB (meV)	E_a (meV)	τ (ps)
LuAs	0.4	0.07	0.43	4780	0.0032	4.07×10^{17}	35.02	18.2	18.34
	0.8	0.07	0.37	3758	0.0071	2.31×10^{17}	12.80	31.45	6.36
	1.2	0.07	0.70	2957	0.0243	8.66×10^{16}	-19.14	71.76	3.59
	1.6	0.07	10.2	2937	0.0297	7.14×10^{16}	-24.84	68.03	3.43
ErAs	0.4	0.05	0.25	4133	0.0023	6.39×10^{17}	56.25	15.58	24.71
	0.8	0.05	0.28	3030	0.007	2.93×10^{17}	21.72	33.15	4.01
	1.2	0.05	0.56	2391	0.0193	1.34×10^{17}	-5.48	62.11	2.71
GdAs	0.5	0.02	0.24	5170	0.0041	2.91×10^{17}	21.39	20.4	4.41
	0.8	0.02	0.51	4278	0.0041	3.51×10^{17}	28.79	22	3.04
	1	0.02	0.77	3513	0.0074	2.37×10^{17}	13.72	30.7	2.18
	1.6	0.02	5.95	2466	0.0289	8.74×10^{16}	-18.91	57	1.71
LaAs	0.1	0.02	0.879	4558	0.0134	1.02×10^{17}	-14.31	19.16	30.38
	0.2	0.02	3.61	2792	0.0375	5.95×10^{16}	-30.10	43.74	12.44
	0.3	0.02	8.18	1918	0.0879	3.7×10^{16}	-43.30	65.34	9.218
	0.4	0.02	9.71	2132	0.1922	1.52×10^{16}	-67.00	99.39	5.35

Chapter 4: Growth Enhancements of RE-As:InGaAs Superlattices

The previous chapter investigated the effects of exchanging the RE-As species in an InGaAs based superlattice while attempting to maintain all other variables the same. Only a modest difference was observed amongst the single-phase-forming RE-As compounds (ErAs, GdAs, and LuAs). LaAs, which forms multiple crystalline phases and orientations, exhibited drastic effects on the structural, electrical, and carrier dynamic properties of the examined superlattices, compared with the single-phase RE-As. The structural quality of the InGaAs overgrowth of the LaAs nanostructures was severely degraded for even small amounts of deposited LaAs and is the likely culprit for the difference in the properties of the resulting nanocomposite. This suggests that the structural quality of the overgrowth might also play a role in the properties of the other well-behaved RE-As at high depositions when the overgrowth begins to deteriorate. This chapter will investigate superlattices of LuAs nanoparticles embedded in an InGaAs matrix grown using a combination of surfactant-mediated growth via bismuth during the InGaAs overgrowth and varying LuAs growth rates. The properties of the resulting photoconductive materials are also discussed.

4.1 Surfactant-Mediated Growth

Surfactant-assisted growth has been an integral part in the development of high quality epitaxial materials [108]. The term surfactant was applied early in regards to epitaxial growth to mean any surface-active species that would alter the surface kinetics of the ad-atoms. The use of surfactants was first introduced by Copel *et al*. [109,110] to investigate the effects of adding a third element, arsenic, to lower the surface free energy

during heteroepitaxial growth of silicon and germanium films. Germanium grows on silicon (100) in a Stranski-Krastanov (SK) growth mode, meaning that germanium wets to the silicon surface and forms films in a layer-by-layer mode during the first few monolayers of deposition. As the germanium film continues to grow, the strain energy from large lattice mismatch increases such that it becomes energetically favorable for the growth to continue in an islanding mode. Growth of silicon on germanium (100) or germanium/silicon (100), on the other hand, grows in a Volmer-Weber (VW) mode where the silicon does not wet to the surface of the germanium and grows in an islanding mode from the start. The 3D islanding mode leads to highly dislocated and defected films as the different island boundaries coalesce with one another as the growth continues. The addition of a single monolayer of arsenic to the surface lowers the surface free energy by providing one extra electron per surface atom, filling the dangling bonds that occur on the silicon (100) or germanium (100) surface, and creating a stable termination [111]. The arsenic-passivated surface changes the thermodynamics and growth kinetics of the surface and suppresses the islanding growth mode for germanium on silicon and vice versa without incorporating into the films. Although the arsenic did not relieve the presence of strain from sufficiently thick films of germanium on silicon substrates, thin films of germanium remained coherently strained. Copel *et al*. [109,110] showed that arsenic could be used as a surfactant to improve the quality and thickness of the germanium grown on silicon films and silicon grown on germanium/silicon films, both of which had previously been very challenging [112,113].

A theory that explains how surfactants affect epitaxial growth was put forth by Massies and Grandjean [114] and further described by Tournie *et al*. [115]. They propose separating surfactants into two distinct categories, reactive and non-reactive surfactants, based on their surface interactions and kinetics. Non-reactive surfactants are used

primarily for homoepitaxy where strain does not play a role in the growth mode of the epitaxial layer. These elements are weakly bonded to the atoms on the surface of the semiconductor and are located on interstitial sites. The bonding complexes created by these minimally incorporating interstitials decrease the effective bond strength and lower the hopping potential of the semiconductor ad-atoms, resulting in an increased surface diffusion length [114]. These interactions also suppress potential islanding from SK growth modes by lowering the Ehrlich-Schwoebel barrier [116,117], which allows ad-atoms to hop to lower atomic layers, thus promoting a Frank-van der Merwe (FM) growth mode. Non-reactive surfactants for III-V homoepitaxy can generally be found in group-IV elements such as Sn and Pb. Virtual non-reactive surfactants [118] that also promote FM growth mode in III-V homoepitaxy can be found in group-III elements and are used when the surface is switched from a group-V terminated surface to a group-III. Reactive surfactants, on the other hand, are primarily used for heteroepitaxy where strain and surface segregation of the ad-atoms plays an important role in the surface kinetics. These elements bond on substitutional sites and as such can be incorporated in dilute amounts depending on the growth conditions. Segregation of the surfactant atoms at the growth front forces an exchange reaction between the surfactant atom and the semiconductor ad-atom. This exchange results in a subsurface incorporation of the ad-atom beneath the segregating surfactant layer [109,110]. The ad-atom is thus surrounded below by the growing film and above by the surfactant layer, resulting in an increase of the hopping potential for the ad-atoms. These interactions thus decrease the ad-atom sub-surface diffusion length [114,119], which is crucial to suppress phase segregation and islanding in highly strained materials and heteroepitaxy and promote a FM growth mode. Reactive surfactants for III-V heteroepitaxy can generally be found in group-V elements such as As, Sb, and Bi and group-VI elements such as Te.

Antimony has been used extensively as a surfactant for growing germanium films on Si (100) [110,120,121] and on InP (100) [122]. It has also been used to as a method to grow highly strained InGaAs [123] and increase the incorporation of nitrogen in GaInNAs [124] and GaInNAsSb [125-130] quantum well layers for high quality lasers on GaAs. However, antimony tends to incorporate in these materials under standard growth temperatures and conditions. Bismuth, on the other hand, is a much larger atom with a slightly lower electronegativity than antimony and incorporates at substrate temperatures much lower than standard growth conditions [131,132]. Bismuth, much like antimony, has also been demonstrated to act as a surfactant to improve Ge/Si interfaces [133,134] and the material quality of highly strained $In_xGa_{1-x}As$/GaAs heterostructures [135], been used to increase the incorporation of nitrogen in dilute GaNAs and GaInNAs layers on GaAs [131,136], and improve the quality of lattice-matched layers of InGaAs on InP [137]. Despite the improved materials quality offered by surfactant-mediated growth, there has been no research exploring this enhancement on RE-As nanocomposites and will be one of the techniques used for the investigation in this chapter.

4.2 Growth Rate-Dependent RE-As Nanoparticle Morphology

The effects on nanoparticle morphology due to different RE-As growth rate was first explored in the ErSb:GaSb system by Hanson [70]. The resulting nanocomposites showed a modest decrease in the carrier lifetime as the ErSb growth rate was decreased from 0.09 ML/s to 0.04 ML/s [138]. The effects on the electrical properties, however, were less advantageous as the resistivity decreased while mobility only slightly improved [138]. The effect on both nanoparticle size and density, shown in Figure 4.1, was far more prominent. The nanoparticles grew significantly larger with a slower ErSb growth

rate and since the total deposition was kept constant the overall surface density of the nanoparticles decreased. The effects of RE-As growth rate on the structural quality of the matrix overgrowth and its effects on the properties of the nanocomposites at RE-As lower growth rates, however, remains unexplored and will also be investigated as a growth enhancement technique in this section.

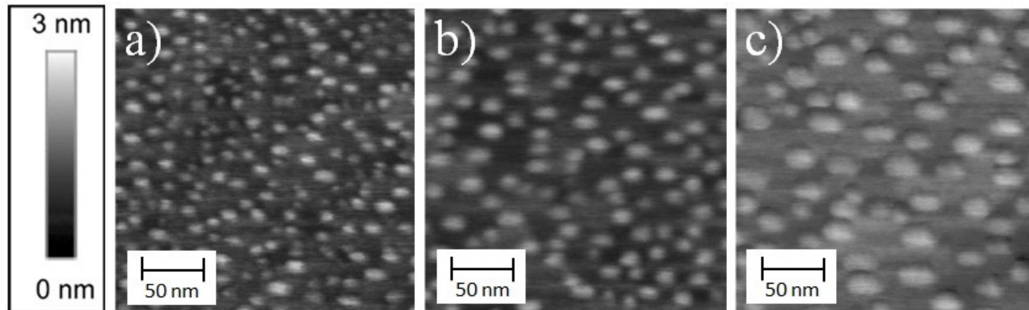

Figure 4.1: AFM images of 0.75 ML deposition of uncovered ErSb nanoparticles grown on GaSb at a) 0.09 ML/s, b) 0.06 ML/s, and c) 0.04 ML/s. The lower deposition rate formed the largest sized nanoparticles and the lowest nanoparticle surface density (reproduced from [70]).

4.3 Growth and Structure of Enhanced LuAs:InGaAs Superlattices

As detailed in Chapter 3, samples were grown on semi-insulating InP (100) substrates using the same InGaAs growth rate, As/III BEP ratio, and substrate temperature. A bismuth BEP of 1×10^{-7} Torr was supplied during growth of the InGaAs layers on selected superlattices and was not expected to incorporate at the 490 °C growth temperature [137]. Furthermore, bismuth is expected to fully desorb from the surface of the substrate within a few seconds after closing of the bismuth source shutter based on estimated desorption rates of the bismuth calculated from RHEED specular intensities at this growth temperature [136]. The LuAs growth rate (GR) was varied from 0.07 ML/s to

0.01 ML/s. The growth rates and depositions are given in terms of equivalent number of RE-As monolayers (ML), using RHEED intensity oscillations and XRD measurements of full LuAs films in the same method as was discussed in Chapter 3. The superlattice structure consisted of a 150-nm InGaAs buffer layer using bismuth to assist the growth. At the end of the buffer layer, all shutters except for the As_2 source were closed for two seconds to allow the majority of the bismuth to desorb and thus not interfere with the LuAs growth kinetics. A fixed deposition of LuAs was then grown and allowed to soak under an As_2 flux for another 2 seconds after the Lu shutter was closed before proceeding with 40 nm of bismuth assisted InGaAs overgrowth. The LuAs deposition and bismuth assisted InGaAs overgrowth steps constituted a single period which was repeated thirty times. All superlattice structures for this investigation used this design except for those used for TEM studies, which varied in the amount of LuAs deposited per period. Specifically, TEM structures began with depositions of 0.2 ML in the first period and increased by 0.2 ML per period up to 3.0 ML. All structures that used bismuth to assist the InGaAs growth followed the same 2 second timing sequence. The superlattices that used the enhancement techniques were compared with the superlattices of LuAs already discussed in Chapter 3 to assess the differences.

For all superlattices containing effective LuAs depositions of 1.2 ML per period or less, the observed RHEED pattern during growth blurred slightly within the first 10 nm of overgrowth and subsequently recovered a streaky pattern. However, for materials with an effective LuAs deposition of 1.6 ML, the superlattice with 0.07 ML/s GR recovered a streaky RHEED pattern after ~28 nm of overgrowth during the first few periods and the recovery degraded as the number of periods increased. In contrast, the superlattices with 0.07 ML/s that used bismuth as a surfactant recovered a streaky RHEED pattern after ~14 nm of overgrowth for depositions up to 1.6 ML, ~20 nm for 2.0

ML, and ~26 nm for 2.4 ML depositions. Furthermore, the superlattices with 0.02 ML/s and 0.01 ML/s that also used bismuth recovered the streaky pattern within ~12 nm for depositions up to 1.6 ML. For depositions of 2.0 ML, 2.4 ML, and 2.8 ML growth at 0.01 ML/s, recovery of the streaky RHEED pattern required ~15 nm, ~18 nm, and ~23 nm of InGaAs overgrowth. All superlattices that used bismuth recovered streaky RHEED patterns throughout all 30 periods. Figure 4.2 shows the RHEED pattern of the InGaAs overgrowth after 30 periods of 1.6 ML LuAs superlattices with the LuAs GR at 0.07 ML/s without bismuth, 0.07 ML/s with bismuth, and 0.01 ML/s with bismuth. The slowest LuAs GR that used bismuth during the InGaAs overgrowth had the clearest 2× pattern for the [110] direction.

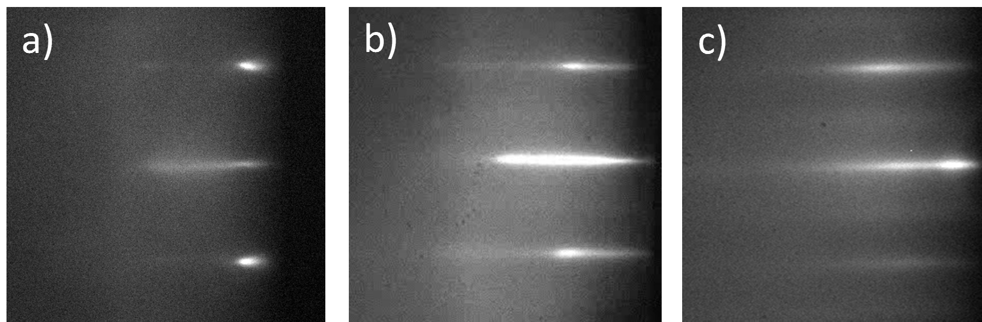

Figure 4.2: RHEED patterns of InGaAs overgrowth after 30 superlattice periods of 1.6 ML of LuAs grown at a) 0.07 ML/s without bismuth, b) 0.07 ML/s with bismuth, and c) 0.01 ML/s with bismuth. The diffraction pattern for the superlattice with the combined enhancements appears streakier and the 2× reconstruction is almost visible compared to the superlattice that used only bismuth.

Symmetric ω-2θ XRD scans around the (004) diffraction peak of the InP substrate, Figure 4.3, showed degraded superlattice peak fringes, indicative of poor quality period interfaces, for an effective deposition of 1.6 ML per period at the 0.07 ML/s LuAs GR without bismuth. The XRD scans show some improvement in the superlattice peak fringes for the 0.07 ML/s GR when bismuth is used and significant

improvement when the GR is then lowered to 0.02 ML/s and 0.01 ML/s. Root-mean-squared (RMS) surface roughness as measured by atomic force microscopy (AFM) was over 10 nm for the superlattice grown without bismuth using 0.07 ML/s LuAs GR at an effective deposition of 1.6 ML, shown in Figure 4.4. The application of bismuth as a surfactant reduced the surface roughness and delayed the onset of material degradation to higher depositions of LuAs. Combining the bismuth surfactant during the InGaAs growth with a slower LuAs GR further decreases the surface roughness and allows for effective depositions up to and including 2.0 ML per period while maintaining an RMS surface roughness of ~1 nm, in agreement with RHEED observations during sample growth and XRD studies of the structural quality. These two growth enhancements allow for a ~50% increase in the LuAs deposition in the 30-period superlattices while maintaining good structural quality of the material compared to the faster LuAs GR without bismuth.

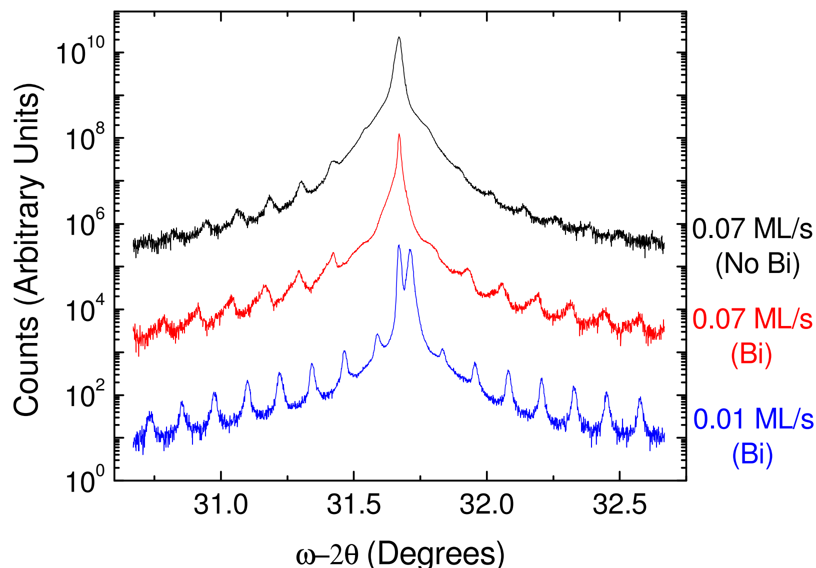

Figure 4.3: X-ray diffraction symmetric *ω-2θ* scans around the (004) diffraction peak of InP for 1.6 ML LuAs. The stronger fringe peaks are indicative of smoother and more sharply defined period interfaces.

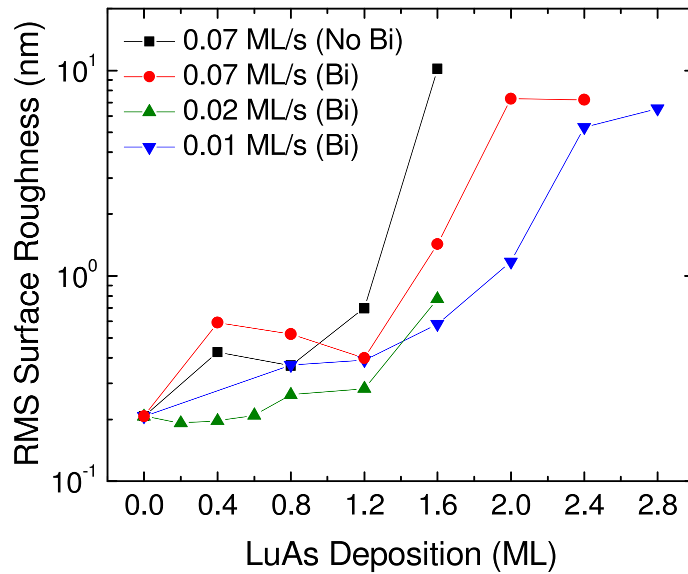

Figure 4.4: Root-mean-squared surface roughness AFM scans of superlattices with increasing LuAs deposition with and without bismuth and different LuAs growth rates. Superlattices that combined both bismuth and slower LuAs growth rate had the lowest surface degradation at the highest depositions of LuAs.

Cross-sectional TEM studies with increasing deposition of LuAs nanostructures per period, shown in Figure 4.5a, indicate surface modulation after an effective LuAs deposition of 1.6 ML as shown previously [139] and consistent with other studies of ErAs on InGaAs with a similar ErAs GR [41]. By contrast, cross-sectional TEM studies that maintained the same LuAs GR and utilized Bi as a surfactant during the InGaAs overgrowth, shown in Figure 4.5b, showed a substantial improvement in the quality of the period interfaces. Surface modulations are clearly visible after an effective deposition of 2.4 ML with progressively degraded period interfaces at higher depositions. By combining Bi with a slow LuAs GR of 0.01 ML/s, shown in Figure 4.5c, the material maintains clearly visible period interfaces even up to an effective deposition of 3.0 ML.

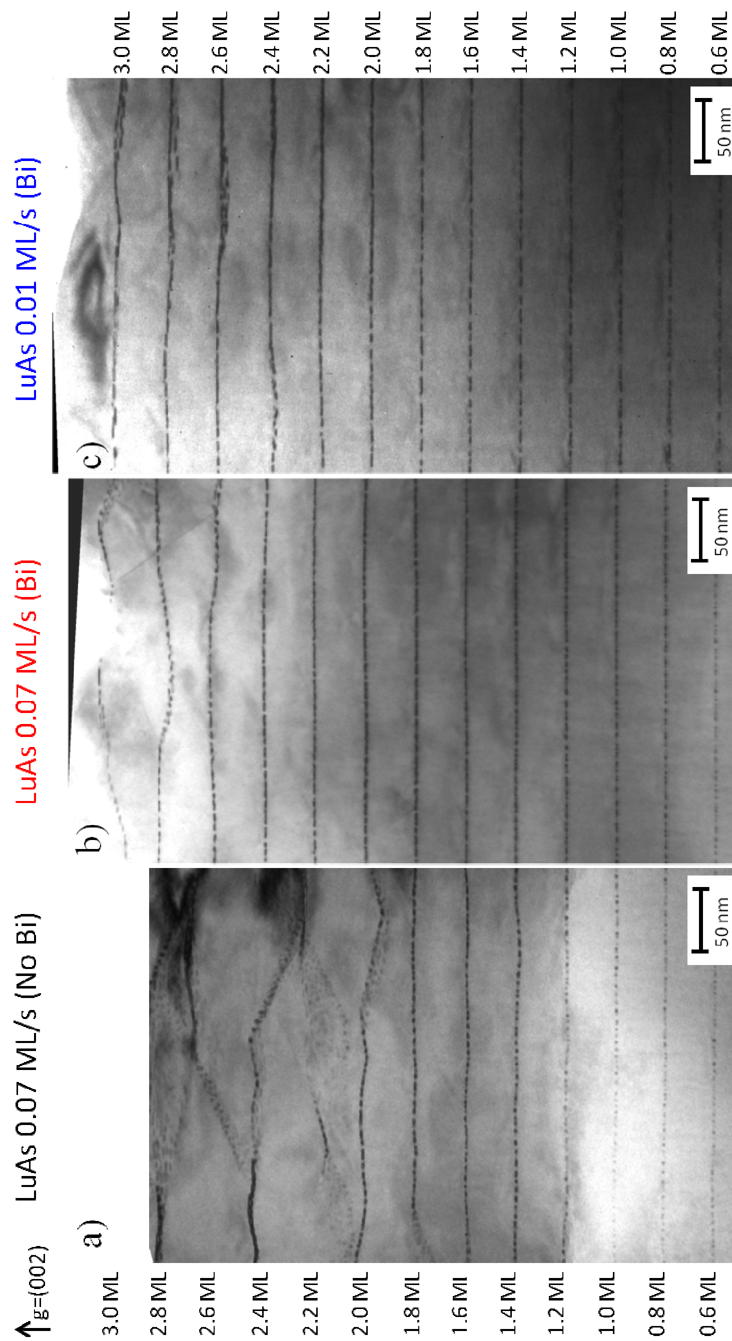

Figure 4.5: Cross-sectional TEM study of LuAs-containing superlattice structures with increasing deposition of LuAs per period for LuAs growth rates of a) 0.07 ML/s without using bismuth, b) 0.07 ML/s with bismuth, and c) 0.01 ML/s with bismuth. The superlattice structure that combined both enhancements had the best overall material overgrowth quality.

The improvement in the quality of the material grown due to the presence of bismuth can be understood from the lowering of the surface free energy already discussed in section 4.1. However, the improvement due to the changing RE-As growth rate requires some consideration. It is suspected that a critical local density of RE atoms is required before a nanoparticle will form, since a nanoparticle with a minimum height of 4 ML is needed to stabilize the rocksalt crystal structure [48]. As such, slowing down the RE-As growth rate means that critical local densities are less common on the surface leading to the formation of fewer nanoparticles. As the RE atoms continue to adsorb to the surface, it is more likely that the atoms will encounter an already formed nanoparticle to adhere to, rather than reaching a critical local density with other loose RE atoms to form a new nanoparticle. Hence a slower growth rate leads to larger, less dense nanoparticles, which increases the mean spacing between nanoparticles where the III-V surface is exposed. The increase in exposed III-V surface allows for an improved seeding of the overgrowth and is likely the reason for higher quality material. If bismuth had also been used during the growth of the RE-As, the surface diffusion length of the RE atoms presumably would have been decreased and would have increased the number of local critical density sites required to form nanoparticles. As such, bismuth would have opposed the benefit of slowing the growth rate and is the main reason for the 2 second timing delay sequence implemented in the growth procedures. This hypothesis was confirmed by the growth of a 1.6 ML LuAs superlattice grown at 0.01 ML/s for LuAs that used bismuth during the growth of the LuAs and InGaAs. This superlattice had a surface roughness twice that of the same superlattice that implemented the 2 second timing. It is also important to note that even though the 2 second timing sequence is sufficient to desorb the majority of the bismuth from the surface, not all of the bismuth is gone before growth of the LuAs begins. Therefore it is possible that LuBi is formed in

small quantities on the surface. However, LuBi is not expected to remain for long because the continuous As_2 overpressure is two orders of magnitude higher than that of the bismuth and because the enthalpies of formation for RE-As are on average three times larger than those of the RE-Bi [140,141,104]. So not only is there more arsenic on the surface, which the Lu atom can interact with, even if some LuBi stable nanostructure is formed the arsenic will eventually dissociate it so that it will form bonds to the Lu atoms leading to LuAs nanostructures.

4.4 Electrical Properties of Enhanced LuAs:InGaAs Superlattices

Room-temperature Hall measurements indicated electrons as the majority carriers for all measured structures, consistent with previous studies of other RE-As:InGaAs nanocomposites [41,139]. The Hall measurements showed an initial drop in dark resistivity at low LuAs depositions compared to measured resistivity values of 0.07 Ω-cm for control samples of epitaxial InGaAs, and then a gradual increase with increasing depositions of LuAs, as shown in Figure 4.6. This trend is consistent with previous studies of RE-As:InGaAs superlattices in Chapter 3, where the RE-As nanocomposites initially appear to dope the material at low depositions and act as recombination centers at higher depositions, reducing the mobility and conductivity [72,139]. Superlattices grown with bismuth as a surfactant during the InGaAs overgrowth showed a ~15× increase in the dark resistivity for the same effective LuAs deposition of 1.6 ML at a 0.07 ML/s GR. Lowering the LuAs GR while also using bismuth further increased the dark resistivity for effective depositions less than 1.6 ML with the 0.01 ML/s GR having the highest resistivities. However, there seems to be a convergence of the resistivities at ~1.6 ML depositions for all of the explored GRs. Effective depositions of 2.0 ML and higher

begin to diverge with the 0.07ML/s GR degrading in resistivity and the 0.01 ML/s GR continuing to increase until a maximum resistivity of 0.75 Ω-cm for a deposition of 2.4 ML. This constitutes a ~25× overall increase in the maximum resistivity considering that the combination of bismuth and slow LuAs GR allow for an increase in the total amount of LuAs deposited.

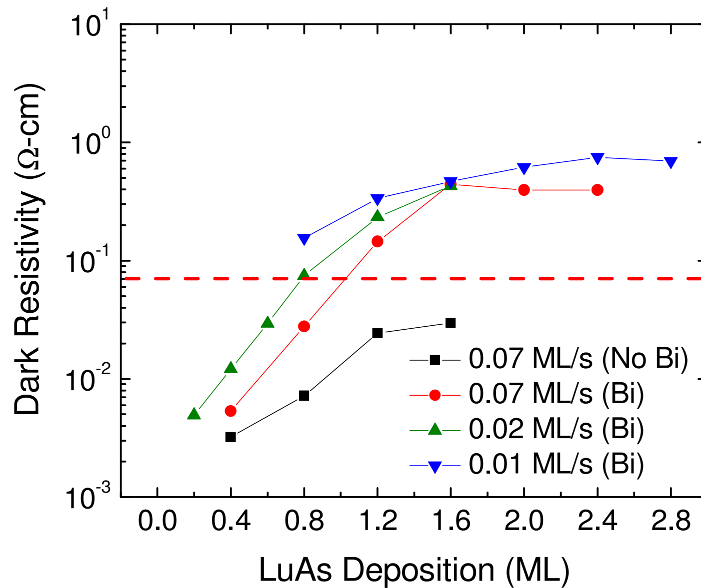

Figure 4.6: Room-temperature dark resistivity measurements of superlattices as a function of LuAs deposition per superlattice period. Superlattices grown with bismuth and a slow LuAs growth rate exhibited significantly higher resistivities than other superlattices except at the 1.6 ML deposition where the growth rate had no apparent effect. The dashed line represents the resistivity of epitaxial InGaAs.

The carrier mobilities, shown in Figure 4.7, indicate a decreasing trend with increasing deposition of LuAs. The superlattices grown with both bismuth and 0.01 ML/s LuAs GR show consistently higher mobilities than all other samples achieving mobilities greater than 3000 cm^2/V-s for all LuAs depositions investigated. The improvement in the electrical properties can be attributed to the improved material quality of the InGaAs

overgrowth after every period. The slow LuAs GR promotes the formation of larger nanoparticles at a lower density [70], which leaves larger areas of exposed InGaAs between nanoparticles to seed the overgrowth. When larger exposed InGaAs areas are combined with the layer-by-layer growth mode promoted by the use of bismuth as a surfactant, material quality improves along with the electrical properties.

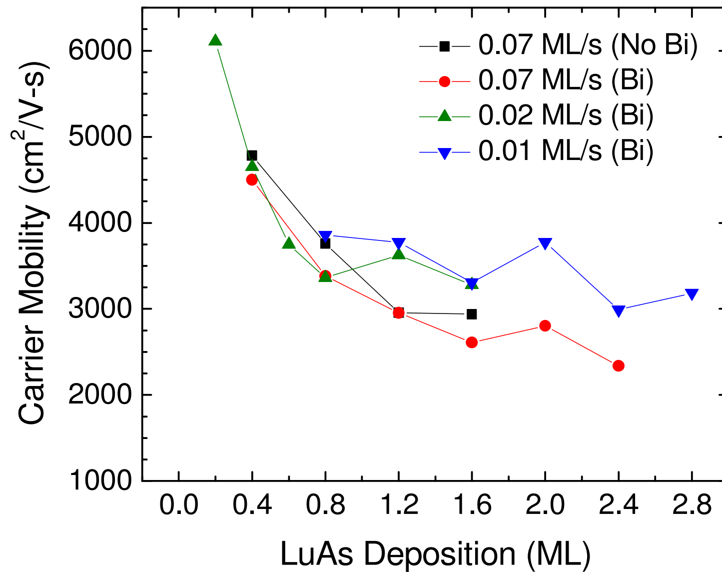

Figure 4.7: Room-temperature electron mobility as a function of LuAs deposition for LuAs:InGaAs superlattices. Superlattices that combined bismuth and a slow 0.01 ML/s LuAs growth rate exhibited uniformly higher mobilities than all other superlattices in this investigation.

Temperature-dependent Hall measurements show strong temperature dependence on the measured charge carrier concentration and were used to estimate the activation energy. The extracted activation energies, shown in Figure 4.8, increased with increasing depositions of LuAs, reaching a maximum of 72 meV for a deposition of 1.2 ML grown at 0.07 ML/s GR without bismuth and falling to 68 meV for a deposition of 1.6 ML. In contrast, the superlattices grown at 0.07 ML/s LuAs GR with bismuth had significant

improvement in the activation energy reaching a maximum of 177 meV for a deposition of 1.6 ML and subsequently degrading at higher depositions. The superlattices that combined a 0.01 ML/s LuAs GR with bismuth had higher activation energies overall than all other measured materials. The same convergence observed for the dark resistivity is observed in the activation energy for effective depositions of 1.6 ML, however, the 0.01 ML/s GR with bismuth continues to increase reaching a maximum of 185 meV for a deposition of 2.0 ML, an approximate 2.5× improvement over the faster GR LuAs without bismuth. Figure 4.9 shows the representative band diagram for the 2.0 ML LuAs superlattice with bismuth and 0.01 ML/s GR. The activation energy appears to level off at ~177 meV for depositions of 2.4 ML and 2.8 ML of LuAs as the increased deposition of LuAs takes on more film like qualities. This effect is also offset by the lower quality of the InGaAs overgrowth at higher LuAs depositions because there is less InGaAs available between nanoparticles to seed the next period. The degradation in the activation energies correlate with the quality of the material evidenced by the RMS surface roughness measurements from the AFM studies. As the material quality degrades, the nanoparticle/matrix interface is also affected and is likely the reason for the deterioration of the average Fermi level alignment for the 0.07 ML/s LuAs GR with bismuth at the 2.0 ML and 2.4 ML depositions.

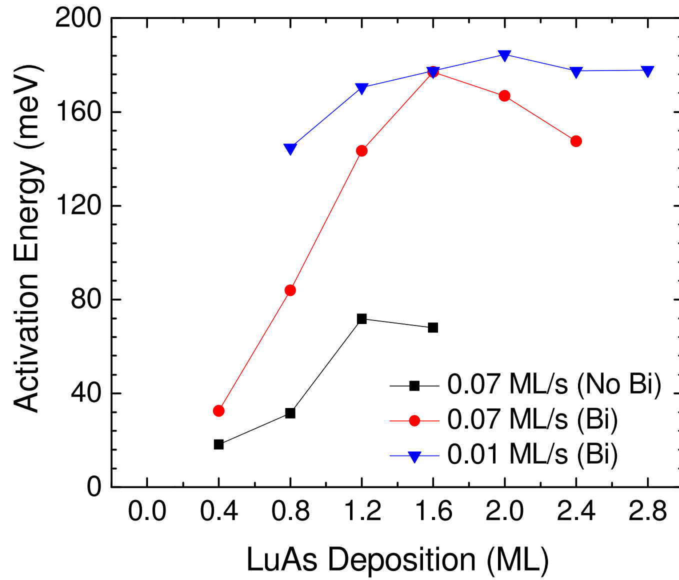

Figure 4.8: Activation energy of LuAs superlattices with increasing LuAs deposition. The superlattices that combined both enhancement techniques had the highest energies.

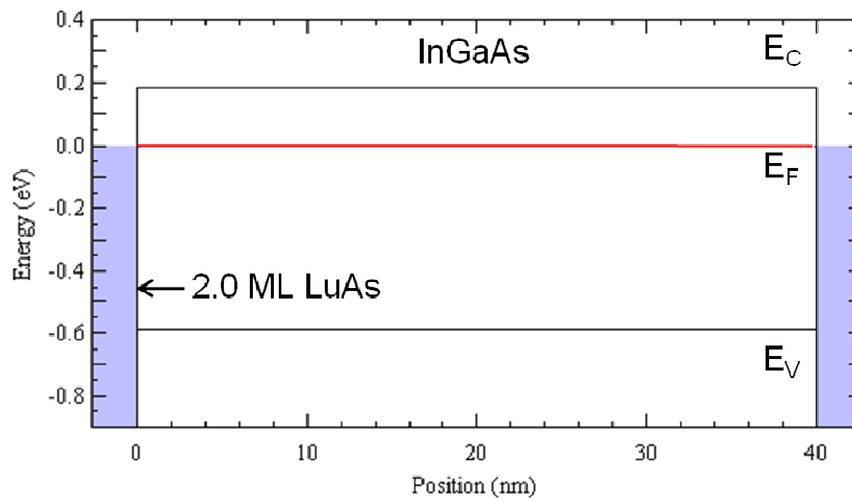

Figure 4.9: Band diagram (1D Poisson) of one period of the 2.0 ML LuAs superlattice that used bismuth and 0.01 ML/s LuAs growth rate, showing a diagram that is nearly flatband. The band diagram used the activation energy as the Schottky barrier height and the room temperature carrier concentration as the doping level for the InGaAs.

4.5 Carrier Lifetimes of Enhanced LuAs:InGaAs Superlattices

Time-resolved differential pump-probe transmission at 1550 nm was used to measure the carrier lifetimes of the superlattices, shown in Figure 4.9. The measured carrier lifetimes decreased with increasing deposition of LuAs down to a minimum of 3.4 ps for an effective deposition of 1.6 ML grown at 0.07 ML/s without bismuth. In contrast, the superlattices that used bismuth had an over 2× decrease in the carrier lifetime achieving 1.6 ps for 2.8 ML of LuAs grown at 0.01 ML/s and did not seem to be as affected by the growth rate of the LuAs as the electrical properties. This suggests that the quality of the InGaAs overgrowth improves the carrier lifetime, possibly by decreasing the carrier scattering due to crystal defects between nanoparticle layers. It is interesting, however, that the nanoparticle morphology has very little effect on the carrier lifetimes and the slight deviation of this trend, observed for depositions of 2.0 ML and 2.4 ML at 0.07 ML/s LuAs GR, can be attributed to the lower quality InGaAs overgrowth, supported by AFM studies. It is possible that the lower quality InGaAs increases the carrier scattering before they reach the LuAs nanoparticles where electron-hole recombination is favored.

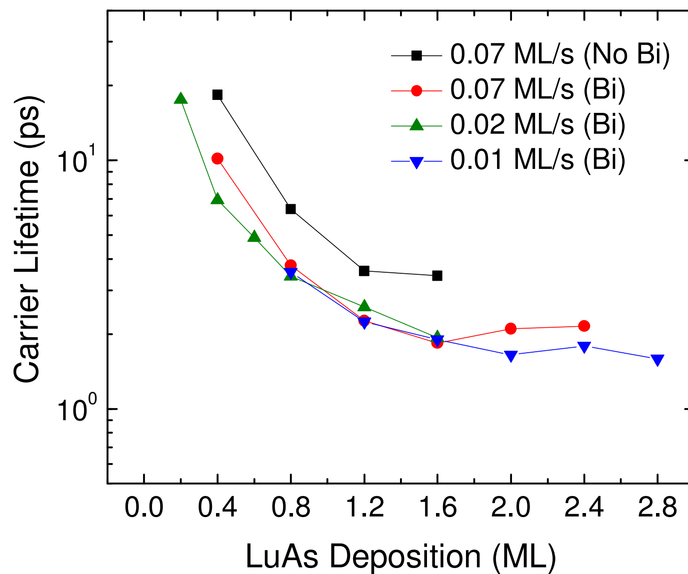

Figure 4.10: Carrier lifetime measurements using differential pump-probe transmission of superlattices with increasing deposition of LuAs. Overall trends in the carrier lifetime seem more affected by the presence of bismuth during growth than by the LuAs growth rate. Superlattices using bismuth with depositions of 2.8 ML of LuAs at 0.01 ML/s achieved the lowest carrier lifetimes at 1.6 ps

4.6 Summary

In summary, the material quality, electrical properties, and carrier lifetimes of superlattices of LuAs embedded in an InGaAs matrix were investigated to assess the effects of using bismuth as a surfactant for the InGaAs overgrowth and slow LuAs growth rate. The material quality shows substantial improvement through the use of bismuth and it is further improved when the LuAs growth rate is subsequently lowered to 0.01 ML/s. The improvement in overgrowth quality allowed for a ~50% increase in the amount of RE-As deposited before the material degraded significantly. The electrical properties showed a 25× improvement in the dark resistivity, reaching a maximum of

0.75 Ω-cm, while maintaining mobilities over 3000 cm^2/V-s for an effective deposition of 2.4 ML of LuAs grown at 0.01 ML/s with bismuth. The activation energies were uniformly higher for the structures that used bismuth and a lower LuAs growth rate, reaching a maximum of 185 meV for a deposition of 2.0 ML. The decay in the activation energy for the 0.07 ML/s LuAs growth rate with bismuth at the 2.0 ML and 2.4 ML depositions can be attributed to the degradation in the material quality potentially affecting the integrity of the nanoparticle/matrix interface. Carrier lifetimes show a substantive decrease for the structures that used Bi, with less dependence on the LuAs growth rate, achieving a lifetime of 1.6 ps for a 2.8 ML deposition of LuAs grown at 0.01 ML/s with bismuth.

The combination of bismuth as a surfactant during the InGaAs growth and a slower LuAs growth rate has demonstrated an improvement in the material quality, electrical properties, and carrier lifetimes. However, these improvements are still short of both the resistivities needed to mitigate ohmic heating due to the dark current as well as the carrier lifetimes required to improve the spectral response of the material. How these parameters affect the overall output power of a photomixer will be assessed in Chapter 7. Further optimizations such as changing the RE atom while using the enhancement techniques or varying the superlattice period will be explored in the following chapter. For convenience, a summary of all superlattices and the measured properties investigated in this chapter is given in Table 4.1.

Table 4.1: Properties of bismuth-enhanced LuAs superlattices with 30 periods of 40 nm of InGaAs grown at 490 °C and various LuAs growth rates. The properties summarized include LuAs deposition (Dep), LuAs growth rate (GR), root-mean-squared surface roughness (RMS SR), room temperature mobility (μ), room temperature dark resistivity (ρ), room temperature carrier concentration (n), Fermi level energy relative to the InGaAs conduction band based on room temperature carrier concentration using the Nilsson equation [107], activation energy from temperature dependent Hall (E_a), and carrier lifetime (τ).

LuAs Dep. (ML)	LuAs GR (ML/s)	RMS SR (nm)	μ (cm^2/V-s)	ρ (Ω-cm)	n (cm^{-3})	E_F-CB (meV)	E_a (meV)	τ (ps)
0.4	0.07	0.59	4499	0.0053	2.6×10^{17}	17.05	32.5	10.18
0.8	0.07	0.52	3381	0.0278	6.65×10^{16}	-26.91	83.9	3.78
1.2	0.07	0.40	2951	0.1448	1.46×10^{16}	-68.08	143.4	2.26
1.6	0.07	1.43	2609	0.4429	5.40×10^{15}	-94.02	177.0	1.84
2.0	0.07	7.30	2803	0.3963	5.62×10^{15}	-92.99	166.8	2.10
2.4	0.07	7.20	2336	0.3969	6.73×10^{15}	-88.29	147.5	2.15
0.2	0.02	0.19	6110	0.0049	2.07×10^{17}	8.88	-	17.55
0.4	0.02	0.20	4651	0.0121	1.11×10^{17}	-11.75	-	6.93
0.6	0.02	0.21	3749	0.0293	5.68×10^{16}	-31.41	-	4.89
0.8	0.02	0.26	3362	0.0744	2.50×10^{16}	-53.92	-	3.41
1.2	0.02	0.28	3625	0.2334	7.38×10^{15}	-85.92	-	2.57
1.6	0.02	0.77	3280	0.4287	4.44×10^{15}	-99.11	153.6	1.94
0.8	0.01	0.37	3860	0.1561	1.04×10^{16}	-77.08	144.7	3.55
1.2	0.01	0.39	3776	0.3367	4.91×10^{15}	-96.51	170.4	2.24
1.6	0.01	0.58	3305	0.4678	4.04×10^{15}	-101.58	177.5	1.90
2.0	0.01	1.17	3774	0.6166	2.68×10^{15}	-112.19	184.5	1.65
2.4	0.01	5.30	2989	0.7491	2.79×10^{15}	-111.20	177.5	1.79
2.8	0.01	6.53	3183	0.6918	2.83×10^{15}	-110.77	177.8	1.59

Chapter 5: Optimizations to Enhanced RE-As:InGaAs Superlattices

The previous chapter investigated two growth enhancement techniques and their effects on the properties of LuAs-containing superlattices. By combining surfactant-mediated growth of the InGaAs matrix with larger, less dense LuAs nanoparticles, the structural quality of the grown material improved considerably. The dark resistivities and carrier lifetimes were also improved by 25× and 2×, respectively, demonstrating the benefit of improved structural quality. This chapter will discuss attempts at applying the enhancement techniques to the LaAs and GdAs material systems and issues encountered that hampered these RE-As systems. The discussion will then turn to two separate investigations that build on the results of each other and on the work in previous chapters. The first investigation used the ErAs materials system and explored the effect of tuning the superlattice period thickness on the carrier lifetime, which has been shown scale directly with period thickness [56,41]. The second investigation used the best ErAs superlattice geometry for beryllium counter doping experiments in an effort to to further improve the the photoconductive properties of the nanocomposite.

5.1 Growth Enhancements of LaAs:InGaAs and GdAs:InGaAs Superlattices

The LaAs and GdAs material systems were also considered for growth enhancement investigations as discussed in the previous chapter. However, there were several factors that impacted these investigations. Since LaAs does not form a single-phase rocksalt crystalline structure when deposited on InGaAs or GaAs [105] as other RE-As species examined, measuring its growth rate required use of cross-sectional TEM. Other techniques such as RHEED intensity oscillations and XRD require coherent films

to accurately measure growth rates and film thicknesses. Given that the LaAs growth rate was already low, 0.02 ML/s, when nanocomposites were grown for the investigation summarized in Chapter 3, a bismuth-mediated superlattice of LaAs (30 periods of 40 nm) with the same 2 second shutter timing sequence used in the LuAs study was grown under the same conditions described in the previous chapters. The resulting properties of the superlattices summarized in Table 5.1 did improve somewhat, however, the improvement was not sufficient to continue exploration of the LaAs system. The GdAs system, on the other hand, does grow coherent films and growth rates can be easily confirmed with XRD interference fringes of the film. RHEED intensity oscillations, however, did not yield repeatable results for calibrations. The growth rates of GdAs films were already limited to a maximum of 0.02 ML/s due to MBE system contraints on the maximum flux from the cell. The position of other source cells restricted the location of the gadolinium cell to an available downward looking port, which meant that the maximum temperature was limited to below the melting point of Gd, and thus a very low resulting flux. Superlattices with increasing deposition of GdAs were grown using the surfactant-mediated enhancement discussed in Chapter 4. Measurements of the resulting superlattices, however, revealed almost no improvements over the superlattices grown in Chapter 3. Flux vs. temperature measurements of the bismuth cell revealed that the bismuth flux had become unstable, likely due to a depleted charge. Although GdAs is a promising material for photomixer development, no further growths were attempted with the GdAs system due to the long delay time in obtaining and loading more bismuth source material.

Table 5.1: Properties of a 30-period LaAs:InGaAs superlattices with 40 nm period thickness grown at 490 °C. The properties summarized include bismuth use during InGaAs growth (Bi), total LaAs deposition (Dep), LaAs growth rate (GR), root-mean-squared surface roughness (RMS SR), room temperature mobility (μ), room temperature dark resistivity (ρ), room temperature carrier concentration (n), Fermi level based on room temperature carrier concentration using Nilsson equation [107], activation energy from temperature dependent Hall (E_a), and carrier lifetime (τ).

Bi	LaAs Dep. (ML)	LaAs GR (ML/s)	RMS SR (nm)	μ (cm^2/V-s)	ρ (Ω-cm)	n (cm^{-3})	E_F-CB (meV)	E_a (meV)	τ (ps)
No	0.3	0.02	8.18	1918	0.0879	3.7×10^{16}	-43.30	65.34	9.22
Yes	0.3	0.02	2.71	2238	0.2484	1.12×10^{16}	-74.98	96.70	7.45

5.2 Geometry Investigation of Enhanced ErAs:InGaAs Superlattices

This investigation explored the effect of different superlattice period thicknesses on the properties of ErAs:InGaAs superlattices. ErAs was chosen for this investigation as results of preliminary enhanced superlattices showed slightly improved properties compared to those of enhanced LuAs superlattices. All materials were grown under the same conditions described in earlier chapters using semi-insulating (100)-oriented InP substrates. The ErAs superlattices used surfactant-mediated growth for the InGaAs with the 2 second shutter timing sequence and an ErAs growth rate of 0.01 ML/s. In addition, all the materials grown had the same 1.2 μm superlattice thickness with a 150 nm InGaAs buffer region. Hence, 10 nm period thicknesses required 120 periods and 20 nm period thicknesses required 60 periods.

For the superlattices with 10 nm periods, the observed InGaAs (2×4) RHEED pattern would recover after different overgrowth thicknesses depending on the amount of ErAs deposited. Effective ErAs depositions of 0.2 ML recovered within 6 nm of overgrowth for every period during growth. The 0.4 ML depositions required almost 9 nm to recover a streaky RHEED pattern. The RHEED pattern for the 0.6 ML and 0.8 ML

depositions remained slightly blurred and never fully recovered a clear streaky pattern after the first few periods during sample growth. For the 20 nm period samples, the RHEED pattern was observed to fully recover within ~8 nm and ~12 nm of InGaAs overgrowth for depositions of 0.4 ML and 0.8 ML respectively throughout the growth. The 1.2 ML deposition required ~18 nm to fully recover the streaky RHEED pattern. The 1.6 ML deposition, however, never fully recovered streaky RHEED after the first period and the pattern remained slightly blurred throughout the growth. For samples with 40 nm periods, depositions up to 2.0 ML recovered the streaky RHEED pattern within 10 nm of overgrowth. Depositions of 2.4 ML, 2.8 ML, and 3.2 ML recovered a streaky pattern after 12 nm, 15 nm, and 25 nm respectively.

Symmetric ω-2θ XRD scans around the (004) diffraction peak of the InP substrate showed degraded superlattice peak fringes for the 0.6 ML and 0.8 ML depositions at 10 nm. Scans of the 20 nm period superlattices showed strong period fringes that widen slightly for the 1.6 ML deposition. Period fringes for the 40 nm superlattices remained strong for depositions up to 2.0 ML and began to widen only with higher depositions. Measurements using AFM, Figure 5.1, showed RMS surface roughness trends consistent with observations from RHEED and XRD scans. The 10 nm period superlattices began to degrade with depositions of 0.4 ML per period and higher. The 20 nm period superlattices degraded uniformly with higher ErAs depositions. The 40 nm period superlattices remained smooth for depositions up to 1.6 ML and began to slightly degrade for higher depositions.

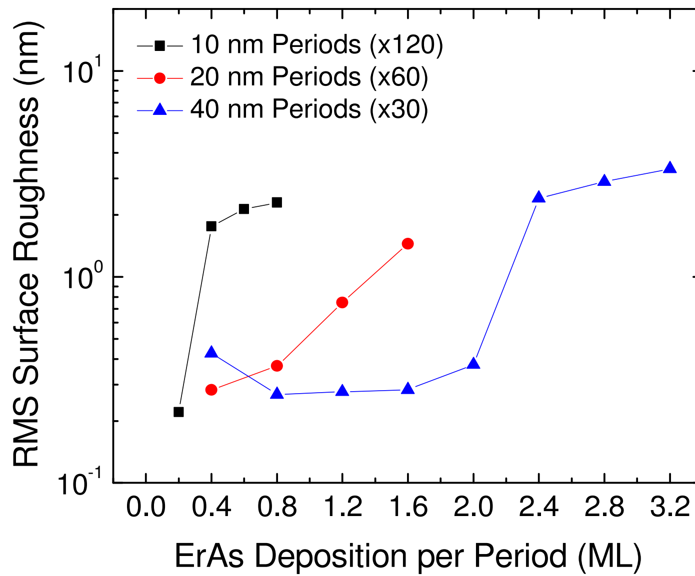

Figure 5.1: Root-mean-squared surface roughness AFM scans of superlattices with increasing ErAs deposition with different superlattice periods. Superlattices with larger periods delayed the degradation of the surface to higher ErAs depositions.

Room temperature Hall measurements indicated electrons as the majority carriers for all the superlattices in this investigation. Much like previous investigations, there is a general trend of increasing dark resistivity with increasing depositions of ErAs, as shown in Figure 5.2. It is interesting to note that the resistivities seem to be asymptoting toward different resistivity values that appears to depend on the period separation and at depositions where the structural quality of the material begins to degrade. Before reaching the apparent resistivity ceiling, however, the resistivity seems to depend only on the amount of ErAs deposition and not the period thickness of the superlattice geometry. This is evident particularly for the 0.4 ML and 0.8 ML ErAs depositions in the 20 nm and 40 nm period superlattices. The measured resistivities are practicaly identical even though the 20 nm period superlattice has twice as much ErAs per volume than the

equivalent 40 nm period superlattice. Although 0.2 ML depositions were not grown for the 20 nm and 40 nm period thicknesses, it appears that the resistivity trends back to a similar value for superlattices at all three period thicknesses. Superlattices with 40 nm spacings had the highest resistivities at ErAs per period depositions beyond 0.8 ML depositions, reaching a high of nearly 4.3 Ω-cm at 2.8 ML of ErAs deposition, a record for non-counterdoped RE-As nanocomposites

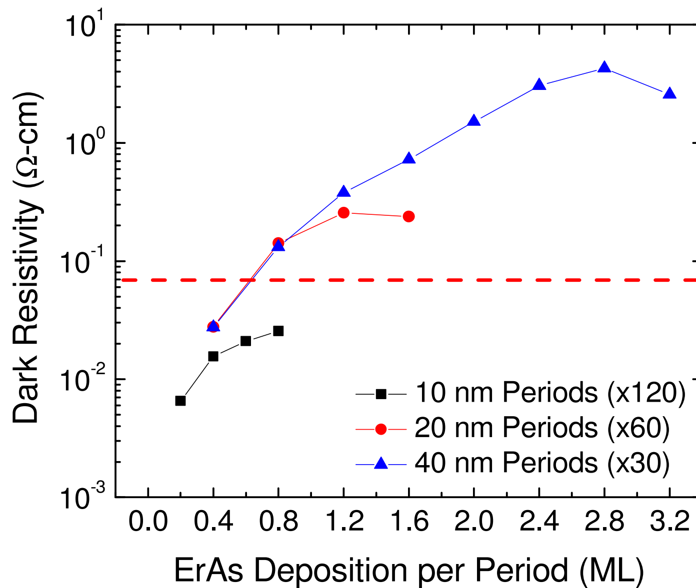

Figure 5.2: Room-temperature dark resistivity of superlattices as a function of ErAs deposition and different period thicknesses. The resistivities seem to level off at different values depending on the period thickness, with the 40 nm period reaching the highest resistivities. The dashed line represents the resistivity of epitaxial InGaAs.

Carrier mobilities, shown in Figure 5.3, demonstrated a general decreasing trend with higher ErAs deposition. This trend was dominant for the 10 nm and 20 nm period superlattices and the mobilities continued to degrade with increasing ErAs. However, the 40 nm period superlattices seem to level off and maintain mobilities over 4000 cm^2/V-s even for depositions up to 2.0 ML. Higher depositions of ErAs then begin degrading the

mobility. These observations are consistent with the surface roughness measurements from AFM scans where the surface quality of the overgrowth for the last period begins to degrade for superlattices with ErAs depositions of 2.4 ML and higher. This makes intuitive sense as the higher structural quality of the material means less scattering of the charges due to crystalline defects and therefore higher expected mobilities.

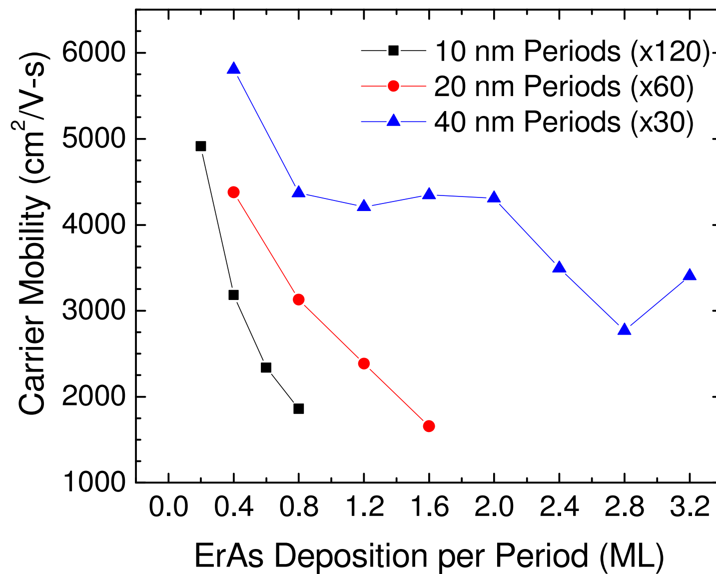

Figure 5.3: Room-temperature electron mobility as a function of ErAs deposition and different period thicknesses. The 10 nm and 20 nm periods showed decreasing mobilities with increasing deposition of ErAs. The mobilities for the 40 nm period leveled off at over 4000 cm^2/V-s for several depositions and decreased for ErAs depositions higher than 2.0 ML.

Activation energies calculated from temperature-dependent Hall measurements, shown in Figure 5.4, show a very similar trend to the resistivity measurements. The activation energies appear to level off and degrade past certain values for each of the period thicknesses. However, they remain nearly the same value for the different periods before the leveling effect comes into play. This makes intuitive sense when looking at the

balancing act of the nanoparticle morphology to the degradation of the matrix overgrowth. Previous studies suggest that different exposed crystalline planes of ErAs films demonstrate different Schottky barrier heights [142] and the idea that the Schottky barrier height for nanoparticles is a combination of the exposed surfaces has also been proposed [41,70]. So if the period thickness allows enough InGaAs growth to smooth out the growth front before the deposition of the nanoparticles, then a particular RE-As deposition will form certain sizes and nanoparticle morphologies where different crystalline planes are exposed to the host matrix. As the deposition of ErAs is increased, the nanoparticles become larger in size and more pancake-like, exposing more of the (100) plane, which has a higher Schottky barrier than other prominent planes such as the (011) [142,143,99,100]. For period thicknesses that do not allow enough overgrowth to smooth out the surface before deposition of the next set of ErAs nanoparticles, the exposed surface of the nanoparticles may no longer be dominated by the (100) planes but by other planes, which have much lower barrier heights [142]. In addition, the lower quality overgrowth can also lead to crystalline defects that create shallow and band tailing states, potentially lowering the effective barrier height to the nanoparticle. This general idea is evidenced by the nearly identical activation energies for the 0.4 ML and 0.8 ML depositions at 20 nm and 40 nm periods. The 1.2 ML deposition for the 20 nm period, on the other hand, showed signs of structural degradation, providing a potential explanation for why the activation energy might decrease. At 1.2 ML of ErAs deposition, the 40 nm superlattice periods still showed good structural quality and hence it is likely the reason why the activation energy continued to increase as more of the (100) plane of the ErAs is exposed to the matrix. The 40 nm superlattices achieved the highest activation energies, over 240 meV for the 2.4 ML and 2.8 ML ErAs depositions, nearly one-third of the way into the InGaAs bandgap.

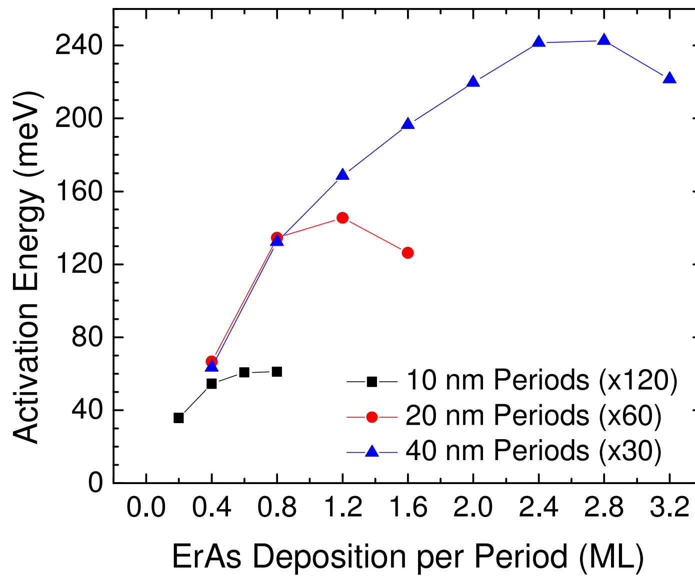

Figure 5.4: Activation energy of enhanced ErAs superlattices with increasing ErAs deposition and different period thicknesses. Superlattices with 40 nm periods had the highest activation energies.

Carrier lifetime measurements using differential pump-probe transmission, shown in Figure 5.5, have a general decreasing trend with increasing deposition of ErAs. The superlattices with the smaller periods had, in general, lower carrier lifetimes than the superlattices with the same ErAs deposition per period at larger periods. However, when the maximum amount of ErAs deposition per period is considered, the 40 nm period superlattices achieved the lowest carrier lifetimes. There is a slight increase in the measured carrier lifetime for the 3.2 ML deposition which is attributed to the degradation of the InGaAs overgrowth quality offsetting the larger ErAs deposition.

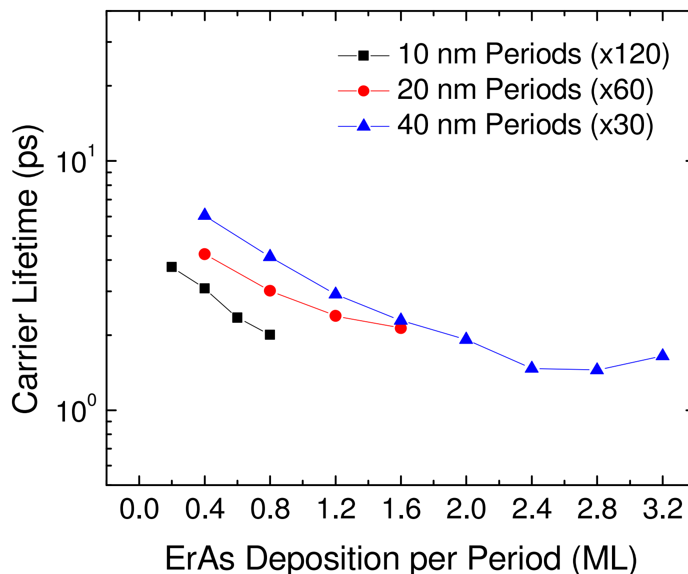

Figure 5.5: Carrier lifetime measurements using differential pump-probe transmission of superlattices with increasing deposition of ErAs and various period thicknesses. Shorter periods had lower lifetimes for the same deposition/period of ErAs, however, the 40 nm periods achieved the lowest overall lifetimes since more ErAs was deposited before the material degraded.

In this investigation we observed the effects of different superlattice periods on the properties of the nanocomposites. Future studies may find cause to see if the general trend of improved properties with increasing superlattice period thickness continues with periods of 60 nm and beyond. However, for the purposes of making photomixer materials, the material system appears to have reached its limit. The following section discusses the use of beryllium counterdoping with the goal of continuing to push the electrical and temporal characteristics of these materials. The growth enhancement techniques discovered in Chapter 4 and applied in this section might lower the amount of beryllium required to align the Fermi level closer to the midgap, meaning less carrier scattering due to point defects and a potentially higher mobility. Following Section 5.4,

Table 5.2 provides a summary of all the superlattices and measured properties for this investigation.

5.3 Beryllium Doping of Enhanced ErAs:InGaAs Superlattices

The improved structural quality of the superlattices due to the growth enhancement techniques developed in the previous investigations also coincidentally lowered the measured carrier concentrations of the materials by at least two orders of magnitude. As such, it was suspected that a much lower amount of beryllium counter doping would be required to align the Fermi level closer to the midgap of the InGaAs. In this investigation, ErAs superlattices with 2.0 ML depositions and 40 nm period thicknesses were used because of their high mobility (~4300 cm^2/V-s) and reasonably high resistivity (1.5 Ω-cm). The carrier lifetime (1.92 ps) was also not too high to preclude further examination of this geometry and ErAs deposition. The amount of deposited beryllium was varied from 1×10^{12} cm^{-3} to 1×10^{18} cm^{-3} as calibrated from Hall measurements of GaAs films at various doping concentrations. The doping profile used was continuous and present only during the InGaAs overgrowth so as to not affect the ErAs nanoparticle morphology. It is unknown at this time if high doping levels of beryllium deposited at the same time as the RE-As affect the nanoparticle morphology, as such no modulation or delta doping [41] was attempted for this investigation pending a thorough examination of the continuous doping profile first performed. Superlattice growth proceeded under same conditions as the investigations in the previous chapters on semi-insulating (100) InP substrates and included the 2 second shutter timing sequence for the surfactant-mediated growth. RHEED patterns recovered their streaky pattern within 10 nm of overgrowth as previously observed for the undoped superlattice and

seemed unaffected by the beryllium doping. This is expected since the flux of beryllium atoms is orders of magnitude lower than the flux of the III-V atoms. XRD measurements showed almost no difference between the superlattices for all doping levels. AFM scans revealed RMS surface roughnesses that did not degrade within increasing doping level, remaining within 0.62 nm for all the measured superlattices.

Room temperature Hall measurements showed almost no change in the dark resistivity, Figure 5.6, for doping levels up to 2×10^{15} cm^{-3} compared to an undoped superlattice with the same ErAs deposition. Doping levels of 1×10^{17} cm^{-3} increased the resistivity to almost 8 Ω-cm. However, a doping level of 1×10^{18} cm^{-3} was sufficient to turn the material p-type, consistent with previous investigations of continuous beryllium doping of ErAs:InGaAs superlattices [41]. It appears that a doping profile between these last two levels might yield an optimal resistivity and should be explored in future investigations. Unfortunately, no further growths were possible as the gallium charge in the source cell depleted preventing further growths.

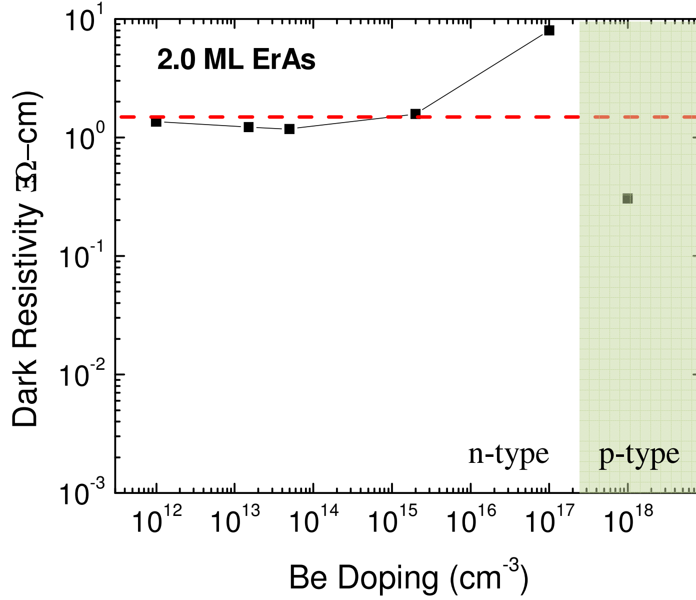

Figure 5.6: Room-temperature dark resistivity of enhanced 2.0 ML ErAs:InGaAs superlattices with increasing beryllium doping of the InGaAs host matrix. Doping levels of $1x10^{17}$ achieved the highest resistivity of 7.9 Ω-cm, while the doping level of $1x10^{18}$ pushed the material p-type. The dashed line represents the resistivity of an undoped enhanced 2.0 ML ErAs:InGaAs superlattice.

Carrier mobilities, shown in Figure 5.7, indicate a gradual decrease with increasing doping levels, which is expected as higher doping leads to more point defects that can scatter the carriers. However, even at a doping level of 1×10^{17} cm^{-3}, where the resistivity began to increase, the mobility was still over 3700 cm^2/V-s. This is promising for continued investigation of counter doping at the higher doping levels, since the mobility is nearly an order of magnitude higher than the beryllium doped ErAs:InGaAs superlattices previously investigated with the same resistivity [41] and can be directly attributed to the improved structural quality of the InGaAs due to the growth enhancement techniques. It is also important to note that although the 1×10^{18} cm^{-3} doping level turned the material p-type, the measured mobility of the holes was 670 cm^2/V-s.

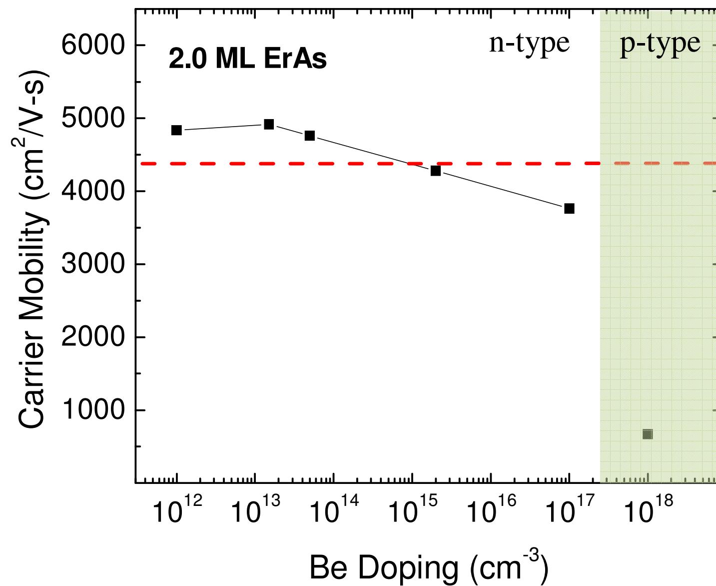

Figure 5.7: Room-temperature carrier mobility of enhanced 2.0 ML ErAs:InGaAs superlattices with increasing beryllium doping in the InGaAs. The dashed line represent the mobility of an undoped superlattice with the same ErAs deposition.

Carrier lifetime measurements using pump-probe transmission, Figure 5.8, showed nearly no change until doping reached 1×10^{17} cm^{-3}, when the lifetime dropped by 25%. The measured lifetime at the 1×10^{18} cm^{-3} doping level, on the other hand, decreased substantially down to 0.24 ps. This makes intuitive sense as the electrons in the n-type material have a short lifetime and decay into the trap states where they are essentially waiting for holes to become trapped. Since the hole lifetime is much longer than that of electrons, the recombination process is dominated by the hole lifetime. As the material becomes p-type, there is now a surplus of holes that can become trapped and the recombination process shifts to waiting for the electrons. Since the lifetime of the electrons is already short to begin with, the overall recombination process becomes very rapid. The important point to remember, however, is that the recombination process is

still maximized when the effective Fermi level position is near the midgap [94], so careful calibrations must be done when increasing the beryllium doping level to create a balance with the Fermi level position due to the nanoparticles.

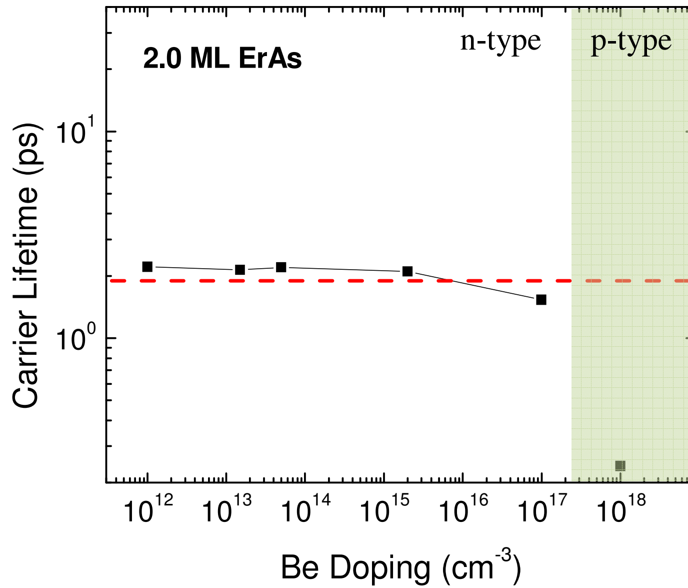

Figure 5.8: Carrier lifetime measurements using differential pump-probe transmission of enhanced 2.0 ML ErAs:InGaAs superlattices with increasing beryllium doping. Lifetimes do not seem to change significantly until the $1x10^{17}$ beryllium doping level when the lifetime drops to 1.53 ps. Further doping to $1x10^{18}$ with beryllium turned the material p-type and had the lowest measured lifetime of 0.24 ps.

5.4 Summary

This chapter investigated applying growth enhancement techniques first explored in Chapter 4 to the ErAs system, which showed superior unenhanced properties to those of LuAs. A LaAs-based superlattice also showed some improvement with surfactant-mediated growth but the improvements were not sufficient to continue pursuing this material system, while an attempt was made to improve the GdAs-based superlattices but

there was not enough bismuth source material to successfully continue that investigation. Superlattices with different period thicknesses were then explored using ErAs-based materials. It was found that superlattices with 40 nm periods yielded the best properties achieving the highest resistivities and mobilities, and the lowest carrier lifetimes. A 40 nm superlattice geometry with 2.0 ML ErAs deposition per period was chosen as the test candidate for beryllium counter doping experiments because it maintained mobilities over 4000 $cm^2/V\text{-}s$, while possessing a resistivity of 1.5 Ω-cm and a 1.92 ps carrier lifetime. The beryllium counter doping experiments showed promise for further exploration of the doping level between 1×10^{17} cm^{-3} and 1×10^{18} cm^{-3}. At the 1×10^{17} cm^{-3} doping level, resistivity was increased up to 8 Ω-cm with a modest decrease in the mobility to 3700 $cm^2/V\text{-}s$, and a carrier lifetime of 1.53 ps, while the material turned p-type at the 1×10^{18} cm^{-3} doping level. Further doping experiments were not possible as the gallium cell in the system depleted its source material.

The following chapter will discuss an attempt to push the Fermi level closer to the midgap without the use of beryllium counter doping by changing the composition of the host matrix. For convenience, a summary of the superlattices grown for the two investigations in this chapter are given in Table 5.2 and Table 5.3 with all the measured properties.

Table 5.2: Properties of bismuth-enhanced ErAs superlattices grown at 490 °C with an ErAs growth rate of 0.01 ML/s and various period geometries. The properties include: ErAs deposition (Dep), number of periods and thicknesses (L), root-mean-squared surface roughness (RMS SR), room temperature mobility (μ), room temperature dark resistivity (ρ), room temperature carrier concentration (n), Fermi level based on room temperature carrier concentration using Nilsson equation [107], activation energy from temperature dependent Hall (E_a), and carrier lifetime (τ).

Dep. (ML)	L (#/nm)	RMS SR (nm)	μ (cm^2/V-s)	ρ (Ω-cm)	n (cm^{-3})	E_F-CB (meV)	E_a (meV)	τ (ps)
0.4	30/40	0.43	5805	0.0274	3.92×10^{16}	-41.73	63.5	6.04
0.8	30/40	0.27	4367	0.1316	1.09×10^{16}	-75.83	132.5	4.12
1.2	30/40	0.28	4206	0.3799	3.91×10^{15}	-102.43	168.7	2.92
1.6	30/40	0.28	4345	0.7248	1.98×10^{15}	-120.04	196.5	2.29
2.0	30/40	0.38	4306	1.5074	9.61×10^{14}	-138.81	219.7	1.92
2.4	30/40	2.41	3492	3.0432	5.87×10^{14}	-151.59	241.5	1.46
2.8	30/40	2.90	2770	4.2788	5.27×10^{14}	-154.38	242.6	1.45
3.2	30/40	3.35	3405	2.5593	7.16×10^{14}	-146.44	221.5	1.65
0.4	60/20	0.28	4377	0.0276	5.16×10^{16}	-34.10	66.7	4.23
0.8	60/20	0.37	3128	0.1418	1.41×10^{16}	-69.05	134.5	3.01
1.2	60/20	0.75	2384	0.2566	1.02×10^{16}	-77.47	145.4	2.39
1.6	60/20	1.45	1657	0.2382	1.58×10^{16}	-66.01	126.2	2.13
0.2	120/10	0.22	4910	0.0066	1.94×10^{17}	6.49	61.0	3.75
0.4	120/10	1.76	3182	0.0155	1.26×10^{17}	-7.57	54.6	3.08
0.6	120/10	2.14	2337	0.0210	1.27×10^{17}	-7.36	60.8	2.35
0.8	120/10	2.30	1859	0.0255	1.32×10^{17}	-6.30	35.8	2.01

Table 5.3: Properties of bismuth-enhanced 2.0 ML ErAs superlattices grown at 490 °C with an ErAs growth rate of 0.01 ML/s, with 30 periods of 40 nm each, and increasing uniform beryllium counter doping. The properties include: beryllium doping level, root-mean-squared surface roughness (RMS SR), room temperature mobility (μ), room temperature dark resistivity (ρ), room temperature carrier concentration (n), measured carrier majority (n = electron, p = hole), Fermi level based on room temperature carrier concentration using Nilsson equation [107], carrier activation energy from temperature dependent Hall (E_a), and carrier lifetime (τ).

Be Doping	RMS SR (nm)	μ (cm^2/V-s)	ρ (Ω-cm)	n (cm^{-3})	Carrier Majority	E_F-CB (meV)	E_a (meV)	τ (ps)
1×10^{12}	0.36	4834	1.3623	9.48×10^{14}	n	-139.18	-	2.21
1.5×10^{13}	0.31	4914	1.2164	1.04×10^{15}	n	-136.65	-	2.14
5×10^{13}	0.39	4760	1.1735	1.12×10^{15}	n	-134.89	-	2.20
2×10^{15}	0.62	4277	1.5779	9.25×10^{14}	n	-139.81	-	2.10
1×10^{17}	0.57	3763	7.9813	2.08×10^{14}	n	-178.50	-	1.53
1×10^{18}	0.49	670	0.3139	2.96×10^{16}	p		-	0.24

Chapter 6: Rare-Earth Arsenide on InGaAsSb

The previous chapter investigated several other potential variables to use in conjunction with the enhancement techniques explored in Chapter 4. These variables included changing the RE-As species once again (ErAs and LaAs), changing the superlattice period spacing, and counter doping the material with beryllium. The enhanced superlattices with ErAs demonstrated the highest dark resistivities and activation energies of all RE-As species investigated. In addition, a decreasing superlattice period decreased the carrier lifetime as expected based on other investigations [41,53], however, the electrical properties suffered. Because a lower superlattice period has less InGaAs overgrowth to smooth the surface before another layer of RE-As is deposited, the structural quality of the matrix overgrowth was compromised leading to degraded mobilities and lower resistivities. On the other hand, larger periods had more space to recover the quality of the growth front and hence permit the most RE-As depositions and the highest dark resistivities. Although the addition of beryllium doping showed promise by increasing the dark resistivity, the lowered mobility may eventually prove counterproductive. An important observation of the enhanced superlattices was the saturation of the activation energy at the highest RE-As depositions. For high depositions, it is likely that the RE-As begins to take on more film like quality and behaviors, which depend on the matrix that is used. This chapter will investigate an alloy composed of $In_{0.53}Ga_{0.47}As$ and $GaAs_{0.5}Sb_{0.5}$ as the matrix for the superlattices. Both materials and the resulting alloy are lattice matched to InP. GaAsSb is a material that aligns with the Fermi level closer to its valence band and will be alloyed with InGaAs to tune the position of the Fermi level at the nanoparticle/matrix interface.

6.1 Fermi level Alignments

A mechanism for Schottky barrier formation and the existence of a Fermi stabilization energy level was proposed by Walukiewicz [144-147] to explain the correlation between Fermi level pinning deduced from Schottky barrier heights and the electrical properties of irradiated III-V semiconductors. Walukiewicz proposed that since the change in electrical properties of irradiated III-V materials were due to amphoteric native defects, that these same defects might play a crucial role in the processes that lead to a Schottky barrier. The model was applied to the metal-GaAs system using specific reactions induced by irradiation of the GaAs, leading to vacancy-interstitial pairs of defects in the lattice. The irradiation-induced defect reactions for n-type GaAs are

$$Ga_{Ga} + As_{As} \rightarrow V_{Ga} + Ga_i + As_{As}, \quad (6.1)$$

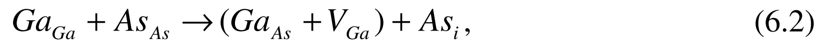

$$Ga_{Ga} + As_{As} \rightarrow (Ga_{As} + V_{Ga}) + As_i, \quad (6.2)$$

where the V_{Ga} and Ga_{As}+V_{Ga} are stable acceptor states. For p-type GaAs, the defect reactions induced by irradiation are

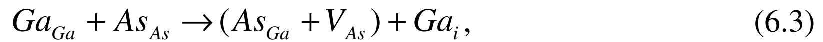

$$Ga_{Ga} + As_{As} \rightarrow (As_{Ga} + V_{As}) + Ga_i, \quad (6.3)$$

$$Ga_{Ga} + As_{As} \rightarrow V_{As} + As_i + Ga_{Ga}, \quad (6.4)$$

where the V_{As} and As_{Ga}+V_{As} are stable donor states. The defect reaction energy as a function of Fermi level position in the bandgap and the net transfer of charge from the lattice to the defect reactions are shown in Figure 6.1. The light blue region shows the Fermi level positions where the net transfer of charge is zero between the Ga and the As sublattice defect reactions. Hence the net effect on n-type or p-type materials after irradiation is a shift away from the band edges and towards the midgap at sufficiently high defect concentrations so that the Fermi energy reaches a stable position. According to the model, when a well-defined metal layer is formed on the surface of GaAs, a charge transfer between the metal and semiconductor occurs. For an n-type doped GaAs

material, if the metal work function is such that the Fermi level aligns near the valence band, then As_{Ga}+V_{As} or V_{As} donor states form to accommodate the excess charge and a short n-type-like depletion region is created near the interface. If the metal work function aligns closer to the conduction band, on the other hand, V_{Ga} or Ga_{As}+V_{Ga} acceptor states form to compensate for the charges and a p-type-like depletion region forms. These depletion regions are relatively short, on the order of a few tens of angstroms [144], and are in addition to the depletion region of the bulk doping of the GaAs, which then adjusts to the standard Schottky barrier formed once the charges at the interface have been balanced by the amphoteric defects. However, the short depletion regions due to the amphoteric defect compensation at the interface do not affect the electrical properties of the standard Schottky barrier height since the large concentration of defects facilitate tunneling to the metal through the thin barrier [144].

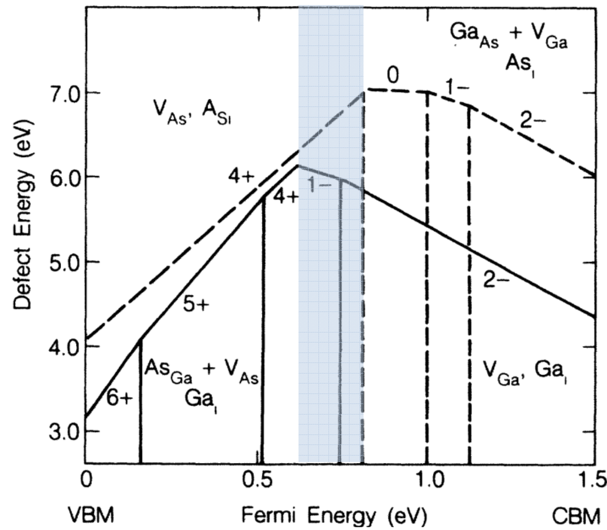

Figure 6.1: Defect reaction energy for the As (dashed line) and Ga sublattice (solid line) defects. Numbers represent the net charge transfer from the lattice due to the reaction. The Fermi level in light blue between E_V + 0.6 eV and E_V + 0.8 eV represents the balance in the reaction equations where there is a zero net transfer of charge (reprinted from [146]).

Although the reason for the Fermi level pinning at the Schottky barrier interface is controversial and Walukiewicz proposes only one of many potential models, vast amount of measurements do point to some stabilization mechanism in materials that prevents them from reaching extreme doping levels [147-153] and the insensitivity of the Schottky barrier heights to different metal work functions [144,154]. Regardless of the specific reason, there is evidence of a stabilizing force towards a particular energy level that is constant with respect to the band offset alignments of different materials and the vacuum level [147,148,155]. Figure 6.2 shows the suspected range for this Fermi stabilization energy.

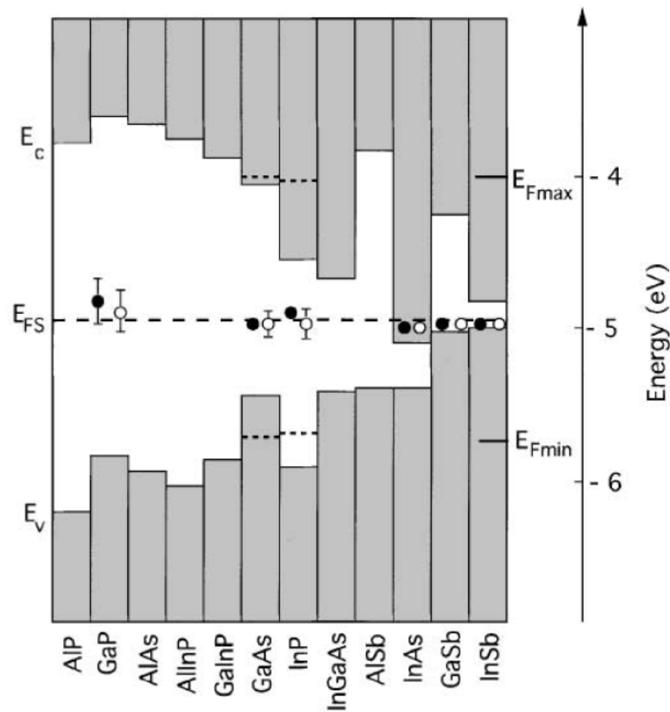

Figure 6.2: Band offsets and Fermi stabilization energy in III-V semiconductors. Energy is given relative to the vacuum level. Open circles represent the Fermi level at metal/semiconductor interfaces. Closed circles represent Fermi levels due to heavily irradiated and damaged materials. The dashed lines represent the highest doping levels achieved for GaAs and InP (reprinted from [147]).

When placing the band alignments of several III-V materials together along with previous measurements of the RE and group-V (RE-V) systems, we see very similar trend as the one described above. Figure 6.3 shows the band alignments of different materials as well the Schottky barrier heights of a film of ErAs on GaAs [142], a film of LuAs on GaAs performed by our group, and the Schottky barrier heights measured from Schottky diodes in an alloy matrix of InGaAs and InAlAs grown on InP [156]. The variation in the Schottky barrier height for the InGaAlAs alloy as it varied from InGaAs to InAlAs is evidence of the tunability of the Fermi level alignment at the RE-As/matrix interface. The activation energy measured from the enhanced LuAs and ErAs superlattices on InGaAs investigated in Chapter 4 and Chapter 5 are also shown in Figure 6.3. The Fermi level position based on room temperature calculations of the carrier concentration are shown for ErSb nanoparticles on GaSb and ErAs and ErSb nanoparticles on GaAsSb [41,70]. It should be noted that the nanoparticle growth on GaAsSb can not definitively be said to be either ErAs or ErSb. The growth conditions described indicate that the nanoparticles are at best As rich ErAsSb and Sb rich ErAsSb due to the shuttering of the group-Vs during growth. This is an important issue when considering growth of RE-V nanoparticles in a mixed group-V matrix. The reason, as we have noted from the investigations in the previous chapters in this dissertation, is that the nanoparticle/matrix interface is crucial for determining the properties of the nanocomposite. If attempting to grow either ErAs or ErSb by closing the Sb or As shutters respectively, then the surface of the exposed III-V material will begin to desorb the missing group-V in favor of the group-V with the impinging flux. As such, any attempt to grow these mixed group-V materials should maintain both group-V shutters open throughout the nanocomposite layer growth.

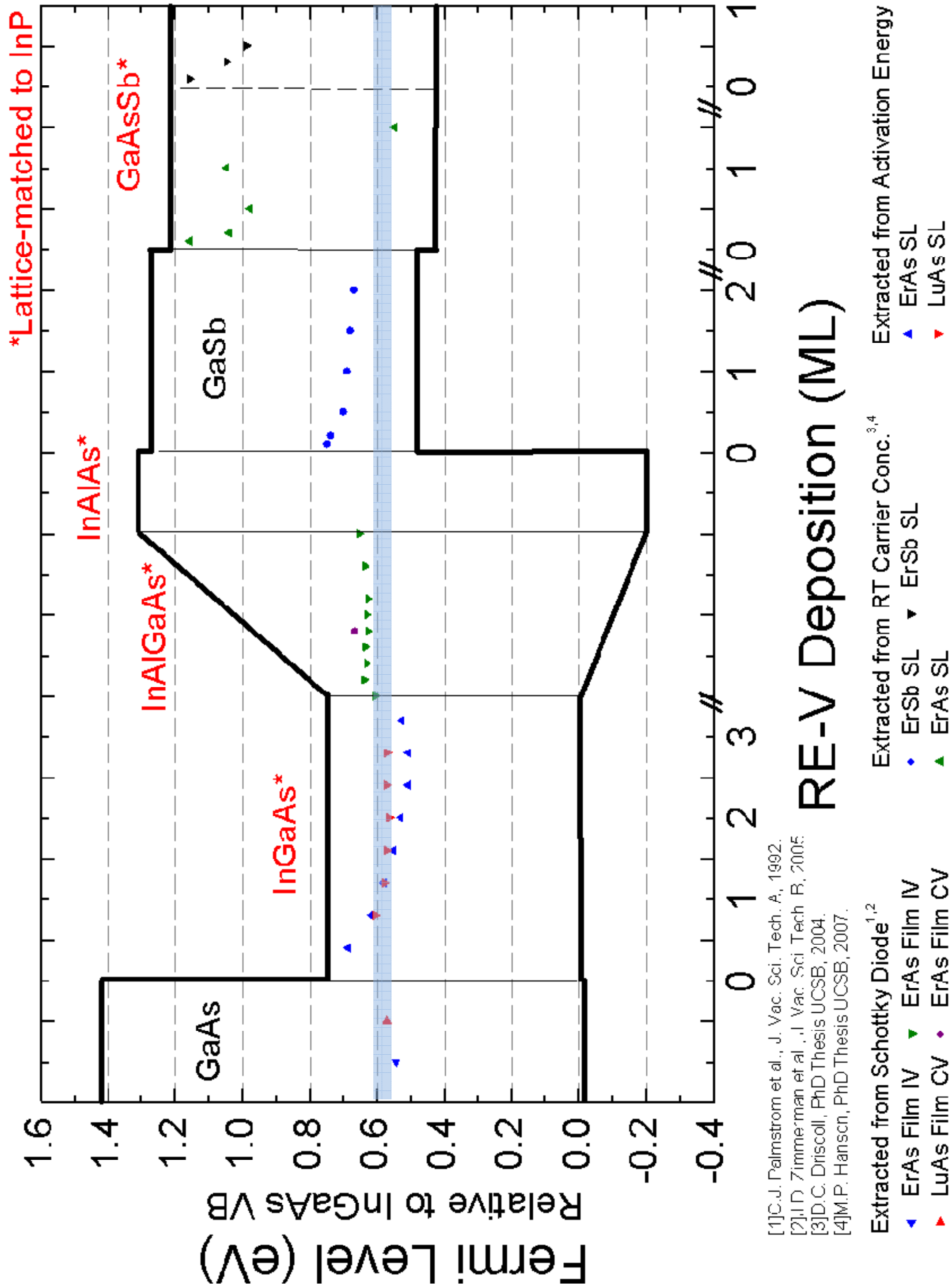

Figure 6.3: Band alignments of various III-V materials and different Fermi level alignments extracted from Schottky diodes, RT carrier concentrations calculations, and activation energies. The light blue line represents the Fermi stabilization energy.

The band alignment of the alloy that will be grown for this investigation is shown in Figure 6.4. The resulting alloy composition should approximately align the Fermi level near the midgap at the nanoparticle/matrix interface.

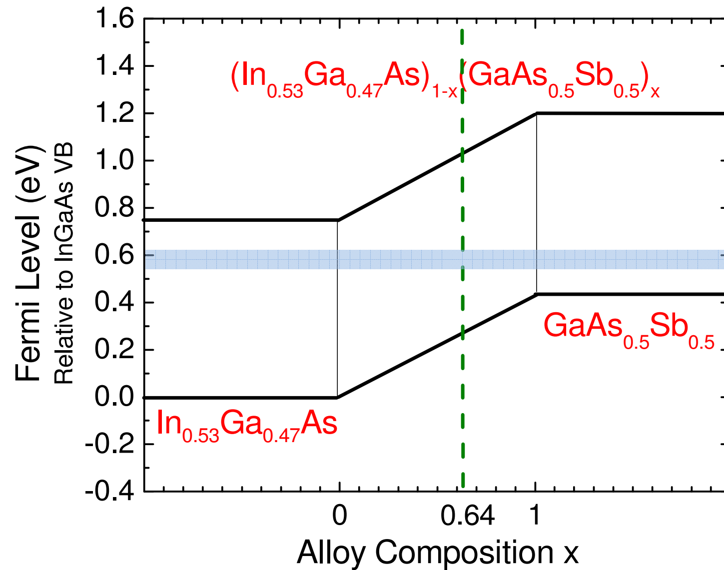

Figure 6.4: Band alignments of InGaAs, GaAsSb, and the resulting InGaAsSb quaternary alloy showing the shifting of the band alignments with respect to the Fermi stabilization energy level. All materials are lattice-matched to InP.

6.2 Growth and Structure of InGaAs and GaAsSb Alloys

Since this quaternary material lies in a miscibility gap [157,158], several test samples were attempted to determine the best growth conditions. Since previous experiments showed that InGaAs grew best between 470 °C and 500°C, these substrate temperatures were also used to grow the quaternary alloy and 470 °C resulted in the best material quality. It was discovered, however, that the alloy was very sensitive to temperature fluctuations. Changes in the substrate temperature of greater than 10 °C after

the fluxes were calibrated would result in very rough and poor crystalline quality material, so maintaining a stable substrate temperature through the duration of the growth became crucial. The quaternary alloy was grown with an As_2/Sb_2 BEP ratio of ~5.8 and a Ga/In BEP ratio of ~2.9 and these ratios were carefully calibrated to maintain the lattice matching condition. A bismuth BEP of 1×10^{-7} Torr was used during the growth of the InGaAsSb using the same 2 second shutter timing sequence described in the previous chapters. The As_2 and Sb_2 fluxes were maintained throughout the duration of the superlattice growth and as such it can not be fully determined whether the nanoparticles are bonded to As or Sb. However, it is suspected that the majority of the Er is bonded to As since enthalpies of formation are 3 times higher for As than for Sb. A proof of concept film of surfactant-mediated $In_{0.19}Ga_{0.81}As_{0.68}Sb_{0.32}$ was grown and tested to check the absorbance band edge, Figure 6.5, and found to be strongly absorbing at 1550 nm.

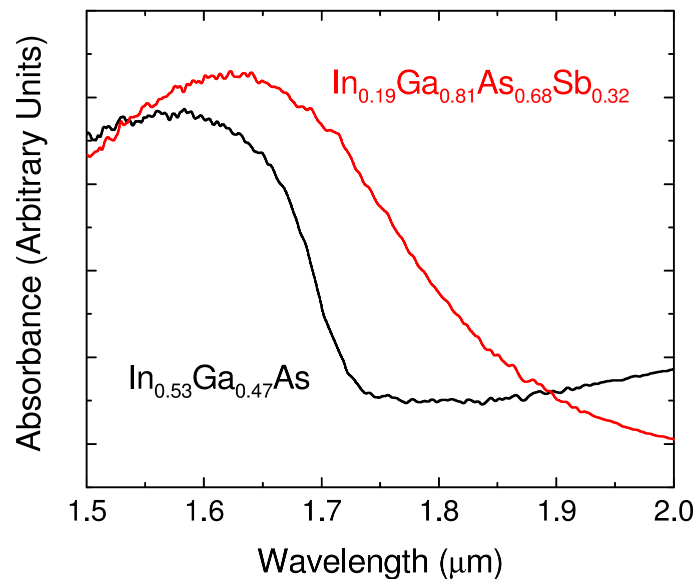

Figure 6.5: Measurement of the absorbance edge, using FTIR spectroscopy, showing the quaternary alloy is still strongly absorbing at 1550 nm.

Superlattices of ErAs(Sb):InGaAsSb were grown with the same alloy composition as the proof of concept matrix, an ErAs(Sb) growth rate of 0.01 MLs/, and with 1.2 ML, 1.6 ML, and 2.0 ML effective depositions of ErAs(Sb). The superlattices had 30 periods of 40 nm and were similar to previously investigated geometries. The observed RHEED pattern for the quaternary material remained slightly blurry and was never as clear as when growing InGaAs. The pattern did, however, chevron during the deposition of ErAs(Sb) and would recover to the same slight blurry pattern after about 20 nm of growth for all depositions of ErAs(Sb). Symmetric ω-2θ XRD scans around the (004) diffraction peak of the InP, Figure 6.6, showed strong period fringes that were slightly wider than those observed for InGaAs based superlattices, but were nonetheless indicative of well defined period interfaces. A reciprocal space map, shown in Figure 6.7, of the 2.0 ML ErAs(Sb) superlattice measured around the (224) diffraction peak of InP showed little deviation from the vertical position of the period fringes indicating coherently strained high quality epilayers. These observations were consistent with RMS surface roughness scans as measured by AFM which indicated roughnesses of less than 0.5 nm for all three superlattices. Superlattices with even higher depositions of ErAs(Sb) and different superlattice periods were scheduled for this material system, unfortunately, no further growths were possible as the Sb sublimator depleted its source material shortly after these growths were performed and the MBE system entered a maintenance cycle.

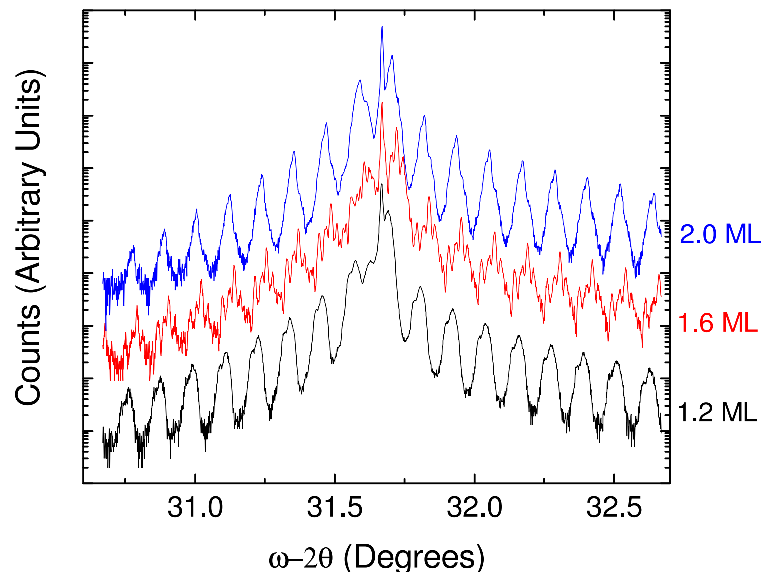

Figure 6.6: X-ray diffraction symmetric *ω-2θ* scans around the (004) diffraction peak of InP for superlattices with increasing depositions of ErAs(Sb) in InGaAsSb. All materials show very strong period fringes which are related to well-defined period interfaces. The materials show a slight lattice mismatch of the matrix to the InP substrate.

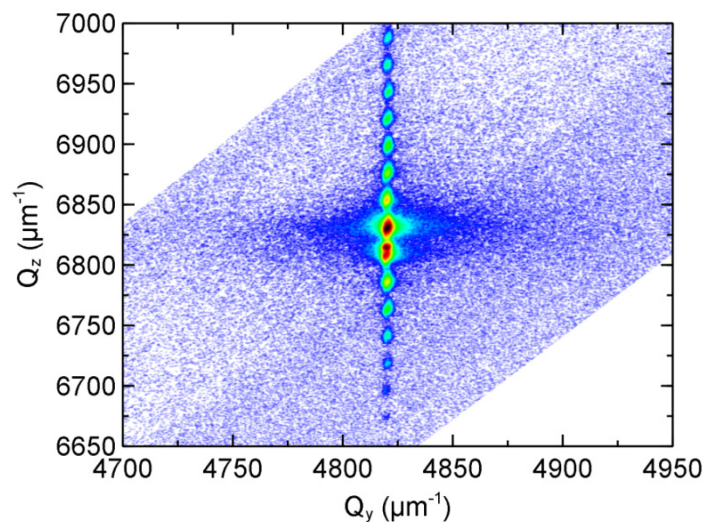

Figure 6.7: X-ray diffraction reciprocal space map around the (224) diffraction peak of InP for a 2.0 ML ErAs(Sb):InGaAsSb superlattice. The non-deviating vertical position of the period fringes show a coherently strained material.

6.3 Electrical Properties of InGaAsSb Based Superlattices

Room-temperature Hall measurements of the quaternary structures indicated n-type material for all superlattices. Dark resistivity measurements, Figure 6.8, for the InGaAsSb based superlattices show them to be slightly lower than the InGaAs based superlattices. This was unexpected, since a Fermi level alignment closer to the midgap should mean more efficient charge recombination at the nanoparticles sites and a reduced conductivity. A potential reason for the reduction in resistivity could be due to band tailing states at the edges of the bands due to irregularities in the period interfaces exposing different nanoparticle surfaces to the matrix besides the dominant (100) plane, which are known to vary in Schottky barrier heights [142]. The slight widening observed in the period fringes of the symmetric ω-2θ scans might be evidence of these irregularities. An investigation using cross-section TEM should elucidate this hypothesis.

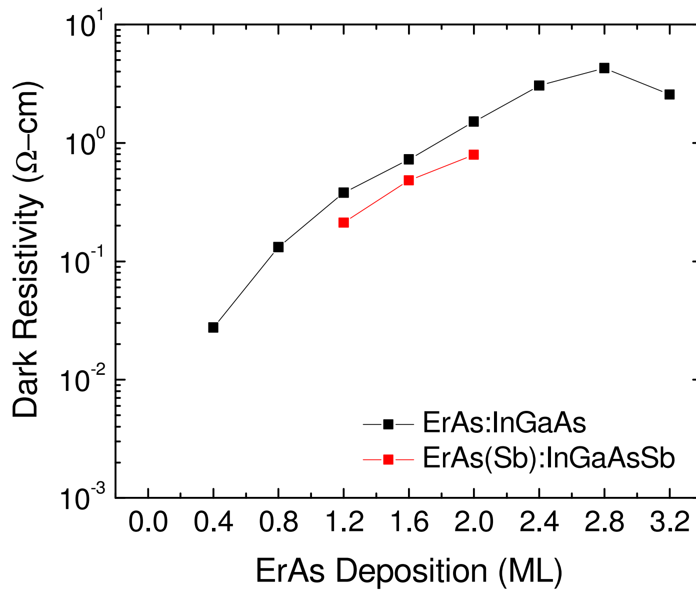

Figure 6.8: Room-temperature dark resistivity of ErAs(Sb):InGaAsSb superlattices with increasing ErAs(Sb) deposition, compared with the enhanced ErAs:InGaAs superlattices from Chapter 5.

Carrier mobilities, shown in Figure 6.9, indicate mobilities over 4000 cm^2/V-s for the 1.6 ML and 2.0 ML depositions of ErAs(Sb). These are also slightly lower than the InGaAs based superlattices but are fairly high nonetheless. It should interesting to see whether the trend will follow the InGaAs-based materials and degrade with increasing deposition of ErAs(Sb).

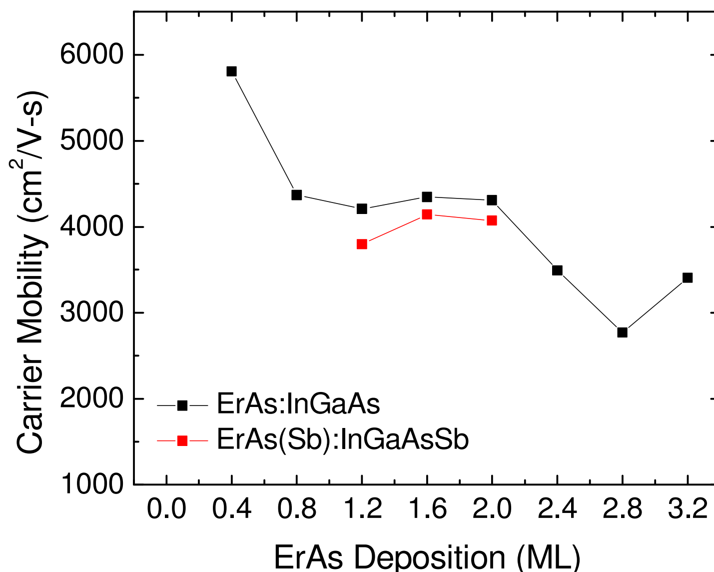

Figure 6.9: Room temperature electron mobility of ErAs(Sb):InGaAsSb superlattices with increasing deposition of ErAs(Sb) compared to the enhanced ErAs:InGaAs superlattices from Chapter 5. The ErAs(Sb) superlattices maintained high mobilities even with depositions of 2.0 ML.

Activation energies, Figure 6.10, extracted from temperature-dependent Hall measurements do not appear to be as high as expected and in fact are actually lower and appear to level off around 180 meV. This could be due to the irregularities in the period interfaces exposing other planes besides the (100) plane of the nanoparticles. Further investigations with different period thicknesses are necessary to elucidate the position of the Fermi level alignment for the nanoparticle/matrix interface.

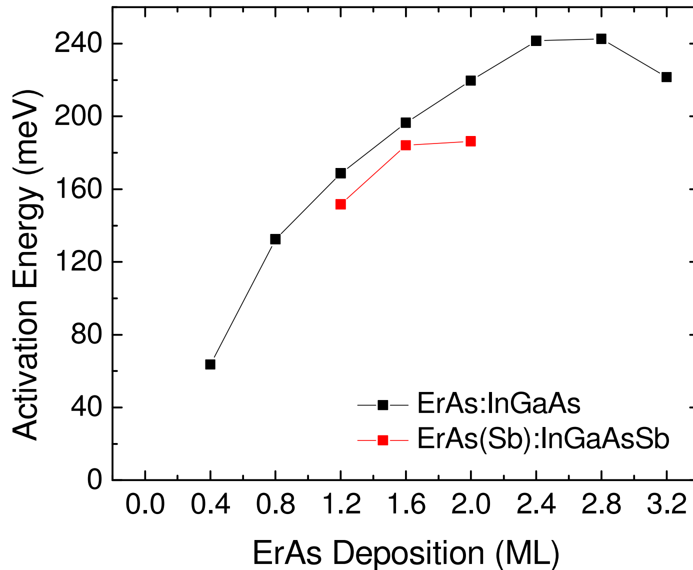

Figure 6.10: Activation energy of ErAs(Sb):InGaAsSb and enhanced ErAs:InGaAs superlattices with increasing ErAs(Sb) deposition. The activation energy of the quaternary superlattices appears to be leveling off at around 186 meV.

6.4 Carrier Lifetimes of InGaAsSb Based Superlattices

Carrier lifetime measurements using pump-probe transmission at 1550 nm, shown in Figure 6.11, indicate a more than 2× improvement in the carrier lifetimes for the InGaAsSb superlattices, achieving a record lifetime of 0.73 ps for the 2.0 ML ErAs(Sb) deposition superlattice. This is the lowest reported lifetime for a 1550 nm material system without using any counter doping. Further investigation of this material system should be performed because if the trend follows the InGaAs based materials even slightly, the decrease in the lifetimes while maintaining the high mobility should prove beneficial for photomixer applications.

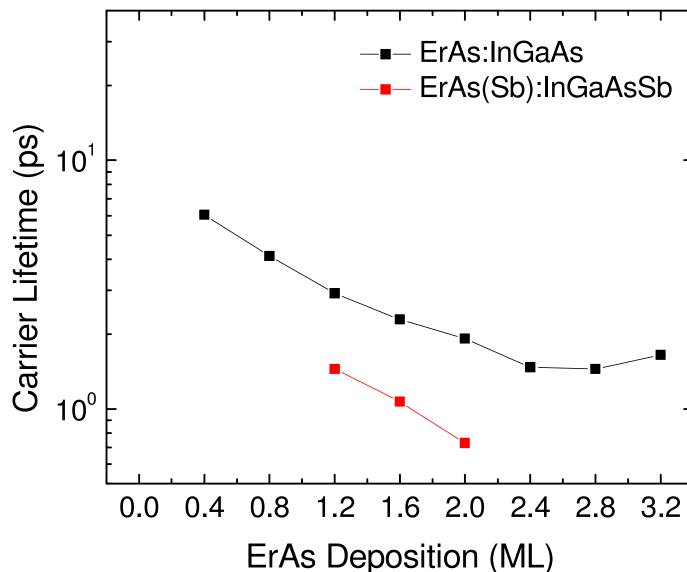

Figure 6.11: Carrier lifetime measurements using differential pump-probe transmission of ErAs(Sb):InGaAsSb superlattices and compared with enhanced ErAs:InGaAs superlattices with increasing ErAs(Sb) deposition. The quaternary superlattices achieved on average 2× lower lifetimes than the InGaAs based superlattices.

6.5 Summary

This chapter investigated the potential use of an InGaAs and GaAsSb alloy, lattice matched to InP, to tailor the alignment of the Fermi level at the nanoparticle/matrix interface towards the midgap of the material. The superlattice structures were complicated to grow and calibrate due to the miscibility gap of the InGaAsSb quaternary material. The resulting nanocomposites showed good structural quality with smooth surfaces and coherently strained epilayers with some slight period interface modulations, evidenced by the widening period fringes from XRD scans. A summary of the measured properties of the InGaAsSb material and the superlattices based on it is given in Table 6.1. Dark resistivities were modest at ~0.8 Ω-cm, but mobilities remained high for all

three superlattices investigated, over 4000 cm^2/V-s for the 2.0 ML deposition of ErAs(Sb). The carrier lifetimes showed the biggest improvement, more than 2× lower than a comparable ErAs:InGaAs superlattice, achieving a lifetime of 0.73 ps, the lowest lifetime of any 1550 nm material without the use of a counter dopant. With further improvements and optimizations, this quaternary alloy is a very promising candidate material for 1550 nm photoconductive materials.

Table 6.1: Properties of bismuth enhanced ErAs(Sb) superlattices grown at 470 °C with an ErAs(Sb) growth rate of 0.01 ML/s in an $In_{0.19}Ga_{0.81}As_{0.68}Sb_{0.32}$ matrix, with 30 periods of 40 nm each, and increasing ErAs(Sb) deposition. The properties include: ErAs deposition (Dep), root-mean-squared surface roughness (RMS SR), room temperature mobility (μ), room temperature dark resistivity (ρ), room temperature carrier concentration (n), carrier activation energy from temperature dependent Hall (E_a), and carrier lifetime (τ).

Dep. (ML)	RMS SR (nm)	μ (cm^2/ V-s)	ρ (Ω-cm)	n (cm^{-3})	E_a (meV)	τ (ps)
0	0.29	5043.72	0.4968	2.49×10^{15}	-	-
1.2	0.31	3795.79	0.2119	7.76×10^{15}	151.70	1.45
1.6	0.34	4142.22	0.4819	3.13×10^{15}	184.00	1.07
2.0	0.50	4070.28	0.7931	1.93×10^{15}	186.20	0.73

Chapter 7: Material Comparison and Device Calculations

All of the previous chapters have dealt with specific properties of the photoconductive materials, i.e. dark resistivity, mobility, and carrier lifetime, and the steps taken to improve them through growth enhancements, optimizations, and compositional alloys of different matrices. However, these properties still need to be put into context to see how each of them can affect the output power of photomixers based on these materials and where compromises can be made to sacrifice a particular property for another in the hopes of maximizing device performance. This chapter will address this need by utilizing the device model developed in Chapter 1.

7.1 Conventional Photomixer Devices

For a conventional photomixer device as described in Chapter 1, the calculated maximum input power based on thermal limitations is given by Equation 1.22,

$$P'_{\max} = \frac{\dfrac{\Delta T_{\max}}{\theta} - \dfrac{E^2 L^2}{\rho K}}{A\eta_{opt}\sqrt{\dfrac{3}{2}}\left[1 + \dfrac{\mu_e \tau_e}{\left(1 + \mu_e E / v_{e,sat}\right)} E^2 \left(\dfrac{e}{h\nu}\right)\right]} . \qquad (1.22)$$

This equation sets the power limit of the input pump lasers incident on the device. It is clear that ohmic heating due to the dark current takes away from the thermal budget of the device and why the biasing electric field needs to be optimized for different material systems. Every material will have different properties and a different optimal electric field that will yield the maximum output THz power. For this theoretical analysis, the key assumptions made about the device geometry and material properties are as follows: the thermal budget $\Delta T_{max}/\theta$ is 24 mW as set by finite element analysis simulations for

InGaAs on InP (described in Section 1.4); the thickness of the InGaAs is set to 1.35 μm; velocity saturation for InGaAs is set to 1.3×10^{5} m/s [39]; the effective resistance geometry value K is set to 296 cm^{-1} (described in Section 1.4); the effective optical absorption is set to ~1; the index of refraction for InGaAs is set to 3.43 at 1550 nm; the length between electrodes is set to 1 μm with an electrode width of 0.25 μm; the electric field lines are assumed to be semicircular between the corners of the electrodes such that the maximum path taken by the photogenerated charges is 1.57 μm; the electrode capacitance is 2.8 fF and the antenna impedance is 72 Ω, which are typical values [34].

Using the assumptions described above, the maximum input laser power can be plotted as a function of the biasing electric field between electrodes. Figure 7.1 shows the input power for the enhanced 2.0 ML ErAs:InGaAs with Be doping of 1×10^{17} cm^{-3} investigated in Chapter 5 and the 1.75 ML ErAs:InGaAs modulation Be doping superlattice grown by Driscoll [41,73]. The properties are included in Table 7.1 for convenience. The plot shows that the maximum input laser power begins to drop off for a much lower biasing electric field for the 2.0 ML ErAs material than for the 1.75 ML ErAs materials. This makes intuitive sense since the dark resistivity of the 1.75 ML ErAs material is much higher and can be biased with a larger electric field before the thermal budget is exceeded. However, the increase in resistivity came at the cost of the carrier mobility as seen in Table 7.1. This trade off then affects the material's β as defined in Equation 1.16 to be the frequency dependent external quantum efficiency,

$$\beta(\omega, E) \approx \frac{(1-e^{-\alpha d})\,\eta_{opt}\,\mu_e \tau_e}{\left(1+\mu_e E / v_{e,sat}\right)\sqrt{1+\omega^2\tau_e^2}}\,\frac{E}{L} = \frac{\eta_{e,electron}}{\sqrt{1+\omega^2\tau_e^2}}\,. \qquad (1.16)$$

This figure of merit describes the frequency dependent THz current gain of the device due to the input laser power and biasing electric field.

Table 7.1: Properties of the materials to be compared in this theoretical analysis.

	ErAs Dep (ML)	Be Doping (cm^{-3})	Doping type	μ (cm^2/V-s)	ρ (Ω-cm)	τ (ps)
Chapter 5	2.0	1×10^{17}	Continuous	3763	7.98	1.53
Driscoll et al. [41,73]	1.75	1×10^{20}	Modulation	211	70	1.0

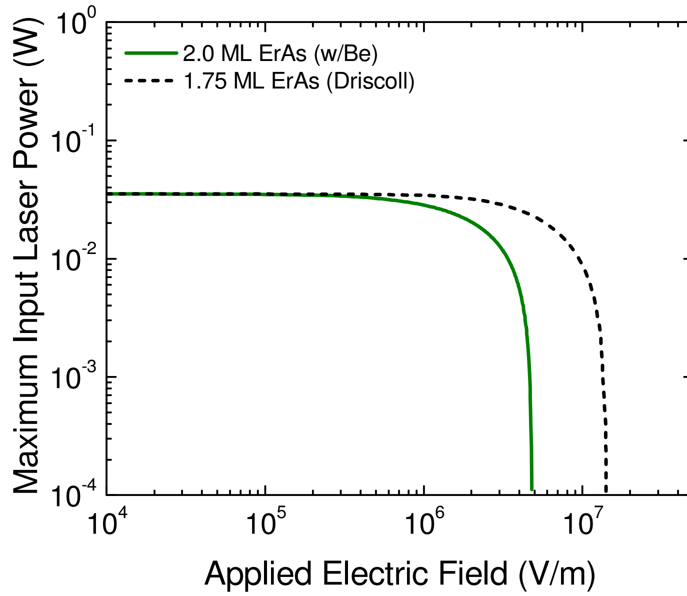

Figure 7.1: Maximum incident laser power calculated for an enhanced 2.0 ML ErAs:InGaAs with Be doping of 1×10^{17} cm^{-3} investigated in Chapter 5 and a 1.75 ML ErAs:InGaAs modulation Be doping superlattice grown by Driscoll [41,73].

The frequency dependent gain or β for both of these materials is plotted in Figure 7.2 for both materials and with a bias electric field increasing from 1×10^5 V/m to 5×10^6 V/m. It is clear the higher mobility has a definite effect on the β as can be seen from inspection of the definition. But the overall effect of the increase in the maximum input power and decrease in the gain can only be made clear when we look at the THz output power.

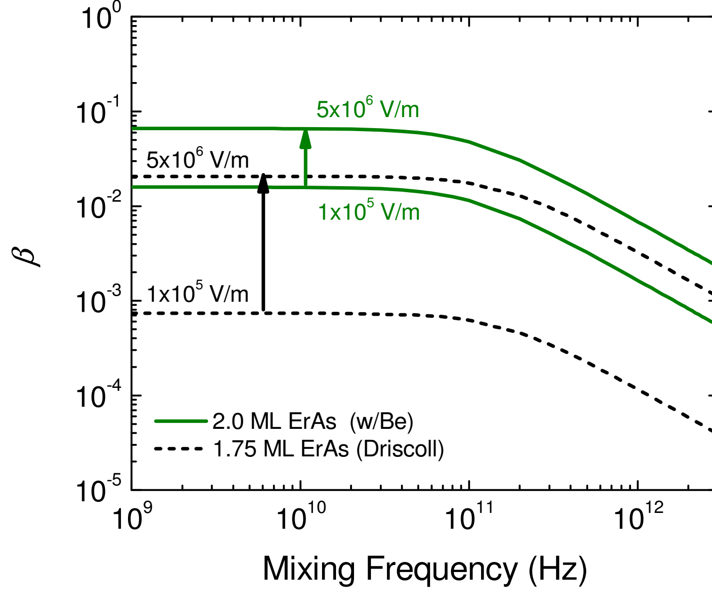

Figure 7.2: Figure of merit β as a function of the mixing frequency for an enhanced 2.0 ML ErAs:InGaAs with Be doping of 1×10^{17} cm^{-3} investigated in Chapter 5 and a 1.75 ML ErAs:InGaAs modulation Be doping superlattice grown by Driscoll [41,73] as the electric field intensity of increased from1×10^{5} V/m to 5×10^{6} V/m.

The maximum THz output power is given by Equation 1.27 and uses the maximum input power, which was set by the thermal budget,

$$P_{THz,out}^{\max}=\left[\frac{\frac{\sqrt{2/3}\,\mu_e\tau_e}{\left(1+\mu_e E/v_{e,sat}\right)}\frac{E}{L}\left(\frac{e}{h\nu}\right)\left(\frac{\Delta T_{\max}}{\theta}-\frac{E^2L^2}{\rho K}\right)}{\left[1+\frac{\mu_e\tau_e}{\left(1+\mu_e E/v_{e,sat}\right)}E^2\left(\frac{e}{h\nu}\right)\right]}\right]^2\frac{\eta_{ant}R_A}{2\left(1+\omega^2\tau_e^2\right)\left(1+\left(\omega R_A C_{elect}\right)^2\right)}.\quad(1.27)$$

Figure 7.3 shows the calculated maximum output power as a function of electric field intensity for a mixing frequency of 1 THz, which indicates an electric field range for optimal device performance. This plot is important to note because even though the resistivity of the material is an order of magnitude higher for the 1.75 ML ErAs:InGaAs material from Driscoll, the overall output power for the device using the material

described in Chapter 5 is 5× higher at 1 THz. This makes sense since the higher mobility contributes approximately squared proportional to the output power. However, the output power is still limited by the thermal budget from the optical heating even if the resistivity were taken to the infinite limit such that there is no contribution due to ohmic heating from the dark current. In essence, the mobility seems to be more important to the overall output power than the resistivity.

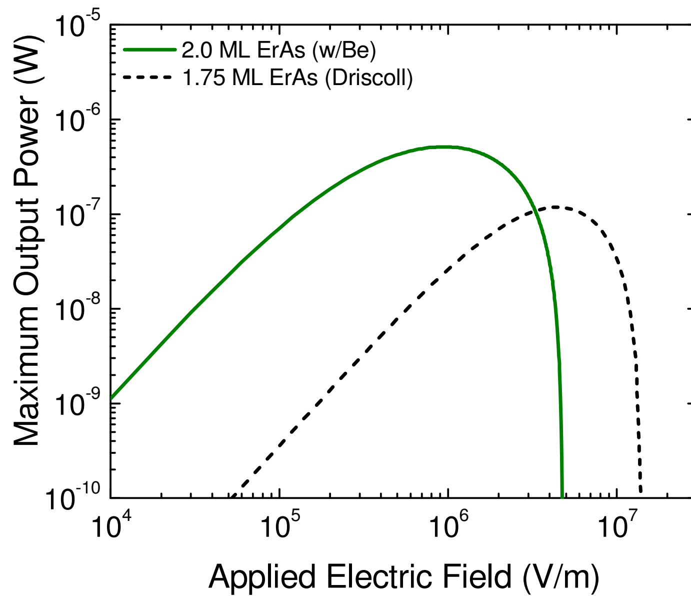

Figure 7.3: Maximum calculated output power versus biasing electric field for a 1 THz mixing frequency of photomixer devices using the 2.0 ML ErAs:InGaAs from Chapter 5 and the 1.75 ML ErAs:InGaAs from Driscoll [41,73].

The calculated output power as a function of the mixing frequency for the optimal biasing electric field for each material is shown in Figure 7.4, for the 2.0 ML ErAs:InGaAs material from Chapter 5 and the 1.75 ML ErAs:InGaAs material from Driscoll [41]. In addition the plot also shows the performance of an actual device fabricated using the Driscoll material and measured with a Golay cell by Sukhotin et al.

[73]. The plot shows over an order of magnitude deviation in the measured device to the calculated output power. Several factors could potentially account for this difference, including temperature dependence of the mobility and carrier lifetime, non-uniformity in the absorption profile between electrodes, irregular fringing electric fields at the electrode corners, as well as coupling efficiency to the silicon lens, etc. all of which were not accounted for in the model derived in Chapter 1.

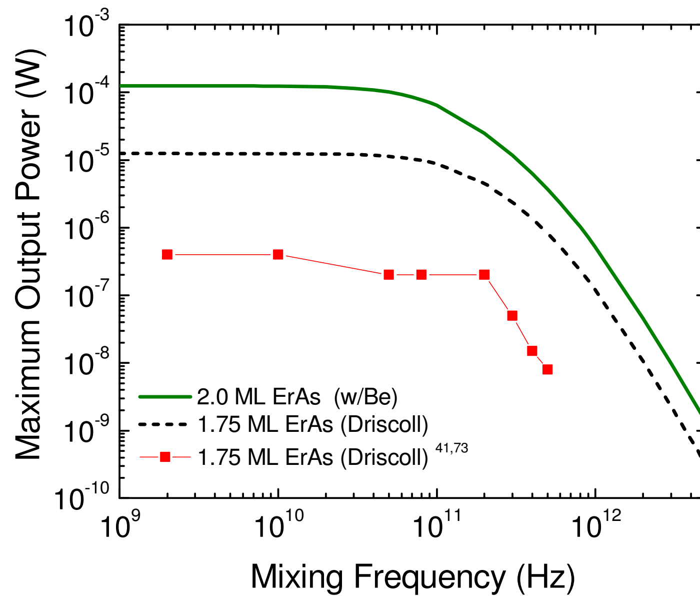

Figure 7.4: Calculated output power versus mixing frequency of photomixer devices using the 2.0 ML ErAs:InGaAs from Chapter 5 and the 1.75 ML ErAs:InGaAs from Driscoll [41,73]. The red dots indicate a device fabricated using Driscoll's 1.75 ML ErAs:InGaAs material and tested by Sukhotin [73].

Table 7.2 includes a summary of the properties for several materials from literature used in the simulated model assuming the same geometries and device impedances. The maximum output powers as a function of applied electric field for these materials are calculated and plotted in Figure 7.5 for 1 THz mixing frequency.

Table 7.2: Properties of the best materials grown during all of these investigations and materials from other sources for comparison in theoretical analysis.

	Material System	ErAs Dep (ML)	Be Doping (cm^{-3})	Doping type	μ (cm^2/V-s)	ρ (Ω-cm)	τ (ps)
Chapter 6	InGaAsSb	2.0	-	-	4070	0.79	0.73
Chapter 5	InGaAs	2.0	-	-	4306	1.5074	1.92
Chapter 5	InGaAs	2.4	-	-	3492	3.0432	1.46
Chapter 5	pInGaAs	2.0	1×10^{17}	Continuous	3763	7.98	1.53
Driscoll [41,73]	InGaAs	1.75	1×10^{20}	Modulation	211	70	1.0
Driscoll [41]	InGaAs	0.8	1×10^{20}	Delta	906	16.8	0.4
Dietz [68,69]	LT-pInGaAs	-	-	Continuous	500	240	0.55
Dietz [68,69]	InGaAs/InAlAs	-	-	-	1500	5800	12.8

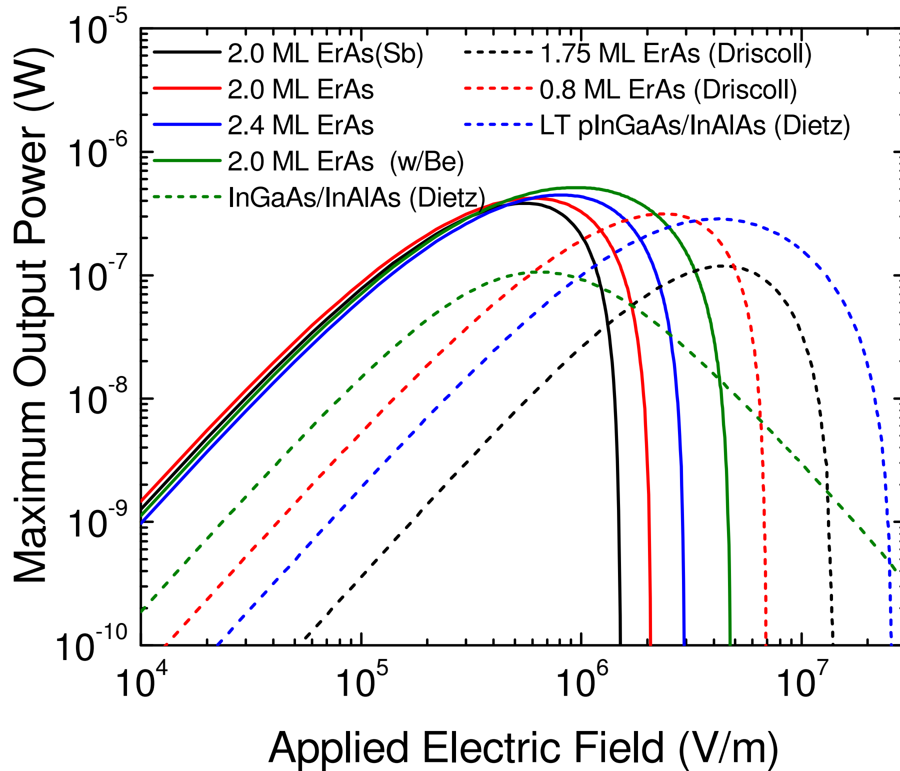

Figure 7.5: Calculated maximum output power as a function of electric field intensity at 1 THz for the best materials grown during this dissertation (solid lines) and compared to best materials grown by Driscoll [41] and Dietz [68,69] (dashed lines).

As can be seen from Figure 7.5, the beryllium counterdoped material developed in Chapter 5 showed the highest output power with nearly 60% higher output power than the highest calculated output power from a material found in the literature at 1 THz and nearly an order of magnitude higher output powers in the GHz range. Figure 7.6 shows the output power versus the mixing frequency.

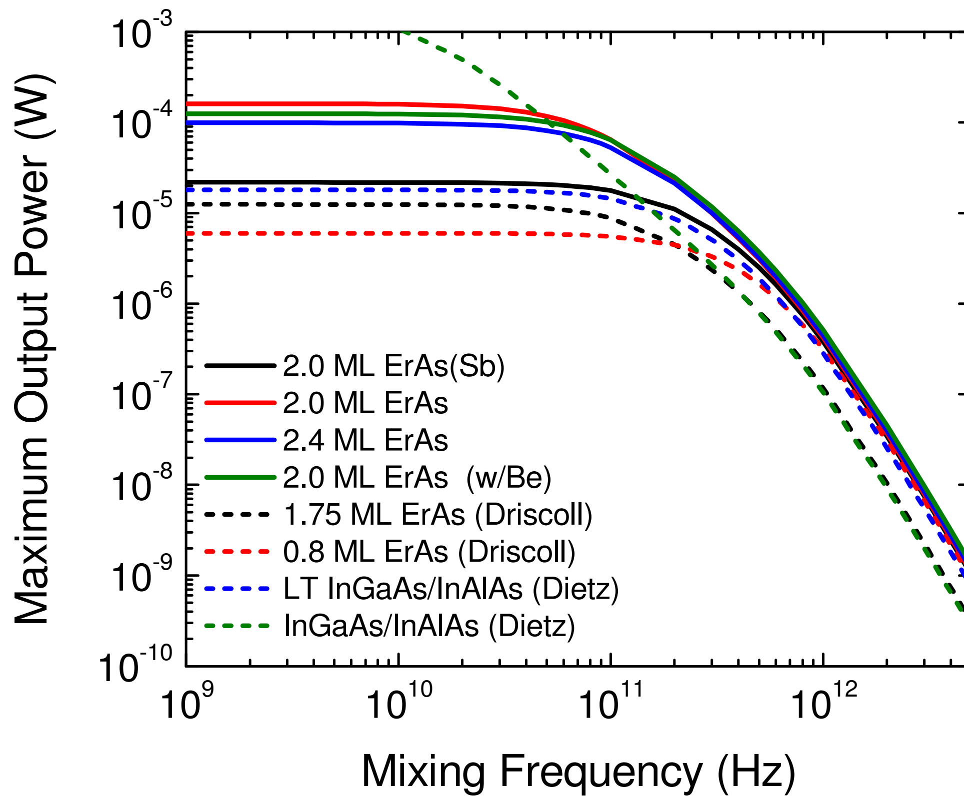

Figure 7.6: Calculated maximum output power versus mixing frequency for each material's optimal electric field bias for the best materials grown during this dissertation (solid lines) and compared to best materials grown by Driscoll [41] and Dietz [68,69] (dashed lines).

Chapter 8: Conclusions

Rare-earth pnictide nanostructures grown in III-V materials were investigated and assessed for use as small bandgap 1550 nm photoconductive materials for heterodyne THz generation. Several avenues were explored to improve upon the previous work from the USCB group who pioneered the small bandgap RE-As material system. Through the exchange of the RE atomic species, the importance of the structural quality of the matrix was discovered. Surfactant-mediated growth of the matrix and RE-As growth rate variation techniques were employed to dramatically improve the properties of the superlattice nanocomposites. A 50% increase in the previously considered maximum deposition amount of RE-As was demonstrated while maintaining high quality structural overgrowth of the matrix. The result was an increase in the dark resistivity by at least 25× and 2× decrease in the carrier lifetime, while maintaining mobilities over 3000 cm^2/V-s. Further optimizations of the enhanced superlattices were then explored by varying exchanging the RE atom to ErAs and changing the superlattice period thickness. This optimization resulted in a near order of magnitude increase the dark resistivity to 4.3 Ω-cm, a record for a 1550 nm bandgap material without the use of counterdoping. Mobilities remained near 3000 cm^2/V-s while carrier lifetimes dropped another 25%. The superlattice geometry and deposition (2.0 ML ErAs and 30 periods of 40 nm each) with the highest mobilites (4300 cm^2/V-s) were then used to explore counterdoping with increasing amounts of beryllium to attempt to shift the Fermi level alignment in the matrix towards the midgap, where the carrier recombination rate would be maximized. Dark resistivities increased to nearly 8 Ω-cm and carrier lifetimes dropped to 1.5 ps as the beryllium doping level increased to near the p-type turning point.

A compositional alloy of $In_{0.53}Ga_{0.47}As$ and $GaAs_{0.5}Sb_{0.5}$ was then explored as a method to tailor the position of the Fermi level without the need of counter doping, which did lower the mobility somewhat. The Fermi level aligns near the conduction band for InGaAs and near the valence band for GaAsSb, an alloy of $In_{0.19}Ga_{0.81}As_{0.68}Sb_{0.32}$ was successfully demonstrated and employed in superlattice nanocomposites which decreased the carrier lifetime to the sub-picosecond range (0.73 ps) while maintaining mobilities over 4000 cm^2/V-s, with a modest dark resistivity of 0.8 Ω-cm.

There are several avenues that should be pursued to further the understanding of the RE-V nanostructure III-V material system and some of these were attempted but were unsuccessful due to equipment limitations. The GdAs InGaAs system should be explored with the growth enhancement techniques developed to get a clearer sense of the potential impact of lattice matching to the host matrix. The ErAs having less strain than LuAs, demonstrated better properties and it would be interesting to see if GdAs follows that trend. The counterdoping with beryllium on the ErAs InGaAs system, enhanced by surfactant-mediated growth, should be fine tuned to see if the effective Fermi level can be pushed to the midgap where the resistivity is expect to increase and the lifetimes is expected to decrease. The ErAs(Sb) InGaAsSb system shows the biggest promise and different alloy composition as well as superlattice period thicknesses should be explored since the position of the Fermi stabilization energy is still not well understood.

Further exploration of RE-V nanostructures embedded in small bandgap III-V materials could lead to photoconductive nanocomposites that produce low-cost CW room-temperature and broadly tunable photomixer devices that would greatly benefit many security, spectroscopic, and medical applications.

Appendix A:

The following are sample sets for experiments that were not discussed in the previous chapters of this dissertation. Previous investigations on growth conditions [53] indicate a change in nanoparticle morphology with different growth temperatures. Table A.1 includes an experiment that changed the growth temperature of the InGaAs superlattices and assessed the changes in its properties. Table A.2 includes a sample set where an InAlAs layer was grown before the InGaAs buffer layer. It is important to notice that the mobility of the resulting superlattices were much higher than the superlattices without the InAlAs layers. This improvement is likely due to the smoothing effect of the InAlAs layer.

Table A.1: Properties of RE-As superlattices with 30 periods of 40 nm grown at various temperatures. The properties summarized include RE-As species and deposition amount, growth temperature (GT), growth rate (GR), root-mean-squared surface roughness (RMS SR), room temperature mobility (μ), room temperature dark resistivity (ρ), room temperature carrier concentration (n), Fermi level based on room temperature carrier concentration using Nilsson equation [107], activation energy from temperature dependent Hall (E_a), and carrier lifetime (τ).

RE-As (ML)	GT (°C)	GR (ML/s)	RMS SR (nm)	μ (cm^2/ V-s)	ρ (Ω cm)	n (cm^{-3})	E_F-CB (meV)	E_a (meV)	τ (ps)
LuAs	460	0.07	0.609	3605.62	0.0115	1.51E+17	-1.95	53.19	5.94
1.2	470	0.07	1.64	3499.57	0.0126	1.41E+17	-3.99	53.43	5.27
	480	0.07	0.755	2923.99	0.0131	1.63E+17	0.63	52.9	4.84
	490	0.07	0.696	2957.81	0.0243	8.67E+16	-19.14	71.76	3.59
	500	0.07	0.413	3054.74	0.0514	3.98E+16	-41.31	78.54	3.97
	510	0.07	0.468	2730	0.0596	3.82E+16	-42.46	-	-
GdAs	460	0.02	0.526	3766.8	0.0049	3.36E+17	27.05	-	2.59
1.0	470	0.02	0.566	3686.68	0.0049	3.45E+17	28.08	-	2.69
	480	0.02	0.816	3550.37	0.0069	2.55E+17	16.35	-	2.39
	490	0.02	0.773	3513.47	0.0075	2.37E+17	13.72	30.7	2.18
	500	0.02	0.506	3769.21	0.0088	1.88E+17	5.45	-	2.08
LaAs	460	0.02	-	3098.02	0.0998	2.02E+16	-59.55	59.14	34.27
0.2	470	0.02	2.28	2992.12	0.0456	4.58E+16	-37.45	45.07	24.71
	480	0.02	2.03	2956.71	0.0406	5.2E+16	-33.87	44.71	17.39
	490	0.02	3.93	2841.3	0.0367	5.98E+16	-29.95	43.74	10.09
LaAs	460	0.02	10.4	1405.6	0.1977	2.25E+16	-56.72	75.23	13.02
0.3	470	0.02	7.42	2351.32	0.0955	2.78E+16	-51.03	76.26	10.62
	480	0.02	7.93	2197.92	0.1125	2.53E+16	-53.60	76.72	10.62
	490	0.02	8.18	1918.42	0.088	3.7E+16	-43.30	65.34	9.22

Table A.2: Properties of bismuth enhanced ErAs superlattices grown at 490 °C with a 2500A InAlAs buffer layer before superlattice growth. The properties include: ErAs deposition (Dep), growth rate (GR), root-mean-squared surface roughness (RMS SR), room temperature mobility (μ), room temperature dark resistivity (ρ), room temperature carrier concentration (n), Fermi level based on room temperature carrier concentration using Nilsson equation [107], activation energy from temperature dependent Hall (E_a), and carrier lifetime (τ).

Dep. (ML)	GR (ML/s)	RMS SR (nm)	μ (cm^2/ V-s)	ρ (Ω cm)	n (cm^{-3})	E_F-CB (meV)	E_a (meV)	τ (ps)
0.8	0.01	0.266	4581.39	0.1227	1.11×10^{16}	-75.26	-	3.40
1.2	0.01	0.29	4968.47	0.3205	3.92×10^{15}	-102.35	-	2.60
1.6	0.01	0.317	6127.11	0.5337	1.91×10^{15}	-121.01	-	2.19
2.0	0.01	0.455	6541.21	0.9559	9.98×10^{14}	-137.83	-	1.88

References

[1] P. H. Siegel. Terahertz technology. *IEEE T. Microw. Theory.*, 50(3):910–928, March 2002.

[2] E. F. Nichols and J. D. Tear. Joining the infra-red and electric wave spectra. *Proceedings of the National Academy of Sciences*, 9(6):211–214, 1923.

[3] J. F. Federici, B. Schulkin, F. Huang, D. Gary, R. Barat, F. Oliveira, and D. Zimdars. Thz imaging and sensing for security applications—explosives, weapons and drugs. *Semicond. Sci. Technol.*, 20(7):S266, 2005.

[4] M. Tonouchi. Cutting-edge terahertz technology. *Nat. Phot.*, 1:97–105, 2007.

[5] V.P. Wallace, A.J. Fitzgerald, S. Shankar, N. Flanagan, R. Pye, J. Cluff, and D.D. Arnone. Terahertz pulsed imaging of basal cell carcinoma ex vivo and in vivo. *British Journal of Dermatology*, 151(2):424–432, 2004.

[6] C.B. Reid, A. Fitzgerald, G. Reese, R. Goldin, P. Tekkis, P.S. O'Kelly, E. Pickwell-MacPherson, A.P. Gibson, and V.P. Wallace. Terahertz pulsed imaging of freshly excised human colonic tissues. *Physics in Medicine and Biology*, 56(14):4333, 2011.

[7] D. Crawley, C. Longbottom, V.P. Wallace, B. Cole, D. Arnone, and M. Pepper. Three-dimensional terahertz pulse imaging of dental tissue. *Journal of Biomedical Optics*, 8(2):303–307, 2003.

[8] E. Pickwell, V.P. Wallace, B.E. Cole, S. Ali, C. Longbottom, R.J. Lynch, and Michael Pepper. Using terahertz pulsed imaging to measure enamel demineralisation in teeth. In *International Conference on Infrared Millimeter Waves and 14th International Conference on Teraherz Electronics*, pages 578–578, Sept 2006.

[9] S. Sy, S. Huang, Y.J. Wang, J. Yu, A.T. Ahuja, Y.T. Zhang, and E. Pickwell-MacPherson. Terahertz spectroscopy of liver cirrhosis: investigating the origin of contrast. *Physics in Medicine and Biology*, 55(24):7587, 2010.

[10] Z. D. Taylor, R. S. Singh, M. O. Culjat, J. Y. Suen, W. S. Grundfest, H. Lee, and E. R. Brown. Reflective terahertz imaging of porcine skin burns. *Opt. Lett.*, 33(11):1258–1260, Jun 2008.

[11] C. Wang and P. Sahay. Breath analysis using laser spectroscopic techniques: Breath biomarkers, spectral fingerprints, and detection limits. *Sensors*, 9(10):8230–8262, 2009.

[12] N. C. Luhmann and W. A. Peebles. Instrumentation for magnetically confined fusion plasma diagnostics. *Review of Scientific Instruments*, 55(3):279–331, 1984.

[13] D L Brower, K W Kim, L Zeng, Y Jiang, E J Doyle, and W A Peebles. Integrated reflectometer-interferometer system for plasma density profile measurement. *Plasma Physics and Controlled Fusion*, 40(9):1575, 1998.

[14] B. H. Deng, C. W. Domier, N. C. Luhmann, D. L. Brower, G. Cima, A. J. H. Donné, T. Oyevaar, and M. J. van de Pol. Ece imaging of electron temperature and electron temperature fluctuations (invited). *Review of Scientific Instruments*, 72(1):301–306, 2001.

[15] D.T. Leisawitz, W.C. Danchi, M.J. DiPirro, L.D. Feinberg, D.Y. Gezari, M. Hagopian, W.D. Langer, J.C. Mather, S.H. Moseley, M. Shao, R.F. Silverberg, J.G. Staguhn, M.R. Swain, H.W. Yorke, and X. Zhang. Scientific motivation and technology requirements for the spirit and specs far-infrared/submillimeter space interferometers. *Proc. SPIE*, 4013:36–46, 2000.

[16] C. Kulesa. Terahertz spectroscopy for astronomy: From comets to cosmology. *IEEE Transactions on Terahertz Science and Technology*, 1(1):232–240, Sept 2011.

[17] T.G. Phillips and J. Keene. Submillimeter astronomy [heterodyne spectroscopy]. *Proceedings of the IEEE*, 80(11):1662–1678, Nov 1992.

[18] H. Kanaya, H. Shibayama, R. Sogabe, S. Suzuki, and M. Asada. Fundamental oscillation up to 1.31 thz in resonant tunneling diodes with thin well and barriers. *Appl. Phys. Express*, 5(12):124101, 2012.

[19] E. Alekseev and D. Pavlidis. Gan gunn diodes for thz signal generation. In *IEEE MTT-S International Microwave Symposium Digest*, volume 3, pages 1905–1908 vol.3, June 2000.

[20] R. P. Joshi, V. Sridhara, P. Shah, and R. D. del Rosario. Monte carlo analysis of gan-based gunn oscillators for microwave power generation. *Journal of Applied Physics*, 93(8):4836–4842, 2003.

[21] A. Acharyya and J.P. Banerjee. Prospects of impatt devices based on wide bandgap semiconductors as potential terahertz sources. *Applied Nanoscience*, 4(1):1–14, 2014.

[22] E. R. Brown, C. D. Parker, L. J. Mahoney, K. M. Molvar, and J. R. Soderstrom. Oscillations up to 712 ghz in inas/alsb resonant-tunneling diodes. *Applied Physics Letters*, 58:2291–2293, May 1991.

[23] D. E. Brehmer, Kai Zhang, Ch. J. Schwarz, S.-P. Chau, S. J. Allen, J. P. Ibbetson, J. P. Zhang, C. J. Palmstro/m, and B. Wilkens. Resonant tunneling through eras semimetal quantum wells. *Applied Physics Letters*, 67(9):1268–1270, 1995.

[24] M. Tanaka, M. Tsuda, T. Nishinaga, and C. J. Palmstrom. Room-temperature negative differential resistance in alas/eras/alas heterostructures grown on (001)gaas. *Applied Physics Letters*, 68(1):84–86, 1996.

[25] A. Maestrini, I. Mehdi, J.V. Siles, J.S. Ward, R. Lin, B. Thomas, C. Lee, J. Gill, G. Chattopadhyay, E. Schlecht, J. Pearson, and P. Siegel. Design and

characterization of a room temperature all-solid-state electronic source tunable from 2.48 to 2.75 thz. *IEEE T. THz. Sci. Tech.*, 2(2):177–185, 2012.

[26] R. Kohler, A. Tredicucci, F. Beltram, H.E. Beere, E.H. Linfield, A.G. Davies, D.A. Ritchie, R.C. Iotti, and F. Rossi. Terahertz semiconductor-heterostructure laser. *Nat.*, 417:156–159, 2002.

[27] M.A. Belkin, F. Capasso, F. Xie, A. Belyanin, M. Fischer, A. Wittmann, and J. Faist. Room temperature terahertz quantum cascade laser source based on intracavity difference-frequency generation. *Appl. Phys. Lett.*, 92(20):201101, 2008.

[28] K. Vijayraghavan, R.W. Adams, A. Vizbaras, M. Jang, C. Grasse, G. Boehm, M.C. Amann, and M.A. Belkin. Terahertz sources based on cerenkov difference-frequency generation in quantum cascade lasers. *Appl. Phys. Lett.*, 100(25):251104, 2012.

[29] K. Vijayraghavan, Y. Jiang, M. Jang, A. Jiang, K. Choutagunta, A. Vizbaras, F. Demmerle, G. Boehm, M. C. Amman, and M.A. Belkin. Broadly tunable terahertz generation in mid-infrared quantum cascade lasers. *Nat. Commun.*, 4:2021, 2013.

[30] S. Jung, A. Jiang, Y. Jiang, K. Vijayraghavan, X. Wang, M. Troccoli, and M.A. Belkin. Broadly tunable monolithic room-temperature terahertz quantum cascade laser sources. *Nat. Commun.*, 5(4267), July 2014.

[31] R. H. Pantell, M. DiDomenico, O. Svelto, and J. N. Weaver. The theory of direct transistions in semiconductors. *Proc. Int. Conf. Quantum Elec.*, 1964.

[32] E. R. Brown, K. A. McIntosh, F. W. Smith, M. J. Manfra, and C. L. Dennis. Measurements of optical-heterodyne conversion in low-temperature-grown gaas. *Appl. Phys. Lett.*, 62(11):1206–1208, 1993.

[33] K. A. McIntosh, E. R. Brown, K. B. Nichols, O. B. McMahon, W. F. DiNatale, and T. M. Lyszczarz. Terahertz photomixing with diode lasers in low-temperature-grown gaas. *Appl. Phys. Lett.*, 67(26):3844–3846, 1995.

[34] I.S. Gregory, C. Baker, W.R. Tribe, I.V. Bradley, M.J. Evans, E.H. Linfield, A.G. Davies, and M. Missous. Optimization of photomixers and antennas for continuous-wave terahertz emission. *J. Quantum. Electron.*, 41(5):717 – 728, 2005.

[35] E. R. Brown, F. W. Smith, and K. A. McIntosh. Coherent millimeter-wave generation by heterodyne conversion in low-temperature-grown gaas photoconductors. *J. Appl. Phys.*, 73(3):1480–1484, 1993.

[36] D. Mittleman. *Sensing with Terahertz Radiation*. Springer, 2003.

[37] E. R. Brown. A photoconductive model for superior gaas thz photomixers. *Appl. Phys. Lett.*, 75(6):769–771, 1999.

[38] E. R. Brown. Thz generation by photomixing in ultrafast photoconductors. *International Journal of High Speed Electronics & Systems*, 13(2):497, 2003.

[39] S. Adachi. *Properties of Semiconductor Alloys*. John Wiley & Sons, Ltd., 2009.

[40] A.W. Jackson. *Low-temperature-grown gallium arsenide photomixers designed for increased terahertz output power*. PhD thesis, University of California Santa Barbara, 1999.

[41] D.C. Driscoll. *Metal-semiconductor nanocomposites for ultrafast photoconductors*. PhD thesis, University of California Santa Barbara, 2004.

[42] F.W. Smith, A.R. Calawa, C.-L. Chen, M.J. Manfra, and L.J. Mahoney. New mbe buffer used to eliminate backgating in gaas mesfets. *IEEE Electron Device Letters*, 9(2):77–80, Feb 1988.

[43] M R Melloch, J M Woodall, E S Harmon, N Otsuka, F H Pollak, D D Nolte, R M Feenstra, and M A Lutz. Low-temperature grown iii-v materials. *Annual Review of Materials Science*, 25(1):547–600, 1995.

[44] S. Gupta, J.F. Whitaker, and G.A. Mourou. Ultrafast carrier dynamics in iii-v semiconductors grown by molecular-beam epitaxy at very low substrate temperatures. *IEEE J. Quantum Electron.*, 28(10):2464 –2472, oct 1992.

[45] F.W. Smith. Device applications of low-temperature-grown gaas. *Mater. Res. Soc. Symp. Proc.*, 241:3–12, 1991.

[46] Y. Chen, S. Williamson, T. Brock, F. W. Smith, and A. R. Calawa. 375-ghz-bandwidth photoconductive detector. *Applied Physics Letters*, 59:1984–1986, oct 1991.

[47] T. Sands, C.J. Palmstrom, J.P. Harbison, V.G. Keramidas, N. Tabatabaie, T.L. Cheeks, R. Ramesh, and Y. Silberberg. Stable and epitaxial metal/iii-v semiconductor heterostructures. *Mater. Sci. Rep.*, 5(3):99 – 170, 1990.

[48] B. D. Schultz, S. G. Choi, and C. J. Palmstrom. Embedded growth mode of thermodynamically stable metallic nanoparticles on iii-v semiconductors. *Appl. Phys. Lett.*, 88(24):243117, 2006.

[49] B. D. Schultz and C. J. Palmstrom. Embedded assembly mechanism of stable metal nanocrystals on semiconductor surfaces. *Phys. Rev. B: Condens. Matter Mater. Phys.*, 73(24):241407, Jun 2006.

[50] J.M. Olney Zide. *Molecular beam epitaxial growth of III-V semimetal/III-V semiconductor nanocomposites for energy conversion applications*. PhD thesis, University of California Santa Barbara, 2007.

[51] D.R. Schmidt, J.P. Ibbetson, D.E. Brehmer, C.J. Palmstrom, and S.J. Allen. Giant magnetoresistance of self-assembled eras islands in gaas. In *Materials Research Society Symposium Proc.*, volume 475, pages 251–256, 1997.

[52] D. R. Schmidt, A. G. Petukhov, M. Foygel, J. P. Ibbetson, and S. J. Allen. Fluctuation controlled hopping of bound magnetic polarons in eras:gaas nanocomposites. *Phys. Rev. Lett.*, 82:823–826, Jan 1999.

[53] C. Kadow. *Self-assembled ErAs islands in GaAs for photomixer devices*. PhD thesis, University of California Santa Barbara, 2000.

[54] E.M. Krivoy. *Rare-earth monopnictide alloys for tunable, epitaxial metals*. PhD thesis, The University of Texas at Austin, 2013.

[55] C. Kadow, A. W. Jackson, A. C. Gossard, S. Matsuura, and G. A. Blake. Self-assembled eras islands in gaas for optical-heterodyne thz generation. *Appl. Phys. Lett.*, 76(24):3510–3512, 2000.

[56] C. Kadow, S. B. Fleischer, J. P. Ibbetson, J. E. Bowers, A. C. Gossard, J. W. Dong, and C. J. Palmstrom. Self-assembled eras islands in gaas: Growth and subpicosecond carrier dynamics. *Appl. Phys. Lett.*, 75(22):3548–3550, 1999.

[57] C. Kadow, A.W. Jackson, A.C. Gossard, J.E. Bowers, S. Matsuura, and G.A. Blake. Self-assembled eras islands in gaas for thz applications. *Physica E: Low-dimensional Systems and Nanostructures*, 7(1-2):97 – 100, 2000.

[58] J. E. Bjarnason, T. L. J. Chan, A. W. M. Lee, E. R. Brown, D. C. Driscoll, M. Hanson, A. C. Gossard, and R. E. Muller. Eras:gaas photomixer with two-decade tunability and 12 mu w peak output power. *Appl. Phys. Lett.*, 85(18):3983–3985, 2004.

[59] C. Kadow, J. A. Johnson, K. Kolstad, J. P. Ibbetson, and A. C. Gossard. Growth and microstructure of self-assembled eras islands in gaas. *J. Vac. Sci. Technol. B*, 18(4):2197–2203, 2000.

[60] C. Kadow, J. A. Johnson, K. Kolstad, and A. C. Gossard. Growth-temperature dependence of the microstructure of eras islands in gaas. *J. Vac. Sci. Technol. B*, 21(1):29–32, 2003.

[61] E R Brown, D C Driscoll, and A C Gossard. State-of-the-art in 1.55 µm ultrafast ingaas photoconductors, and the use of signal-processing techniques to extract the photocarrier lifetime. *Semicond. Sci. Technol.*, 20(7):S199, 2005.

[62] G H Dohler, F Renner, O Klar, M Eckardt, A Schwanhauber, S Malzer, D Driscoll, M Hanson, A C Gossard, G Loata, T Loffler, and H Roskos. Thz-photomixer based on quasi-ballistic transport. *Semicond. Sci. Technol.*, 20(7):S178, 2005.

[63] S. Preu, F. H. Renner, S. Malzer, G. H. Dohler, L. J. Wang, M. Hanson, A. C. Gossard, T. L. J. Wilkinson, and E. R. Brown. Efficient terahertz emission from ballistic transport enhanced n-i-p-n-i-p superlattice photomixers. *Appl. Phys. Lett.*, 90(21):212115, 2007.

[64] T. Ishibashi, N. Shimizu, S. Kodama, H. Ito, T. Nagatsuma, and T. Furuta. Uni-traveling-carrier photodiodes. In *Ultrafast Electronics and Optoelectronics*, page UC3. Optical Society of America, 1997.

[65] E. Rouvalis, C.C. Renaud, D.G. Moodie, M.J. Robertson, and A.J. Seeds. Traveling-wave uni-traveling carrier photodiodes for continuous wave thz generation. *Opt. Express*, 18(11):11105–11110, May 2010.

[66] C.W. Berry, M.R. Hashemi, S. Preu, H. Lu, A.C. Gossard, and M. Jarrahi. High power terahertz generation using 1550 nm plasmonic photomixers. *Appl. Phys. Lett.*, 105(1):011121, 2014.

[67] C. Baker, I. S. Gregory, W. R. Tribe, I. V. Bradley, M. J. Evans, E. H. Linfield, and M. Missous. Highly resistive annealed low temperature-grown ingaas with sub 500 fs carrier lifetimes. *Appl. Phys. Lett.*, 85(21):4965–4967, 2004.

[68] R.J B. Dietz, M. Gerhard, D. Stanze, M. Koch, B. Sartorius, and M. Schell. Thz generation at 1.55 um excitation: six-fold increase in thz conversion efficiency by separated photoconductive and trapping regions. *Opt. Express*, 19(27):25911–25917, 2011.

[69] R.J.B. Dietz, B. Globisch, M. Gerhard, A. Velauthapillai, D. Stanze, H. Roehle, M. Koch, T. Gobel, and M. Schell. 64uw pulsed terahertz emission from growth optimized ingaas/inalas heterostructures with separated photoconductive and trapping regions. *Appl. Phys. Lett.*, 103(6):061103, 2013.

[70] M.P. Hanson. *Erbium-V Semimetal and III-V Semiconductor Composite Materials*. PhD thesis, University of California Santa Barbara, 2007.

[71] D.C. Driscoll, M.P. Hanson, E. Mueller, and A.C. Gossard. Growth and microstructure of semimetallic eras particles embedded in an in0.53ga0.47as matrix. *J. Cryst. Growth*, 251(1–4):243 – 247, 2003.

[72] D. C. Driscoll, M. Hanson, C. Kadow, and A. C. Gossard. Electronic structure and conduction in a metal-semiconductor digital composite: Eras:ingaas. *Appl. Phys. Lett.*, 78(12):1703–1705, 2001.

[73] M. Sukhotin, E. R. Brown, A. C. Gossard, D. Driscoll, M. Hanson, P. Maker, and R. Muller. Photomixing and photoconductor measurements on eras/ingaas at 1.55 um. *Appl. Phys. Lett.*, 82(18):3116–3118, 2003.

[74] A. Y. Cho. Film deposition by molecular-beam techniques. *Journal of Vacuum Science & Technology*, 8(5):S31–S38, 1971.

[75] A.Y. Cho and J.R. Arthur. Molecular beam epitaxy. *Progress in Solid State Chemistry*, 10, Part 3(0):157 – 191, 1975.

[76] A. Y. Cho. Morphology of epitaxial growth of gaas by a molecular beam method: The observation of surface structures. *J. Appl. Phys.*, 41(7):2780–2786, 1970.

[77] A. Y. Cho. Gaas epitaxy by a molecular beam method: Observations of surface structure on the (001) face. *J. Appl. Phys.*, 42(5):2074–2081, 1971.

[78] A. Y. Cho. Bonding direction and surface structure orientation on gaas (001). *J. Appl. Phys.*, 47(7):2841–2843, 1976.

[79] J.H. Neave and B.A. Joyce. Structure and stoichiometry of 100 gaas surfaces during molecular beam epitaxy. *Journal of Crystal Growth*, 44(4):387 – 397, 1978.

[80] J.J. Harris, B A. Joyce, and P.J. Dobson. Oscillations in the surface structure of sn-doped gaas during growth by {MBE}. *Surface Science*, 103(1):L90 – L96, 1981.

[81] C.E.C. Wood. Red intensity oscillations during mbe of gaas. *Surface Science*, 108(2):L441 – L443, 1981.

[82] J. H. Neave, B. A. Joyce, P. J. Dobson, and N. Norton. Dynamics of film growth of gaas by mbe from rheed observations. *Applied Physics A: Materials Science & Processing*, 31:1–8, 1983. 1.

[83] B. F. Lewis, F. J. Grunthaner, A. Madhukar, T. C. Lee, and R. Fernandez. Reflection high energy electron diffraction intensity behavior during homoepitaxial molecular beam epitaxy growth of gaas and implications for growth kinetics and mechanisms. *J. Vac. Sci. Technol. B*, 3(5):1317–1322, 1985.

[84] H. Sakaki, M. Tanaka, and J. Yoshino. One atomic layer heterointerface fluctuations in gaas-alas quantum well structures and their suppression by insertion of smoothing period in molecular beam epitaxy. *Jpn. J. Appl. Phys.*, 24(Part 2, No. 6):L417–L420, 1985.

[85] M A Moram and M E Vickers. X-ray diffraction of iii-nitrides. *Rep. Prog. Phys.*, 72(3):036502, 2009.

[86] H.B. Yuen. *Growth and characterization of dilute nitride antimonides for long-wavelength optoelectronics*. PhD thesis, Stanford University, 2006.

[87] E. H. Hall. On a new action of the magnet on electric currents. *American Journal of Mathematics*, 2(3):287–292, Sep. 1879.

[88] L. J. van der Pauw. A method of measuring specific resistivity an hall effect of discs of arbitrary shapes. *Philips Research Reports*, 13:1–9, 1958.

[89] L. J. van der Pauw. A method of measuring the resistivity and hall coefficient on lamellae of arbitrary shape. *Philips Technical Review*, 20:220–224, 1958.

[90] R. Chwang, B.J. Smith, and C.R. Crowell. Contact size effects on the van der pauw method for resistivity and hall coefficient measurement. *Solid-State Electron.*, 17(12):1217 – 1227, 1974.

[91] S.M. Sze and Kwok K. Ng. *Physics of Semiconductor Devices*. John Wiley and Sons, New Jersey, 2007.

[92] E. F. Schubert. *Doping in III-V semiconductors*. Cambridge University Press, 1993.

[93] D. G. Deppe, N. D. Gerrard, C. J. Pinzone, R. D. Dupuis, and E. F. Schubert. Quarter-wave bragg reflector stack of inp-in0.53ga0.47as for 1.65 um wavelength. *Applied Physics Letters*, 56(4):315–317, 1990.

[94] R. S. Muller and T. I. Kamins. *Device Electronics for Integrated Circuits*. John Wiley and Sons, 1986.

[95] R. N. Hall. Electron-hole recombination in germanium. *Phys. Rev.*, 87:387–387, Jul 1952.

[96] W. Shockley and W. T. Read. Statistics of the recombinations of holes and electrons. *Phys. Rev.*, 87:835–842, Sep 1952.

[97] J. M. Zide, D. O. Klenov, S. Stemmer, A. C. Gossard, G. Zeng, J. E. Bowers, D. Vashaee, and A. Shakouri. Thermoelectric power factor in semiconductors with buried epitaxial semimetallic nanoparticles. *Applied Physics Letters*, 87(11):112102, 2005.

[98] J K Lang, Y Baer, and P A Cox. Study of the 4f and valence band density of states in rare-earth metals. ii. experiment and results. *Journal of Physics F: Metal Physics*, 11(1):121, 1981.

[99] L.V. Pourovskii, K.T. Delaney, C.G. Van de Walle, N.A. Spaldin, and A. Georges. Role of atomic multiplets in the electronic structure of rare-earth semiconductors and semimetals. *Phys. Rev. Lett.*, 102:096401, Mar 2009.

[100] K.T. Delaney, N.A. Spaldin, and C.G. Van de Walle. Theoretical study of schottky-barrier formation at epitaxial rare-earth-metal/semiconductor interfaces. *Phys. Rev. B: Condens. Matter Mater. Phys.*, 81(16):165312, 2010.

[101] L.E. Clinger, G. Pernot, T.E. Buehl, P.G. Burke, A.C. Gossard, C.J. Palmstrom, A. Shakouri, and J.M.O. Zide. Thermoelectric properties of epitaxial tbas:ingaas nanocomposites. *J. Appl. Phys.*, 111(9):094312, 2012.

[102] D. C. Driscoll, M. P. Hanson, A. C. Gossard, and E. R. Brown. Ultrafast photoresponse at 1.55 um in ingaas with embedded semimetallic eras nanoparticles. *Appl. Phys. Lett.*, 86(5):051908, 2005.

[103] E. M. Krivoy, H. P. Nair, A. M. Crook, S. Rahimi, S. J. Maddox, R. Salas, D. A. Ferrer, V. D. Dasika, D. Akinwande, and S. R. Bank. Growth and characterization of luas films and nanostructures. *Appl. Phys. Lett.*, 101(14):141910, 2012.

[104] R. Hanks and M. M. Faktor. Quantitative application of dynamic differential calorimetry. part 2. heats of formation of the group 3a arsenides. *Trans. Faraday Soc.*, 63:1130–1135, 1967.

[105] E. M. Krivoy, S. Rahimi, H. P. Nair, R. Salas, S. J. Maddox, D. J. Ironside, Y. Jiang, G. Kelp, G. Shvets, D. Akinwande, and S. R. Bank. Growth and characterization of single crystal rocksalt laas using luas barrier layers. *Appl. Phys. Lett.*, 101(22):221908, 11 2012.

[106] L.R. Vanderhoef, A.K. Azad, C.C. Bomberger, D.R. Chowdhury, D.B. Chase, A.J. Taylor, J.M. O. Zide, and M.F. Doty. Charge carrier relaxation processes in tbas nanoinclusions in gaas measured by optical-pump thz-probe transient absorption spectroscopy. *Phys. Rev. B: Condens. Matter Mater. Phys.*, 89:045418, Jan 2014.

[107] N. G. Nilsson. An accurate approximation of the generalized einstein relation for degenerate semiconductors. *physica status solidi A: Applications and Materials Science*, 19(K75), 1973.

[108] E. Tournie and K.H. Ploog. Surfactant-mediated molecular beam epitaxy of strained layer semiconductor heterostructures. *Thin Solid Films*, 231(1–2):43 – 60, 1993.

[109] M. Copel, M. C. Reuter, Efthimios Kaxiras, and R. M. Tromp. Surfactants in epitaxial growth. *Phys. Rev. Lett.*, 63:632–635, Aug 1989.

[110] M. Copel, M. C. Reuter, M. Horn von Hoegen, and R. M. Tromp. Influence of surfactants in ge and si epitaxy on si(001). *Phys. Rev. B: Condens. Matter Mater. Phys.*, 42:11682–11689, Dec 1990.

[111] R.I.G. Uhrberg, R. D. Bringans, R. Z. Bachrach, and John E. Northrup. Symmetric arsenic dimers on the si(100) surface. *Phys. Rev. Lett.*, 56:520–523, Feb 1986.

[112] S.S. Iyer, J. C. Tsang, M. W. Copel, P. R. Pukite, and R. M. Tromp. Growth temperature dependence of interfacial abruptness in si/ge heteroepitaxy studied by raman spectroscopy and medium energy ion scattering. *Applied Physics Letters*, 54(3):219–221, 1989.

[113] E. Kasper and H. Jorke. *Growth Kinetics of Silicon Molecular Beam Epitaxy*, volume 10 of *Springer Series in Surface Sciences*. Springer Berlin Heidelberg, 1988.

[114] J. Massies and N. Grandjean. Surfactant effect on the surface diffusion length in epitaxial growth. *Phys. Rev. B: Condens. Matter Mater. Phys.*, 48:8502–8505, Sep 1993.

[115] E. Tournie, N. Grandjean, A. Trampert, J. Massies, and K.H. Ploog. Surfactant-mediated molecular-beam epitaxy of iii-v strained-layer heterostructures. *J. Cryst. Growth*, 150, Part 1(0):460 – 466, 1995.

[116] R.L. Schwoebel and E.J. Shipsey. Step motion on crystal surfaces. *Journal of Applied Physics*, 37(10):3682–3686, 1966.

[117] G. Ehrlich and F. G. Hudda. Atomic view of surface self-diffusion: Tungsten on tungsten. *The Journal of Chemical Physics*, 44(3):1039–1049, 1966.

[118] E. Tournie and K.H. Ploog. Virtual-surfactant epitaxy of strained inas/al0.48in0.52as quantum wells. *Applied Physics Letters*, 62(8):858–860, 1993.

[119] A. Sakai, T. Tatsumi, and K. Ishida. Prevention of crystallization by surfactants during si molecular-beam deposition on amorphous-si films. *Phys. Rev. B*, 47:6803–806, Mar 1993.

[120] W. Dondl, G. Lütjering, W. Wegscheider, J. Wilhelm, R. Schorer, and G. Abstreiter. Sn and sb segregation and their possible use as surfactant for short-period si/ge superlattices. *Journal of Crystal Growth*, 127(1–4):440 – 442, 1993.

[121] H. J. Osten, J. Klatt, G. Lippert, E. Bugiel, and S. Higuchi. Surfactant mediated growth of germanium on silicon (001) with submonolayer coverage of sb and te. *Journal of Applied Physics*, 74(4):2507–2511, 1993.

[122] D. Rioux and H. Hochst. Sb/inp(100) interface: A precursor to surfactant-mediated ge epitaxy. *Phys. Rev. B*, 46:6857–6863, Sep 1992.

[123] H. Shimizu, K. Kumada, S. Uchiyama, and A. Kasukawa. 1.2 um range gainas sqw lasers using sb as surfactant. *Electronics Letters*, 36(16):1379–1381, Aug 2000.

[124] X. Yang, M. J. Jurkovic, J. B. Heroux, and W. I. Wang. Molecular beam epitaxial growth of ingaasn:sb/gaas quantum wells for long-wavelength semiconductor lasers. *Applied Physics Letters*, 75(2):178–180, 1999.

[125] W. Ha, V. Gambin, M. Wistey, S. Bank, H. Yuen, S. Kim, and Jr. Harris, J.S. Long wavelength gainnassb/ganassb multiple quantum well lasers. *Electronics Letters*, 38(6):277–278, Mar 2002.

[126] V. Gambin, Wonill Ha, M. Wistey, Homan Yuen, S.R. Bank, Seongsin M. Kim, and James S. Harris. Gainnassb for 1.3-1.6- um-long wavelength lasers grown by molecular beam epitaxy. *IEEE J. Sel. Topics in Quantum Electron.*, 8(4):795–800, Jul 2002.

[127] K. Volz, V. Gambin, W. Ha, M.A. Wistey, H. Yuen, S. Bank, and J.S. Harris. The role of sb in the mbe growth of (gain)(nassb). *Journal of Crystal Growth*, 251(1–4):360 – 366, 2003. Proceedings of the Twelfth International Conference on Molecular Beam Epitaxy.

[128] S.R. Bank, M.A. Wistey, L.L. Goddard, H.B. Yuen, V. Lordi, and Jr. Harris, J.S. Low-threshold continuous-wave 1.5 um gainnassb lasers grown on gaas. *IEEE J. Quantum Electron.*, 40(6):656 – 664, june 2004.

[129] S.R. Bank, Hopil Bae, L.L. Goddard, H.B. Yuen, M.A. Wistey, R. Kudrawiec, and J.S. Harris. Recent progress on 1.55 um dilute nitride lasers. *IEEE J. Quantum Electron.*, 43(9):773 –785, 2007.

[130] J.S. Harris, R. Kudrawiec, H. B. Yuen, S. R. Bank, H. P. Bae, M. A. Wistey, D. Jackrel, E. R. Pickett, T. Sarmiento, L. L. Goddard, V. Lordi, and T. Gugov. Development of gainnassb alloys: Growth, band structure, optical properties and applications. *Phys. Status Solidi B*, 244(8):2707–2729, 2007.

[131] S. Tixier, M. Adamcyk, E.C. Young, J.H. Schmid, and T. Tiedje. Surfactant enhanced growth of ganas and inganas using bismuth. *J. Cryst. Growth*, 251(1–4):449 – 454, 2003.

[132] X. Lu, D.A. Beaton, R.B. Lewis, T. Tiedje, and M.B. Whitwick. Effect of molecular beam epitaxy growth conditions on the bi content of gaas(1-x)bi(x). *Appl. Phys. Lett.*, 92:192110, 2008.

[133] K. Sakamoto, K. Kyoya, K. Miki, H. Matsuhata, and T. Sakamoto. Which surfactant shall we choose for the heteroepitaxy of ge/si(001)? –bi as a surfactant with small self-incorporation–. *Jpn. J. Appl. Phys.*, 32(2A):L204, 1993.

[134] K. Sakamoto, H. Matsuhata, K. Kyoya, K. Miki, and T. Sakamoto. Abrupt si/ge/si(001) interfaces fabricated with bi as a surfactant. *Jpn. J. Appl. Phys.*, 33(Part 1, No. 4B):2307–2310, 1994.

[135] M. R. Pillai, Seong-Soo Kim, S. T. Ho, and S. A. Barnett. Growth of in(x)ga(1-x)as/gaas heterostructures using bi as a surfactant. *J. Vac. Sci. Technol. B*, 18(3):1232–1236, 2000.

[136] E.C. Young, S. Tixier, and T. Tiedje. Bismuth surfactant growth of the dilute nitride gan(x)as(1-x). *J. Cryst. Growth*, 279(3–4):316 – 320, 2005.

[137] G. Feng, K. Oe, and M. Yoshimoto. Temperature dependence of bi behavior in mbe growth of ingaas/inp. *J. Cryst. Growth*, 301–302:121 – 124, 2007.

[138] M. P. Hanson, D. C. Driscoll, J. D. Zimmerman, A. C. Gossard, and E. R. Brown. Subpicosecond photocarrier lifetimes in gasb/ersb nanoparticle superlattices at 1.55um. *Appl. Phys. Lett.*, 85(15):3110–3112, 2004.

[139] R. Salas, S. Guchhait, S. D. Sifferman, K. M. McNicholas, V. D. Dasika, E. M. Krivoy, D. Jung, M. L. Lee, and S. R. Bank. Growth and properties of rare-earth arsenide ingaas nanocomposites for terahertz generation. *Appl. Phys. Lett.*, 106(8):081103, 2015.

[140] C. Colinet. The thermodynamic properties of rare earth metallic systems. *J. Alloys Compd.*, 225(1-2):409 – 422, 1995. Proceedings of the 2nd International Conference on f-Elements.

[141] A P Bayanov. Thermodynamics of the interaction of the lanthanides with other elements. *Russ. Chem. Rev.*, 44(2):122, 1975.

[142] C. J. Palmstrom, T. L. Cheeks, H. L. Gilchrist, J. G. Zhu, C. B. Carter, B. J. Wilkens, and R. Martin. Effect of orientation on the schottky barrier height of thermodynamically stable epitaxial metal/gaas structures; eras; schottky; gaas. *J. Vac. Sci. Technol. A*, 10(4):1946 –1953, jul 1992.

[143] K.T. Delaney, N.A. Spaldin, and C.G. Van de Walle. Theoretical study of the structural and electronic properties of strained eras. *Phys. Rev. B: Condens. Matter Mater. Phys.*, 77:235117, Jun 2008.

[144] W. Walukiewicz. Mechanism of schottky barrier formation: The role of amphoteric native defects. *J. Vac. Sci. Technol. B*, 5(4):1062–1067, 1987.

[145] W. Walukiewicz. Fermi level dependent native defect formation: Consequences for metal–semiconductor and semiconductor–semiconductor interfaces. *J. Vac. Sci. Technol. B*, 6(4):1257–1262, 1988.

[146] W. Walukiewicz. Mechanism of fermi-level stabilization in semiconductors. *Phys. Rev. B*, 37:4760–4763, Mar 1988.

[147] W. Walukiewicz. Intrinsic limitations to the doping of wide-gap semiconductors. *Physica B*, 302–303(0):123 – 134, 2001.

[148] E. Tokumitsu. Correlation between fermi level stabilization positions and maximum free carrier concentrations in iii–v compound semiconductors. *Jpn. J. Appl. Phys.*, 29(Part 2, No. 5):L698–L701, 1990.

[149] E. F. Schubert, G. H. Gilmer, R. F. Kopf, and H. S. Luftman. Maximum concentration of impurities in semiconductors. *Phys. Rev. B*, 46:15078–15084, Dec 1992.

[150] D. Mathiot and J. C. Pfister. Dopant redistribution in heavily doped silicon: Confirmation of the validity of the vacancy-percolation model. *Journal of Applied Physics*, 66(2):970–972, 1989.

[151] G. A. Baraff and M. Schlüter. Electronic structure, total energies, and abundances of the elementary point defects in gaas. *Phys. Rev. Lett.*, 55:1327–1330, Sep 1985.

[152] T. N. Theis, P. M. Mooney, and S. L. Wright. Electron localization by a metastable donor level in *n-GaAs*: A new mechanism limiting the free-carrier density. *Phys. Rev. Lett.*, 60:361–364, Jan 1988.

[153] E. F. Schubert, J. M. Kuo, R. F. Kopf, H. S. Luftman, L. C. Hopkins, and N. J. Sauer. Beryllium delta doping of gaas grown by molecular beam epitaxy. *Journal of Applied Physics*, 67(4):1969–1979, 1990.

[154] R.T. Tung. Recent advances in schottky barrier concepts. *Materials Science and Engineering: R: Reports*, 35(1–3):1 – 138, 2001.

[155] C.G. Van de Walle and J. Neugebauer. Universal alignment of hydrogen levels in semiconductors, insulators and solutions. *Nat.*, 423:626–628, 2003.

[156] J.D. Zimmerman, E.R. Brown, and A.C. Gossard. Tunable all epitaxial semimetal-semiconductor schottky diode system: Eras on inalgaas. *Journal of Vacuum Science Technology B: Microelectronics and Nanometer Structures*, 23(5):1929–1935, 2005.

[157] I. Vurgaftman, J. R. Meyer, and L. R. Ram-Mohan. Band parameters for iii–v compound semiconductors and their alloys. *J. Appl. Phys.*, 89(11):5815–5875, 2001.

[158] V.S. Sorokin, S.V. Sorokin, A.N. Semenov, B.Ya. Meltser, and S.V. Ivanov. Novel approach to the calculation of instability regions in gainassb alloys. *J. Cryst. Growth*, 216(1–4):97 – 103, 2000.